The detection of delaminations in vibrating composite beams

Harrison, Christopher

Award date:
2000

Awarding institution:
University of Bath

THE DETECTION OF DELAMINATIONS IN VIBRATING COMPOSITE BEAMS

Submitted by Christopher Harrison
for the degree of PHD
of the University of Bath
2000

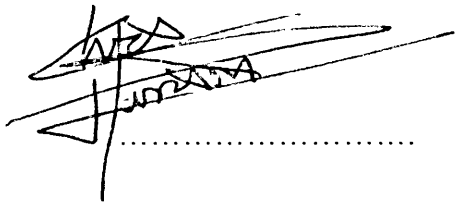

ProQuest LLC
789 East Eisenhower Parkway
P.O. Box 1346
Ann Arbor, MI 48106-1346

"Of particular significance are the paterae - small saucepan-like vessels of pewter, silver and bronze - used for pouring libations. Some bear inscriptions to the patron deity - *Deae Sul Min* or simply D.S.M - to the goddess Sulis Minerva. The pewter paterae are plain, perhaps manufactured as votives to be inscribed and thrown into the Spring unused."

Information from the Roman Baths, Bath, on Roman offerings to the gods.

Contents

Acknowledgements

I've always thought that the acknowledgements in a thesis were thin, shallow things; that are only written to adhere to the status quo. And yet, when it becomes my turn to write one, I find that I really do want to thank the people that have helped me in researching for, and writing, this thesis. I really could not have achieved this without them, and they all receive my heartfelt thanks.

Firstly, my supervisor, Dr. Richard Butler, who offered advice, encouragement and (almost unending) patience throughout the three-and-a-bit years. Also, Jim Askew, and later, Richard Weston; two men who gave me much advice about all things practical.

I should also thank Dr. Ranjan Banerjee from City University, who not only developed the software upon which this research heavily rests, but also offered much encouragement and advice in its use.

I would also like to thank Professor Almond and Frank Hammet from the School of Materials Science at the University, who offered advice and assistance the manufacturing of composite beams. Dr. James Ball from British Aerospace Airbus Ltd. also helped in this area, not only by supplying materials for testing, but also for providing advice in the area of NDT, where he has considerable knowledge. Also Richard Cox, who, as part of his final year research project, manufactured and tested some of the carbon-fibre beams; I hope I was as much help to him as he was to me.

Also, not forgetting all the people who shared the office with me; Chris, Tony, Yiannis, Mark, James, Beccy and Sabina (in estimated height order for a change). Of course they helped in my research if I asked, but their contribution mostly came the best way of all, keeping me happy! And finally, two guys who felt like I've shared the office with; Mike, from whom I inherited my desk, and Tony Miles, who had so many coffee breaks in the office, it felt like he was a permanent resident!

Abstract

This thesis presents a method of locating delaminations within composite beams. The method presented herein compares the natural frequencies and mode-shapes of a delaminated beam, with those predicted by an analytical model. The differences are quantified by an objective function, which is minimised using a numerical optimisation technique. When the difference between the analytically produced modal parameters, and those measured experimentally, is minimised, the damage is said to have been located.

The analytical model used within this thesis to obtain the natural frequencies and mode-shapes is the Dynamic Stiffness Method (DSM), based on Timoshenko beam theory. A simple model, based on the static deflection of a cantilever beam, is developed to obtain an estimate for the effective shear and torsional rigidities of the delaminated area, and these are incorporated into the DSM.

The damage is located using a two stage optimisation process. Firstly the differences in the analytical and experimental frequencies and mode-shapes are minimised by altering the material properties and support conditions of the model. This is achieved using the Modified Method of Feasible Directions (MMFD), a gradient-based optimisation procedure.

Once the material properties have been obtained, damage is located by altering the size and number of delaminations within the beams. Results are obtained and compared from using two different optimisation procedures; the MMFD and a genetic algorithm.

The method is firstly assessed by applying example input data, obtained analytically, and the sensitivity to experimental error is assessed by applying random errors to this data. Finally, results from experimental beams with delaminations, obtained by inserting thin strips of Teflon during manufacture, are obtained, and applied to the method.

List of Figures

List of Tables

Nomenclature

$a(\omega)$	Acceleration in the frequency domain
$[A']$	3-D laminate stiffness matrix
$(AG)'$	Equivalent shear rigidity of a delaminated section
A	Cross sectional area
$[B']$	3-D Laminate stiffness matrix
b	Beam width
$[D]$	2-D Laminate stiffness matrix
$[D']$	3-D Laminate stiffness matrix
d	Beam thickness
E	Young's modulus
EA	Axial stiffness
EI	Bending rigidity
$f(\omega)$	Force in the frequency domain
$[F]$	Vector of forces and moments
$F(i)$	Fitness of binary structure
$(GJ)'$	Equivalent torsional rigidity of a delaminated section
G	Shear modulus
$G(X)$	Inequality constraint
GJ	Torsional rigidity
h	Bending displacement
$H(y)$	Amplitude of sinusoidally-varying bending displacement at location y
$H(\omega)$	Accelerance
I	Second moment of area
I_α	Polar mass moment of inertia per unit length
$[K]$	Dynamic stiffness matrix
k	Shear correction factor
kAG	Shear rigidity
K_{BA}	Bending-extension coupling constant
K_{BT}	Bending-torsional coupling rigidity
k_h	Root vertical spring stiffness
k_θ	Root torsional spring stiffness
k_ψ	Root bending rotation spring stiffness

l	Beam length
l_a	Location of delamination along Y-axis
l_b	Location of delamination along Z-axis
l_{clamp}	Length of beam clamped to support
l_d	Length of delamination
l_{ui}	Length of undelaminated beam section i
$[M]$	Vector of bending and torsional moments per unit width acting on laminate
m	Mass per unit length
M	Bending moment
Mx	Chordwise bending moment per unit width acting on a plate cross section
M_{xy}	Torsional moment per unit width acting on a plate cross section
M_y	Lengthwise bending moment per unit width acting on a plate cross section
$[N]$	Vector of direct and shear load per unit width acting on laminate
n	Mode order
$n_{combinations}$	Number of combinations of delamination arrangement
n_{con}	Number of constraints
n_{delams}	Number of delaminations
n_{dv}	Number of design variables
n_f	Number of natural frequencies
n_p	Number of points used to define mode-shapes
n_{plies}	Number of plies
n_{pop}	Population size
$O(X)$	Objective function
$O'(X,r)$	Transformed objective function
P	Axial force in the Y-direction
$P(G(X))$	Penalty function
P^t	Force in the X-direction to
p_c	Probability of crossover
p_m	Probability of mutation
$p_{selection}$	Probability of selection
q	Iteration number
Q	Quality factor
Q^k	Transformed off-axis lamina modulus of the kth ply with angle θ_{ply}
r	Penalty function scalar multiplier

S	Shear force
S^q	Search direction of iteration q
t	Time
T	Torque
t_{ply}	Thickness of one ply
u	Sub-laminate extension
$[U]$	Displacement vector
U_s	Strain energy due to shear
v	Tip deflection of a cantilever beam
W	Cantilever tip load
$[X]$	Vector of design variables
X^L	Lower bound of side constraint
X^U	Upper bound of side constraint
y	Distance along Y axis
z	Distance along Z axis
$\bar{z}$	Distance of neutral axis to z=0
α	Weighting constant
α^*	Scalar move parameter
α^*_{est}	Estimate of the scalar move parameter
β	Weighting constant
δ	End deflection
δ_m	End deflection due to bending moment
δ_s	End deflection due to shear
δX	Small change in design variable
Δ	Difference in extension of two adjacent laminates
Δ^t	Difference in transverse displacement due to twist
$[\varepsilon]$	Vector of laminate in-plane and shear strains
$[\kappa]$	Vector of laminate mid-plane curvatures of the mid-plane
ϕ	Mode shape
ϕ^*	Experimental mode shape
γ_{yz}	Shear strain
η	Angle of cantilever tip deflection
ν	Poisson's ratio

θ	Angle of bending rotation
θ_{ply}	Ply angle
$\Theta(y)$	Amplitude of sinusoidally-varying bending rotation at location y
ρ	Density
τ	Shear stress
ω	Natural frequency
ω'	Normalised natural frequency
ω^*	Experimental natural frequency
ω_0	Undamped natural frequency
ψ	Angle of torsional rotation
$\Psi(y)$	Amplitude of sinusoidally-varying torsional rotation at location y
∇	Finite difference gradient operator

1. Introduction

1.1 Composite Materials: An Overview

The use of composite materials in the aviation industry began as early as December 17th, 1903, when the Wright brothers' first aircraft, the Flyer 1, took to the sky (Kelly (1994)), but it took a little while longer for structural plastics to become common. In fact it was the 1940s when military aircraft began using glass-fibre-reinforced plastics, mostly as secondary structural components because of the low specific stiffness and compressive strength that such materials had at the time (Delmonte (1981)). In 1941, a report by the Army Air Corps specified the minimum values for the mechanical properties of plastics if they were to be used for primary structures, being (at 160°, 75° and -65°F [71°, 22° and -54°C]):

Tensile strength: 22000 psi [151.7×10^6 Pa]
Flexural strength: 13000 psi [89.6×10^6 Pa]
Modulus of elasticity: 3.6×10^6 psi [24.8×10^9 Pa]

It was not until the late 1960s, with the earlier discovery of carbon fibres at the Royal Aircraft Establishment at Farnborough, UK, in 1964, that composites became widespread. Used on a demonstrator basis, trim tabs, spoilers, rudders and doors were produced from carbon-fibre-reinforced plastics.

As the use of composite materials increased, the fibre and matrix properties were improved, meaning that traditional metallic structures could increasingly be replaced with composites. Figure 1.1.1 compares the specific stiffness and strengths of uni-directional composite laminates with typical structural isotropic materials, showing the significant advantages that composite materials can offer to the structural engineer. This has to some extent been taken advantage of in the aviation industry. Figure 1.1.2 shows the increase in use of carbon composites in civil aircraft.

Delmonte defines composite materials with three main points. A composite material:

- "Consists of two or more physically distinct and mechanically separable materials."

- "Can be made by mixing the separate materials in such a way that the dispersion of one material in the other can be done in a controlled way to achieve optimum properties."
- "[Has] properties [that] are superior, and possibly unique in some specific respects, to the properties of the individual components."

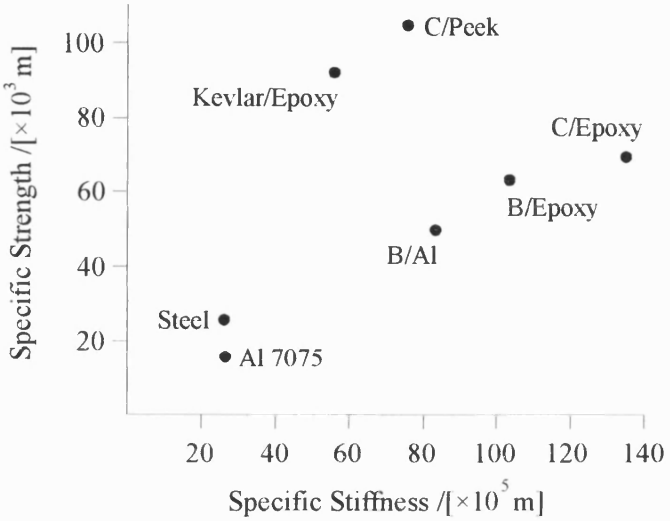

Figure 1.1.1 – Specific stiffness and strength of some isotropic materials and uni-directional laminates (Kelly (1995))

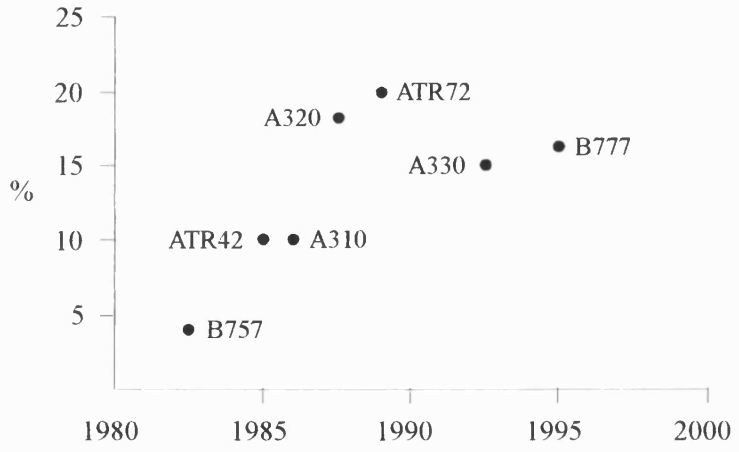

Figure 1.1.2 - Percentage of structure made of carbon composite material - Civil Aircraft (Davies (1995))

There are numerous classes of fibre/matrix composite materials that fall under this definition, for example:

- Randomly distributed chopped fibres in a resin matrix, used mainly as moulding components.
- Continuous fibres in a resin matrix, sometimes as a unidirectional tape, which may be positioned as desired.
- Woven fabrics that are laminated together with a resin.
- Honeycomb constructions.
- Continuous long poltrusions.

This encompasses a wide range of materials, displaying quite different micro- and macroscopic properties. This research concentrates mostly on the second type of structure, with a small section giving experimental results for laminates of woven fibres.

1.2 Damage of Composite Materials

With the advent of new materials and the new opportunities therein, there also came new problems. One such problem was that the new material structures had complex damage mechanisms, which were not fully understood. Because of the relative complexity of fibre/matrix systems when compared to metals, the damage mechanisms in composite materials are complex, dependent upon the loading condition, material properties and the geometry of the structure. Damage in composite materials can take the form of a combination of many different types; fibre fracture, matrix cracking, fibre-matrix interface de-bonding, and delamination are a few examples.

There has been extensive research investigating the damage mechanisms involved in composite materials, and a brief review of some of the relevant literature is given here.

Zhou and Davies (1995a) investigated woven glass fibre laminates under tension, compression and shear loads, and later (Zhou and Davies (1995b)) under flexure loads. They showed that the failure mechanisms are complex, and are as dependent upon the manufacturing tolerances as the loading conditions. When loading the specimens in tension, the failure mechanisms and associated failure stresses were found to be dependent upon the manufacturing tolerances (such as the

straightening of initial fibre 'kinks'). When loaded in shear, the damage mechanism was dependent upon the test conditions, and was greatly affected by the size of the specimen.

O'Brien and Reifsnider (1977) investigated damage caused by fatigue. Investigating Boron/epoxy laminates, they found that repeated cycles of tension/compression caused breakage of individual fibres, de-bonding and cracking of the matrix. Only the matrix damage caused significant reduction in axial rigidity of the laminates, although it did not appear to reduce the strength of the laminate.

Damage can also be induced during the manufacturing process. Garrett (1986) investigated the effect of porosity, caused by using an incorrect curing cycle, on the strength of mechanically fastened joints. Delaminations at the exit of drilled holes and joints with incorrect fastener seating depths and angles were also investigated. Significant strength reductions were recorded for the first two types of defect, although this was less evident for incorrect fastening.

1.3 Barely Visible Impact Damage and Delaminations

The most intensively investigated damage process, and the one most critical for the aviation industry, is however due to low velocity impact, which causes Barely Visible Impact Damage (BVID). As the name suggests, BVID is difficult to detect, and requires time intensive inspection techniques to be used, which are often very costly (Sensburg (1993)). It has been shown that, for low impact energies, composite laminates suffer a greater strength loss in compression than in tension (Hull and Shi (1993)), see figure 1.3.1. For this reason, post-impact compressive strength has become the norm for assessing a laminates damage tolerance (Soutis and Curtis (1996), Davies *et al.* (1996)).

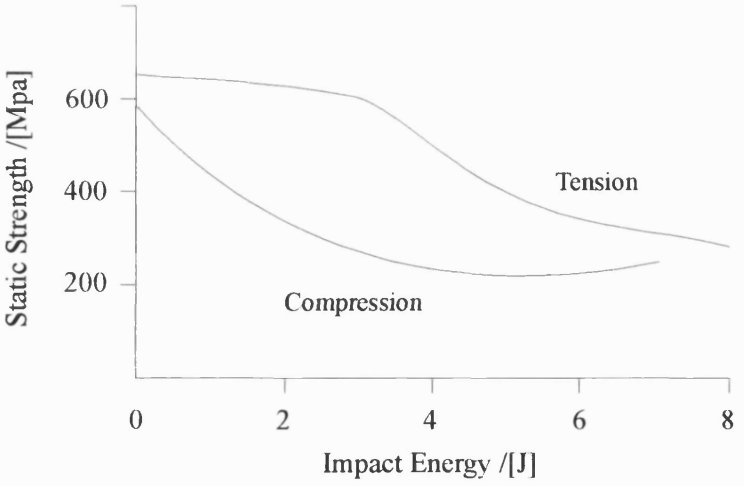

Figure 1.3.1 – Post-impact tensile and compressive strength reductions of a $[0°,90°,\pm45°,0]_s$ laminate (Hull and Shi (1993))

Although a complex mechanism, the BVID process has been investigated widely using such methods as ultrasonic B-scanning (which builds up a quasi-3-D representation of the damaged area), and C-scanning, and is becoming increasingly understood. An example C-scan image of an impacted laminate is shown in figure 1.3.2.

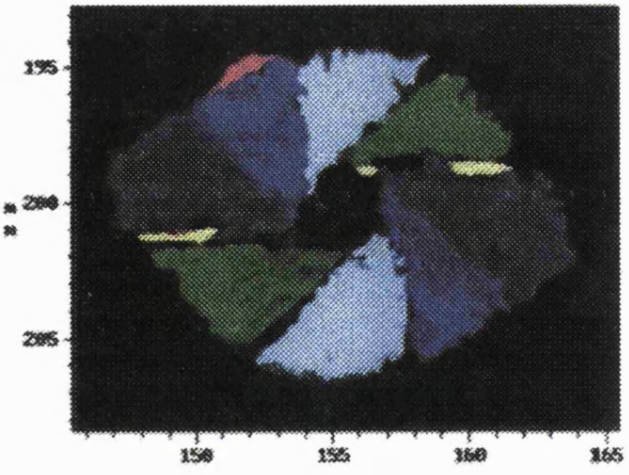

Figure 1.3.2 - C-Scan Image of a composite material with impact damage (Gundtoft and Borum (1999))

The predominant damage modes in BVID are intraply cracking and delamination. An impact produces a transverse shear stress field that initiates intraply cracking. These cracks propagate through the laminate, until they reach adjacent plies with different fibre orientations. The cracks then deviate into delaminations (Shi and Hull (1992)), which is the mechanism that dissipates the most energy. The formation of intraply cracks and delaminations is dependent upon the laminate geometry and gives a distinctive damage pattern. An idealised delamination pattern for the –45°/+45° layers in a 0°/-45°/45° laminate is shown in figure 1.3.3. Here, the intraply cracks have propagated through the top 0° layer (not shown), and formed a delamination at the interface of the 0°/-45° plies. A delamination has also been formed at the interface of the –45°/45° plies, which is rotated 90° to the preceding delamination.

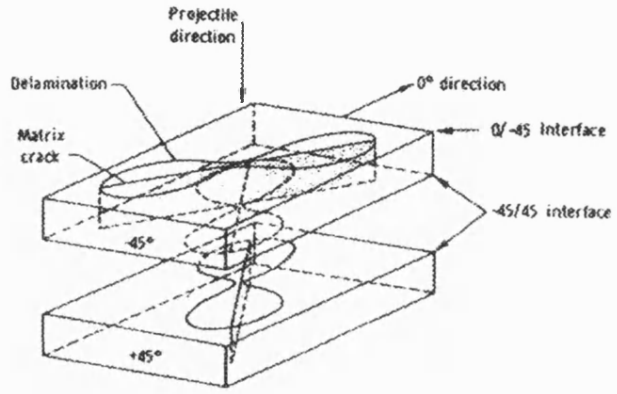

Figure 1.3.3 - Delamination pattern in a 0°/-45°/+45° laminate caused by impact (Soutis and Curtis (1996))

Of particular relevance to this research is the effect of impact damage on the dynamic properties of composite laminates. Tracy, Dimas, and Pardoen (1985) investigated the frequency drop and mode-shape change for BVID in sixteen ply laminates with a range of geometries. They found that impact damage reduced the natural frequency of vibration significantly for high frequencies (Tracy and Pardoen (1989)), with a smaller frequency shift for lower order modes. They remarked that the drop in frequencies would be a useful indicator of BVID, and might be a useful method of characterising such damage.

1.4 Structural Modelling of Composite Laminates

1.4.1 Vibration Analysis of Composite Laminates

Much work has gone into modelling the vibration of composite materials, because of the coupling between different types of deflection due to rotated plies. In an early paper, Abarcar and Cunniff (1972), presented experimental results for carbon- and boron-fibre beams with 0°, 15°, 30° and 90° ply angles. They noticed significant effects of bending-twisting coupling for the 15° and 30° beams, which agreed well with their theoretical model of bending modes. Teoh and Huang (1977) derived the equations of motion for three degrees of freedom of an anisotropic beam, and Teh and Huang (1980) used them to show the effects of fibre orientation on the natural frequencies of carbon/epoxy cantilever beams. Later, Banerjee (1989) derived the expressions for the dynamic stiffness matrix of a beam with coupled bending and twisting motion. Coupled to the Wittrick-Williams algorithm, which quickly and accurately calculates the undamped natural frequencies of a structure given the dynamic stiffness matrix (Wittrick and Williams (1971), Williams and Wittrick (1983)), good agreement was seen with experimental results. Coupling the dynamic stiffness matrix with the Wittrick-Williams algorithm is known as the Dynamic Stiffness Method (DSM). This has shown good accuracy, and significant processor time savings compared to finite element methods (Banerjee and Williams (1995)), which are used extensively to model the dynamics of composite laminates (Chai *et al.* (1993)). The DSM has been improved over the years to include the effects of warping of thin-walled and open section beams (Banerjee, Guo and Howson (1994)), and the effects of shear deformation and rotary inertia (Banerjee and Williams (1996)). The latter model was used in this research.

The effects of transverse shear is more pronounced for plate structures than for beams, especially where the transverse shear modulus is small in relation to the extensional modulus, as well as for thick plates. Kapania and Lovejoy (1996) presented results for the free vibration, and Farag and Pan (1998) for forced, in-plane, vibration of such plates. The former authors showed that overestimation of the natural frequencies occurs if shear deformation is not taken into account.

1.4.2 Vibration Analysis of Delaminated Composite Laminates

1.4.2.1 Based on Static Analysis

The DSM models a beam as a number of interconnecting elements with known properties. This allows a delamination to be modelled as one or more elements with a lower rigidity than the rest of the beam. A number of static models of delaminated laminates have been presented that could

be used for this. O'Brien (1985) investigated delaminated laminates to determine strain energy release rates, and developed a simple method of determining the axial stiffness and strength of delaminated plies. Shi and Hull (1992) developed a beam model of a delamination to determine the strain energy release rate. This calculated the forces and static deflection of the sub-laminates, from which static stiffness properties can theoretically be determined.

Chan and Chou (1995) used classical laminate analysis and the parallel axis theorem to determine values of effective bending and axial stiffness of delaminated laminates, and also determined the effects of ply fibre waviness on the stiffness of laminates. However, the results in this thesis do not support the conclusions of the first method.

1.4.2.2 Based on Dynamic Analysis

Much work has been carried out to analytically determine the effects of delamination on the vibrational behaviour of cracked isotropic or delaminated composite beams. In an early work, Ramkumar *et al.* (1979) modelled an isotropic beam with a full-width delamination as four Timoshenko beams connected at the delamination edges. Wang *et al.* (1982) improved on this model by including the coupling between longitudinal and bending vibration. Later, Mujumdar and Suryanarayan (1988) developed a "constrained mode" model of a delaminated composite beam, which included contact between sub-laminates. They concluded that the constrained model showed better results than "free" models, where no contact between sub-laminates is modelled, when the delamination is large and the friction correspondingly more significant. Tracy and Pardoen (1989) investigated the effects of delamination size and position within composite beams, and compared the results for the first four bending modes with experiment. Only the first bending mode of vibration was investigated by Shen and Grady (1992), but results of local opening modes of vibration were given.

More recently, Luo and Hanagud (1997) calculated the dynamic response of delaminated beams using a combined free and constrained model, using linear springs to model contact between sub-laminates, and Yin and Jane (1992) calculated the modes of vibration of delaminated pre-buckled composite laminates.

Contrasting with the "exact" analytical methods, there has also been extensive research making use of Finite Element (FE) methods. Tracy *et al.* (1985) compared experimental results with FE results for plates with impact damage. They found significant frequency reductions for high frequency modes. This was also found by Tenek *et al.* (1993), who used the heat generated by the

friction between sub-laminates in high frequency opening modes to non-destructively detect delaminations. Averill (1993) used zig-zag elements that, with only four degrees of freedom per laminate, offer significant computer processor time savings for laminates with a large number of plies. A better accuracy than discrete-ply FE models was also seen, due to the stress averaging used by the latter.

Gandelrab (1996) used a special FE model of 2-lamina laminate to model a delamination, and presented frequencies and mode-shapes of the first three bending modes of beams. Reductions in cantilever first bending frequency of up to 40% were noted for a centreline delamination 25% of the beam length. Smaller reductions were seen by Krawczuk *et al.* (1997), who gave results for bending frequencies and mode-shapes with varying delamination size and position. This was later extended to include contact between sub-laminates (Zak *et al.* (1999)).

1.5 Non-Destructive Testing

Non-Destructive Testing (NDT) is an on-going area of research in the aerospace community. Because damage in composite materials can be difficult to detect by the naked eye, manual inspection must either be augmented by methods such as double pass retroreflection (Forsyth *et al.* (1998)) or laser highlighting (Ghoshal (1999)) for example, or inspection must take place using other means. Damage can either be detected as it occurs using structural health monitoring systems (Boller *et al.* (1996), Crawley (1994), Bartkowicz *et al.* (1996)), or detected using a NDT technique. This section gives a brief overview of some of the current NDT methods.

One popular inspection technique is ultrasonic scanning (Gundtoft and Borum (1999)). In this technique, a transducer transmits ultrasonic waves, through some intermediate medium, to the structure being examined. Because ultrasound is not transmitted through air, a delamination does not allow the ultrasonic waves to pass through the structure. A receiver is placed either to record un-obstructed sound waves, or to record reflected waves. In an A-scan, an ultrasonic receiver records the reflected sound to register the delamination. Recording the time taken for the wave to be reflected back to the receiver allows the calculation of the depth of the damage, and a 3-D image to be built up. Two problems with ultrasonic techniques are that the technique is quite slow, due to the fact that only a small area can be scanned, and that the liquid coupling between the transducer and the test structure may be detrimental to the composite material.

Transient thermography solves the first of these problems, as it is a technique that scans large areas of the test structure. In this process, the test structure is heated via a number of methods, including flash lamps, microwave heating, eddy current heating or hot air blowers (Almond *et al.* (1996)). A delamination impedes the conduction of heat into the structure, resulting in an area that radiates more heat than the rest of the structure. A thermal imaging camera is then used to determine the local hot area, which locates the damage. Ball and Almond (1998) showed that transient thermography is able detect damage in thick laminates, but the technique is susceptible to low signal to noise ratios during on-site inspection due to parasitic heat sources. However, some parasitic heat sources can be filtered out (Braggiotti *et al.* (1998)).

X-radiography is also used as a NDT technique, although its use is limited by the necessity of having access to the rear of the component for the radiation detector (Kelly (1994)). The X-radiation technique is based on the fact that differences in material, whether porosity, difference in thickness, or the presence of foreign bodies in the material, show differences in absorption of penetrating radiation. Cracks and delaminations are difficult to detect using X-radiation because the defect must have an appreciable thickness in the plane of the radiation, and hence they are highly dependant upon their orientation. However, they can be detected if a radio-opaque penetrant is introduced into the material, which highlights the damage. However, this may in itself damage the composite material.

When a structure is damaged, its structural integrity is altered, which alters its surface deformation when stressed. Digital shearography (Findeis and Gryzagoridis (1999)) focuses a monochromatic light source on the structure, and through a mirror shearing device, a speckle pattern image of the unstressed image is recorded. The structure is then stressed, using a variety of methods, which alters the intensity of the image. Comparing the two images results in a fringe pattern that highlights the damage.

Although not a NDT technique *per se*, some mention should also be given to acoustic emission, because the technique can measure damage as it occurs, and does not require additional stressing of the material. An acoustic emission occurs when an elastic stress wave is released during the propagation of cracks, delaminations, friction or microscopic deformation. In acoustic emission (Ziehl (1999)), a 10 kHz – 1 MHz piezoelectric sensor is used to measure damage events either as they occur, or during test loading. Acoustic emission has the disadvantage that it is unable to quantify accurately the size of damage, but can only monitor its presence.

1.5.1 NDT via Modal Analysis

Much of the research into the effects of delamination on the dynamic characteristics of composite laminates has been carried out to produce models for the purpose of NDT. From an early stage, it was recognised that modal analysis has significant advantages over other NDT techniques. Cawly and Adams (1979) pointed out that measuring the dynamic behaviour of a structure is potentially very attractive for NDT, because dynamic properties can be measured at one point of the structure. A time-consuming scan of the whole structure is therefore not necessary. For this reason, NDT using modal parameters receives considerable interest in the aerospace industry (Shen *et al.* (1998), Boller (1994)).

Potentially, measurements of natural frequencies, mode-shapes and damping parameters can be used for NDT. Damping increases with most types of damage, due to the energy dissipation resulting from internal friction of the damage area. However, most modal NDT techniques use frequency and mode-shape data, because there is still some uncertainty as to how sensitive damping is to damage. For instance, after a study of stiffened composite panels, Vantomme (1992) did not notice significant damping changes for a wide range of damage types that caused significant reductions in frequency. It is also difficult to obtain damping measurements for highly coupled modes, and to differentiate material damping from structural damping, which contributes a much greater percentage to the whole (Shelby, Tai and Jang (1991)).

A high proportion of NDT research using modal analysis has been carried out on lattice or frame type structures. Adams *et al.* (1991) investigated the effects of different types of damage, ranging from saw cuts to impact damage, on a glass-fibre-reinforced plastic structure. They noticed frequency and mode-shape changes greater than the baseline undamaged results for all damage types. Cobb and Liebst (1997) used a partial set of eigenvalues and vectors to detect the majority of damage in a NASA truss structure, minimising a cost function based on the eigendata. Hajela and Soeiro (1990) used a gradient-based optimisation method to minimise the difference between results from undamaged and damaged FE models, simulated by extensional and shear rigidity reductions. A similar method was also used by Hassiotis and Jeong (1993) (1995), who also applied this to beams. Baruh and Ratan (1993) calculated a residual matrix for truss structures, which, by inspection of its elements, directly located either stiffness or mass reductions.

Investigating damage within beams, Banks et al. (1996) developed and experimentally verified a NDT technique, which minimised the difference in the time-decaying response for an aluminium beam excited by piezoelectric patches. Drilled holes were successfully located within the beam.

Ruotolo and Surace (1996) (1997) incorporated an FE model into a genetic algorithm to investigate different types of objective function to detect damage in cracked beams. Multiple cracks in steel beams were successfully located. Pandey *et al.* (1991) and Ratcliffe (1997) both used mode shape data to detect damage. The former researchers used the local curvature of the mode-shapes to highlight damage, simulated by a 50% drop in Youngs' modulus in a FE model. Similarly, the latter researcher used a modified Laplacian operator to highlight the damage. Neither technique requires an initial analytical model to detect damage.

In his PhD work, Sensburg (1993) created an FE model of beams, and then a model aircraft fin to detect area reductions and holes. He used a gradient-based optimisation method to update the stiffness matrix of the FE model to detect the damage.

By far the greatest amount of NDT work using modal analysis has approximated damage as stiffness or area reductions. (The brief literature survey above does not do justice to the scope of the research: Abé (1996), Casas and Aparicio (1994), Hassiotis and Jeong (1995) are a few more examples which do not fit neatly into the discussion.) Comparatively little research has been undertaken to specifically locate delaminations. Ratcliffe and Bagaria (1998) used a cubic polynomial fit to mode-shapes, using curvature elements. The "gapped" element, which is the element not used to fit the polynomial, is used in a damage index. The technique located damage in experimental delaminated glass-fibre beams, which the technique by Pandey *et al.* was not able to detect. Luo and Hanagud (1997) obtained the dynamic response of a set of experimental glass-fibre beams with Teflon patches inserted to simulate delaminations. This was used to train a neural network, which could then detect damage. A neural network was also used by Okafor *et al.* (1995), who used the first four bending frequencies produced by an analytical model similar to Tracy and Pardoen (1989) as training data. The neural network subsequently detected 2-inch long experimental delaminations in 10.5-inch long glass-fibre beams. Saravanos *et al.* (1994) used exact solutions of the equations of motion for a composite with a piezoelectric layer. They successfully located delaminations, which were 20% of the beams length, in experimental carbon-fibre beams with different lay-ups using distributed piezoelectric sensors.

1.6 Characterisation of Structures by Modal Analysis

Structural characterisation is the method of determining the material and structural properties of vibrating structures. Structural characterisation via modal analysis is used as an alternative to more traditional static methods such as tensile or bending tests. Araujó *et al.* (1995) used a

higher-order plate FE model to determine the eigenfrequencies of a free-free plate. The difference between these and experimental frequencies were minimized using a gradient-based optimisation method to determine six material parameters. Larsson (1991) used Timoshenko beam theory to determine the optimum dimensions of beams used to minimise errors in structural characterisation. Figure 1.6.1 shows normalised free-free eigenfrequencies against the ratio of shear modulus to Young's modulus for beams of different dimensions. As the ratio of length to thickness of the beam increases, higher order modes must be used to ensure accuracy. Also, high ratios of shear to Young's modulus result in a lower accuracy. Similarly, Ip and Tse (1999) used Timoshenko beam theory and an iterative procedure to determine the material properties of a free-free beam. They devised an equation to estimate the errors involved in calculating the shear and Young's modulus, and determined that the error in determining the shear modulus was always greater than for the Young's modulus.

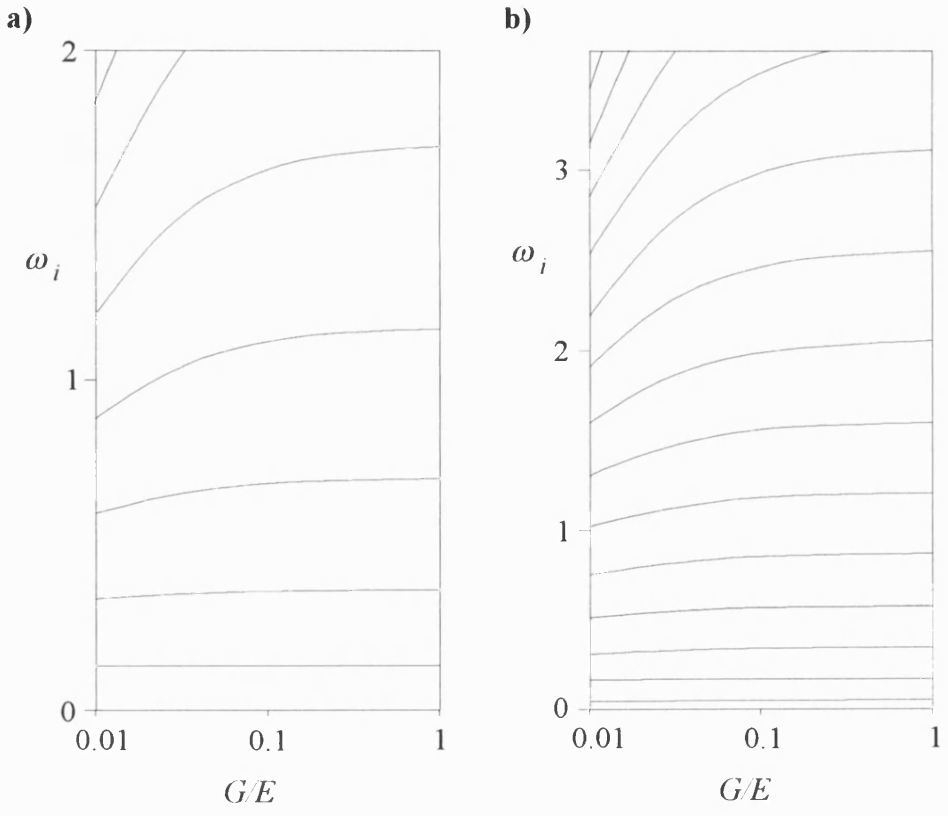

Figure 1.6.1 – Dimensionless frequencies ω_i versus *G/E* (Larsson (1991))

a) Length/Thickness = 50 b) Length/Thickness = 100

Using energy methods to derive the equations of a thin orthotropic plate, McIntyre and Woodhouse (1988) measured the elastic and damping constants of a variety of materials. The Young's and shear moduli could then be determined from these constants.

Model updating, which can be thought of as a sub-set of structural characterisation, is a common method of improving the accuracy of vibration models. Friswell et al. (1997) updated the stiffness and damping matrices of an FE model via equations calculated from the Langrangian of a penalty function. They demonstrated reasonable results with a numerical example, but the process showed potential problems of introducing extra modes within frequency range of interest, and de-stabilising other modes by introducing negative damping.

1.7 Numerical Optimisation

As discussed in the previous sections, both NDT and structural characterisation methods based on modal analysis often use numerical optimisation techniques (Hajela and Soeiro (1990), Ruotolo and Surace (1996) (1997), Hassiotis and Jeong (1993) (1995), Sensburg (1993), Araujó *et al.* (1993)). Optimisation methods have been under development for more than thirty years, but the industrial applications of such methods remains small (Butler (1998)).

The optimisation process can be stated as, "to choose the variables in a design process so as formally to achieve the best value of some performance index while not violating any of the associated conditions or constraints" (Ashley (1982)). This definition encompasses a wide range of applications; in the aerospace industry alone aerodynamic, structural and control optimisation for example, is possible. The Wright brothers' Flyer 1 again gives an early example, when they investigated the lift to drag ratio of sixty wing models in their wind tunnel, which, in the words of Wilbur Wright himself, "... renders the search for the best shapes much easier". They chose Model no. 12, giving a maximum lift to drag of 9.5.

The choice of optimisation technique depends on the design problem for which it is to be used, and can be thought of a compromise between speed and robustness. Goldberg (1989) illustrates this principle with a 'problem spectrum', shown in figure 1.7.1. Here, an idealised value of efficiency for different optimisation methods is plotted for different problem types. The optimisation methods are classified by three types; random walks or enumerative schemes, specialised schemes, and robust schemes. The first set of optimisation schemes involves sampling the whole design space, and is therefore very robust, but has low efficiency. An enumeration

scheme involves sampling the design space at regular intervals, and a random walk involves sampling the design space randomly. These methods are attractive for their simplicity, but are usually discounted as serious optimisation methods for their low efficiency.

The 'specialized scheme' defined by Goldberg includes gradient-based optimisation methods. Gradient-based methods (sometimes known as hill-climbing methods) are a commonly used optimisation technique, which rely on the presence of local gradients at sampled points of the design space. Research using gradient-based optimisation techniques has been widespread, but restricting the review to the field of aerospace gives an indication of their applications.

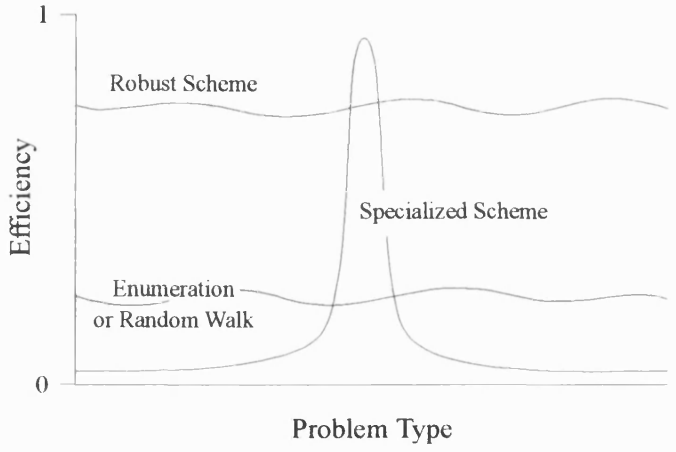

Figure 1.7.1 – Idealised representation of a 'problem spectrum', showing the efficiency of different optimisation schemes for different problem types (Goldberg (1989))

For example, Butler *et al.* (1995) presented results from a computer code that produced a minimum-mass preliminary wing design with constraints on flutter speed and divergence speed, using a gradient-based optimisation method. Their wing design showed a 32% reduction in mass compared to the initial design. Butler and Banerjee (1996) also compared minimum-mass designs for beams and wing box structures. These were constrained by separation of the first bending and first torsional modes of vibration and constrained by flutter and divergence speeds. They found that designs based on flutter and divergence speeds were lighter than designs constrained by frequency separation (which is the traditional method of designing wings with sufficient flutter speeds – classical flutter being the coelesance of these modes at a certain speed). This led Taylor *et al.* (1999) to suggest a two-stage method, which optimised composite wind-tunnel wing models

firstly for frequency separation, and then for flutter and divergence speeds. This achieved the optimum designs in terms of both mass, and flutter onset "hardness", and showed significant computer processor time savings.

For more complex problems, a gradient-based optimisation technique becomes insufficient, and a 'robust scheme' becomes desirable. Goldberg includes simulated annealing (Shim and Manoochehri (1997)) and genetic algorithms (GAs) as robust schemes. Because of their inherent robustness, GAs can be used for more complex problems. These range, for example, from traditional structural optimisation (Goto and Yokoyama (1999)), to design of complicated control processes (Donne et al. (1995)). In the area of aerospace applications, Quagliarella and Cioppa (1999) designed transonic aerofoils for low drag at a specific mach number and lift coefficient, using a GA. Later, Takahashi *et al.* (1999) designed aerofoils and wing-planforms for similar constraints.

1.8 Summary of the Research

At the University of Bath much confidence has arisen about the accuracy and applicability of the Dynamic Stiffness Method (DSM) introduced previously in this chapter. As part of his PhD, Taylor (1998) confirmed that the DSM was as accurate as FE models for predicting the natural frequencies of composite beams, and was up to two orders of magnitude faster. The computational efficiency of the DSM means that it is ideal for structural optimisation, where multiple solutions of a design must be obtained. Williams *et al.* (1991) used the DSM to design optimum stiffened panels with buckling constraints, and Lillico *et al.* (1997) incorporated the DSM to obtain preliminary designs of aircraft wings with minimum mass.

After gaining initial experience of aeroelastic optimisation using the DSM (Taylor *et al.* (1999)), the current author began work on NDT using vibrational analysis. Code was developed which calculated the stiffness of composite laminates using classical laminate analysis. This was incorporated into the Timoshenko beam DSM (Banerjee and Williams (1996)) to calculate their free vibration frequencies and mode-shapes. A delamination was initially modelled as a reduction in bending stiffness via the procedure outlined by Chan and Chou (1995). The structural optimisation method, the Modified Method of Feasible Directions (MMFD), contained within the commercially available software package DOT (Vanderplaats Research & Development, Inc. (1995)) was incorporated into the code. This minimised the difference between the experimentally

produced vibrational response with that produced by the DSM, by varying the size and location of the delaminations.

Initial results provided by the model, however, did not agree well with initial results obtained experimentally and by FE analysis. This was due to incorrect modelling of the delamination, and a corrected model based on the static deflection of two beams was later developed (Harrison and Butler (1999)). When incorporated into the DSM, this gave vibration results that agreed with FE analysis and with the available literature.

Results obtained from using analytical input data to simulate experimental data, suggested that the MMFD could locate delaminations within composite beams, but might find locally-minimum solutions. This problem, combined with the fact that delaminations are located at discrete ply locations, suggested the use of a Genetic Algorithm (GA) as the optimising method. The GA used was the shareware code GENISIS (Grefenstette (1990)). This successfully located delaminations within composite laminates using experimental vibration data, showing some advantages over the gradient-based optimising method (Harrison and Butler (2000)).

2. Analysis and Modelling of Delaminated Beams

This chapter deals with the structural models used to describe the behaviour of the composite beams. A summary of the calculations used to determine the stiffness properties of the laminates and their incorporation into the Dynamic Stiffness Method is given. The static beam model of a delaminated section, and its use to determine the effective shear and torsional rigidities, is described. The finite element models used to verify the results are also outlined.

2.1 Free Vibration Analysis Using the Dynamic Stiffness Method

The free vibration frequencies and mode-shapes are calculated using the Dynamic Stiffness Method (DSM). This is incorporated in a computer code developed by Dr. J.R.Banerjee of City University, London. The DSM theory has been summarised here for reference as much of the later work in this thesis has been constrained by the assumptions and limitations of the DSM, but a much more complete understanding can be obtained by referring to the literature (Wittrick and Williams (1971), Williams and Wittrick (1983), Banerjee (1989), Banerjee and Williams (1995), Banerjee *et al.* (1996), Banerjee and Williams (1996)).

The DSM uses the solutions of the equations of motion of a structure to assemble a stiffness matrix $[K]$. Each element of $[K]$ is a transcendental function of the circular frequency ω, which is a natural frequency of the structure when the determinant of the matrix is zero. Because the beam is assumed to have a continuous distribution of mass and rigidity along its length, the procedure allows for an infinite number of degrees of freedom. Therefore, as many natural frequencies as desired can be obtained without increasing the number of elements in the model. This is in contrast to Finite Element (FE) methods, which discretise the model by lumping distributed masses at nodes. Only a finite number of modes of vibration can be obtained, this number being the number of degrees of freedom of the model. In addition, the solution becomes more inaccurate for higher order modes, and increased accuracy can only be obtained by increasing the number of nodes of the structure. This increases the time necessary for analysis. Therefore the DSM is much more suitable to structural optimisation, where the solution must be found many times. However, this is only true as long as the problem can be approximated to a simple structure. The DSM is limited to structures that can be approximated as beams and plates (Williams *et al.* (1991)) with different boundary conditions, and only calculates modes of vibration (and buckling) where the whole structure undergoes vibration (or buckling). FE methods, although more computationally

expensive, are able to model more complicated structures, and can obtain solutions for local modes of vibration, where only small sections of the structure undergo vibration.

The DSM used in this research includes the effect of bending-torsion material coupling, shear deformation, and rotary inertia; i.e. Timoshenko beam theory. However, the effects of warping, and other types of coupling, (e.g. bending-axial coupling), are neglected in the formulation of the matrix. The limitation of no axial coupling restricts the types of beams considered to symmetric lay-ups, which can however be unbalanced.

The governing partial differential equations of motion for the beam shown in figure 2.1.1 (Banerjee and Williams (1996), Teoh and Huang (1977), Teh and Huang (1980)) are:

$$EI\frac{\partial^2\theta}{\partial y^2}+kAG\left(\frac{\partial h}{\partial y}-\theta\right)+K_{BT}\frac{\partial^2\psi}{\partial y^2}-\rho I\frac{\partial^2\theta}{\partial t^2}=0 \qquad \ldots (2.1.1)$$

$$kAG\left(\frac{\partial^2 h}{\partial y^2}-\frac{\partial\theta}{\partial y}\right)-m\frac{\partial^2 h}{\partial t^2}=0 \qquad \ldots (2.1.2)$$

$$GJ\frac{\partial^2\psi}{\partial y^2}+K_{BT}\frac{\partial^2\theta}{\partial y^2}-I_\alpha\frac{\partial^2\psi}{\partial t^2}=0 \qquad \ldots (2.1.3)$$

where EI is the bending rigidity, GJ is the torsional rigidity, kAG is the shear rigidity, and K_{BT} is the bending-torsion coupling rigidity of each element. Also, t is time, ρ is the density, I is the second moment of area of the beam, m is the mass per unit length, I_α is the polar mass moment of inertia per unit length about the Y-axis, h is the flexural translation in the z-direction, ψ is the torsional rotation about the Y-axis, and θ is the angle of rotation in radians about the X-axis due to bending alone. The total slope $\frac{\partial h}{\partial y}$ equals the sum of the slopes due to bending and to shear deformation.

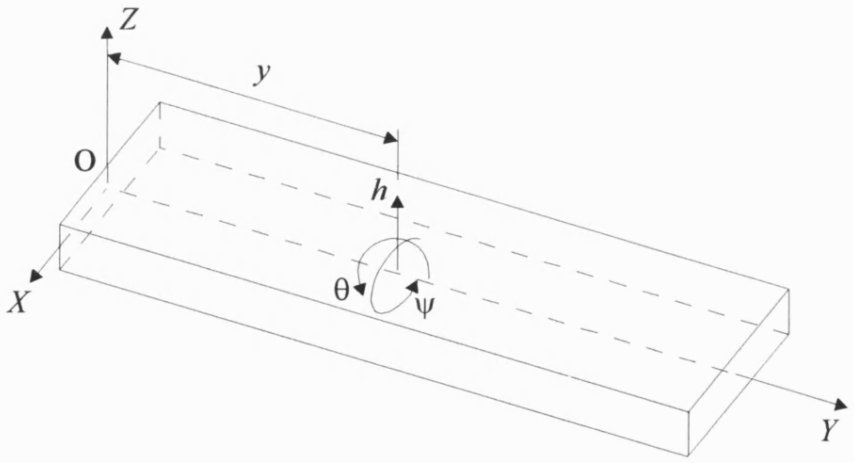

Figure 2.1.1 - The co-ordinate system and notation for a composite Timoshenko beam

It is assumed that h, θ and ψ vary sinusoidally with circular frequency ω, so that:

$$h(y,t) = H(y)\sin\omega t \qquad \ldots (2.1.4)$$

$$\theta(y,t) = \Theta(y)\sin\omega t \qquad \ldots (2.1.5)$$

$$\psi(y,t) = \Psi(y)\sin\omega t \qquad \ldots (2.1.6)$$

where $H(y)$, $\Theta(y)$ and $\Psi(y)$ are the amplitudes of vertical displacement, bending rotation and twist, respectively.

By substituting equations (2.1.4) - (2.1.6) into (2.1.1) - (2.1.3), a differential equation for any one of H, Θ or Ψ can be found. These are solved with the knowledge of the relevant end conditions, the beam displacements and forces, shown in figure 2.1.2. The solutions to these equations yield the force displacement relationship for each beam element, the dynamic stiffness matrix:

$$[F]=[K][U]$$

or:

$$\begin{bmatrix} S_1 \\ M_1 \\ T_1 \\ S_2 \\ M_2 \\ T_2 \end{bmatrix} = \begin{bmatrix} K_{11} & K_{12} & K_{13} & K_{14} & K_{15} & K_{16} \\ & K_{22} & K_{23} & K_{24} & K_{25} & K_{26} \\ & & K_{33} & K_{34} & K_{35} & K_{36} \\ & & & K_{44} & K_{45} & K_{46} \\ & Symm. & & & K_{55} & K_{56} \\ & & & & & K_{66} \end{bmatrix} \begin{bmatrix} H_1 \\ \Theta_1 \\ \Psi_1 \\ H_2 \\ \Theta_2 \\ \Psi_2 \end{bmatrix}$$

The individual terms of the dynamic stiffness matrix can be obtained from Banerjee and Williams (1996).

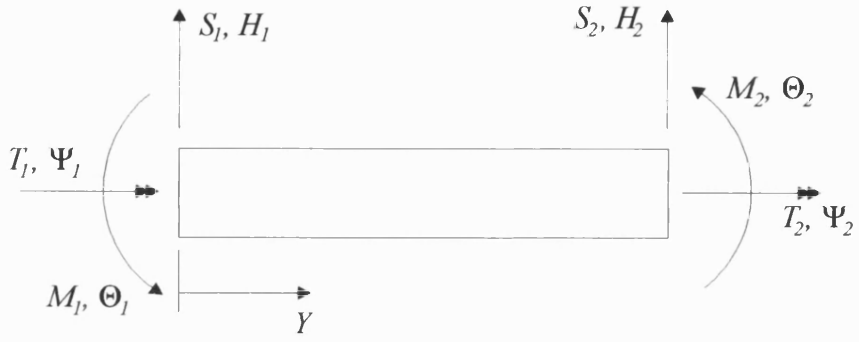

Figure 2.1.2 - End conditions for forces and displacements of the beam element

The natural frequencies are obtained using the algorithm of Wittrick and Williams (1971), which solves the equation of the form:

$$[K][U] = [0]$$

The number of natural frequencies (found by counting the number of negative leading diagonal elements of the upper triangle matrix of $[K]$) exceeded by a trial frequency, is obtained. A value for natural frequency is found when this number increments. This method is attractive because, using a bisecting algorithm for example, any number of natural frequencies can be found to any accuracy desired, independent of the number of elements in the model.

2.2 Calculation of Beam Element Properties

When using the DSM, the beam is split up into elements, for each of which the element properties required for equations (2.1.1) to (2.1.3) are known. These properties are calculated using classical laminate analysis, which is outlined in many textbooks (For example see Tsai and Hahn (1980)).

2.2.1 Laminate Analysis

For a plate consisting of n layers, the load-deflection relationships are expressed as:

$$\begin{bmatrix} N \\ M \end{bmatrix} = \begin{bmatrix} A & B \\ B & D \end{bmatrix} \begin{bmatrix} \varepsilon \\ \kappa \end{bmatrix}$$

where $[N]$ is the vector of direct and shear loads per unit width, $[M]$ is the vector of bending and torsional moments per unit width, $[\varepsilon]$ the vector of in-plane and shear strains, and $[\kappa]$ the vector of the curvatures of the mid-plane of the plate. The stiffness matrices $[A]$, $[B]$ and $[D]$ are obtained from:

$$A_{ij} = \int_{-d/2}^{d/2} Q_{ij}^{k'} dz \; ; \; B_{ij} = \int_{-d/2}^{d/2} Q_{ij}^{k'} z dz \; ; \; D_{ij} = \int_{-d/2}^{d/2} Q_{ij}^{k'} z^2 dz$$

$$i = 1...6; \; j = 1...6$$

where $Q_{ij}^{k'}$ denote the elements of the transformed off-axis lamina modulus of the kth ply with angle θ_{ply}. For the purpose of this research, a ply angle of 0° is defined along the Y-axis, with negative angles towards the X-axis, as shown in figure 2.2.1. The variable $d/2$ is the distance from the mid-plane to the upper surface of the laminate.

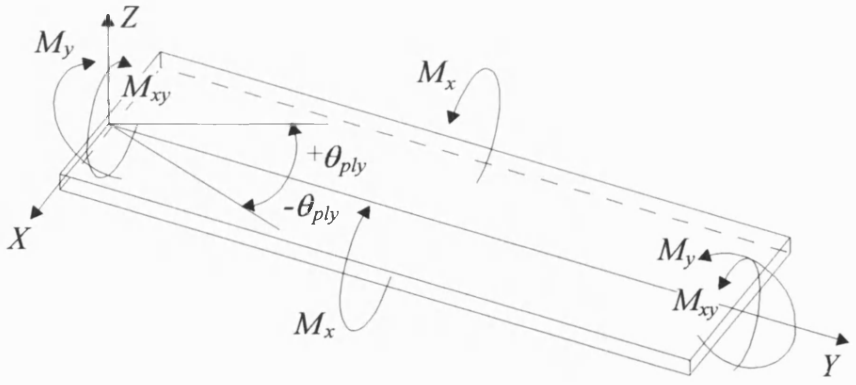

Figure 2.2.1 - Co-ordinate system and positive ply angle for laminate analysis.

For the bending-extension coupling terms, the axial stiffness and the shear rigidities used in the static beam analysis of the delaminated sections, the full 3-D stiffness matrices of laminates made up of plies with three mutually orthogonal planes of symmetry are used:

$$\begin{bmatrix} N_x \\ N_y \\ N_z \\ Q_{xy} \\ Q_{yz} \\ Q_{zx} \\ M_x \\ M_y \\ M_z \\ M_{xy} \\ M_{yz} \\ M_{zx} \end{bmatrix} = \begin{bmatrix} A'_{11} & A'_{12} & A'_{13} & 0 & 0 & A'_{16} & B'_{11} & B'_{12} & B'_{13} & 0 & 0 & B'_{16} \\ & A'_{22} & A'_{23} & 0 & 0 & A'_{26} & B'_{21} & B'_{22} & B'_{23} & 0 & 0 & B'_{26} \\ & & A'_{33} & 0 & 0 & A'_{36} & B'_{31} & B'_{32} & B'_{33} & 0 & 0 & B'_{36} \\ & & & A'_{44} & A'_{45} & 0 & 0 & 0 & 0 & B'_{44} & B'_{45} & 0 \\ & & & & A'_{55} & 0 & 0 & 0 & 0 & 0 & B'_{55} & 0 \\ & & & & & A'_{66} & 0 & 0 & 0 & 0 & 0 & B'_{66} \\ & & & & & & D'_{11} & D'_{12} & D'_{13} & 0 & 0 & D'_{16} \\ & & & & & & & D'_{22} & D'_{23} & 0 & 0 & D'_{26} \\ & & \textit{Symm.} & & & & & & D'_{33} & 0 & 0 & D'_{36} \\ & & & & & & & & & D'_{44} & D'_{45} & 0 \\ & & & & & & & & & & D'_{55} & 0 \\ & & & & & & & & & & & D'_{66} \end{bmatrix} \begin{bmatrix} \varepsilon_x \\ \varepsilon_y \\ \varepsilon_z \\ \gamma_{xy} \\ \gamma_{yz} \\ \gamma_{zx} \\ \kappa_x \\ \kappa_y \\ \kappa_z \\ \kappa_{xy} \\ \kappa_{yz} \\ \kappa_{zx} \end{bmatrix} \quad \ldots (2.2.1)$$

The derivation of the Q'_{ij} terms for an orthotropic ply, together with the transformations for ply angle θ_{ply}, can be found in the textbook by Christensen (1979) (Note: With the definition of ply angle as shown in figure 2.2.1, the ply angle θ_{ply}, must be rotated by $-\frac{\pi}{2}$ to remain consistent with the ply angle in Christensen, θ. i.e. $\theta = \theta_{ply} - \frac{\pi}{2}$)

For the bending rigidity, torsion rigidity, and bending-torsion coupling rigidity, it is assumed that the laminate is symmetric so that $[B]=0$. It is also assumed that the laminate has a state of plane stress. The 6x6 matrices can then be reduced to 3x3 form (Christensen (1979)), giving (for the bending stiffness matrix $[D]$):

$$\begin{bmatrix} M_x \\ M_y \\ M_{xy} \end{bmatrix} = \begin{bmatrix} D_{11} & D_{12} & D_{16} \\ D_{21} & D_{22} & D_{26} \\ D_{61} & D_{62} & D_{66} \end{bmatrix} \begin{bmatrix} \kappa_x \\ \kappa_y \\ \kappa_{xy} \end{bmatrix} \quad \ldots (2.2.2)$$

where the axes and directions of positive moment are shown in figure 2.2.1. It should be noted that the elements of the plane stress stiffness matrix are not equivalent to the elements of the 3-D matrix i.e. $D'_{ij} \neq D_{ij}$.

2.2.2 Bending Stiffness, Torsional Stiffness and Bending-Torsion Coupling

The bending rigidity, torsional rigidity and bending-torsion coupling rigidity are found using the high aspect ratio plate model outlined by Weisshaar and Foist (1985). For this model, it is assumed that the relationship between the bending moment and torque, and beam curvature and twist rate, is expressed as:

$$\begin{bmatrix} M \\ T \end{bmatrix} = \begin{bmatrix} EI & -K_{BT} \\ -K_{BT} & GJ \end{bmatrix} \begin{bmatrix} \dfrac{\partial^2 h}{\partial y^2} \\ \dfrac{\partial \psi}{\partial y} \end{bmatrix} \quad \ldots (2.2.3)$$

where the relationships between the resultant moments on the beam and those on the plate cross section, as shown in figure 2.2.1, are:

$$M = -bM_y \quad \ldots (2.2.4)$$
$$T = -2bM_{xy}$$

where b is the width of the plate, and the chordwise moment M_x is assumed to be zero. The plate curvatures are approximated as:

$$\kappa_y \approx -\frac{\partial^2 h}{\partial y^2} \quad \ldots (2.2.5)$$

$$\kappa_{xy} \approx 2\frac{\partial^2 h}{\partial x \partial y}_{x=0} = -2\frac{\partial \psi}{\partial y}$$

where h is the deflection of the mid-plane of the plate (i.e. at x=0). Using equations (2.2.4) and (2.2.5) in (2.2.2), expressions for the desired rigidities can be determined:

$$EI = b\left[D_{22} - \frac{D_{12}^2}{D_{11}}\right] \quad \ldots (2.2.6)$$

$$GJ = 4b\left[D_{66} - \frac{D_{16}^2}{D_{11}}\right] \quad \ldots (2.2.7)$$

$$K_{BT} = 2b\left[D_{26} - \frac{D_{12}D_{16}}{D_{11}}\right] \quad \ldots (2.2.8)$$

2.2.3 Shear Rigidity

The resultant shear strain γ_{yz} is related to the shear force via the shear rigidity kAG:

$$S = kAG\gamma_{yz} \quad \ldots (2.2.9)$$

Also, the shear force per unit width Q_{yz} is related to the shear strain as per equation (2.2.1):

$$Q_{yz} = A_{55}\gamma_{yz} \quad \ldots (2.2.10)$$

Integrating Q_{yz} along the width of the beam, and using equations (2.2.9) and (2.2.10), gives:

$$kAG = bA_{55} \quad \ldots (2.2.11)$$

2.2.4 Bending-Extension Coupling

When the laminate has been delaminated, it creates individual laminates of one or more plies. These sub-laminates may not necessarily be symmetric about their local z=0 axis. This introduces non-zero elements into the [B] matrix, which causes coupling between axial extension and other types of displacement. Extension-bending coupling is the most significant result of a laminate

which is not symmetric about the z=0 axis, and for the static beam analysis for a delaminated beam, shown in section 2.3, an additional bending-axial extension material coupling term is necessary. This correction factor is obtained by inverting the [*ABD*] matrix to give [*abd*], and (Tsai and Hahn (1980)):

$$K_{BA} = \frac{b_{22}}{b} \qquad \ldots (2.2.12)$$

where b is the beam width and K_{BA} is the required bending-axial coupling term.

This can only be considered as a first approximation to the solution of the problem, used to reduce the error caused by assuming a symmetric laminate in equation (2.2.2). For highly asymmetric laminates, or for problems where the exact solution is desired, equations (2.2.2) and (2.2.3) must include axial coupling terms. However, for the purposes of this thesis, equation (2.2.12) was used and was deemed to have an acceptable accuracy. Chapter 4 explains some of the ramifications of this simplification.

2.3 Static Beam Model of a Delaminated Beam Section

As explained in section 2.1, a beam is modelled with a series of connecting elements with known sectional properties, and a dynamic stiffness matrix is obtained for each element. It is therefore necessary to describe a delaminated beam as elements with reduced rigidity terms.

It is assumed for this research that a delamination causes a local reduction in the shear rigidity and torsional rigidity of the beam, and this section describes the analysis used to obtain values for these rigidities. Figure 2.3.1 shows a representation of a beam with a delamination, showing the reduced shear rigidity $(kAG)'$ and torsional rigidity $(GJ)'$ for the delaminated section. It is assumed in this analysis that the bending stiffness EI and the bending-torsional coupling term K_{BT} remains unchanged in the delaminated section.

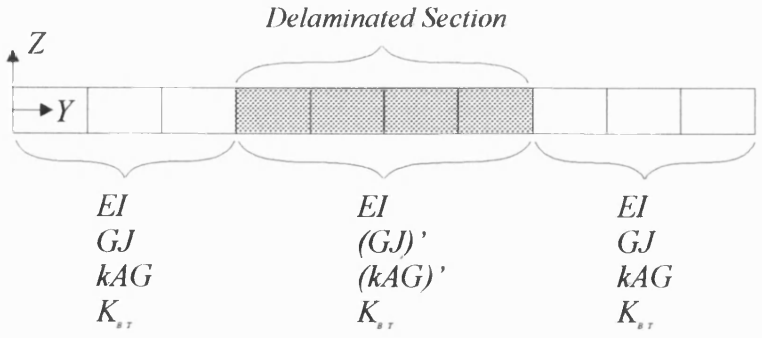

Figure 2.3.1 - Representation of a delaminated beam used in the Dynamic Stiffness Method

2.3.1 Calculation of Equivalent Shear Rigidity

The effect of delamination on shear rigidity is calculated using a static beam model. This models a delamination as two (or more) beams stacked on top of one another, whose end-faces are rigidly connected. This therefore describes a beam with full-length and full-width gaps running parallel to the *Y*-axis. To calculate a value for shear rigidity, a cantilever beam is assumed, because a tip-loaded cantilever beam has constant shear force acting along its length. Some ramifications of approximating the delamination as a tip-loaded cantilever are given in 2.3.1.7.

Figure 2.3.2 shows such a beam with a single delamination at some *z* location, giving two sub-laminates *A* and *B*. Note that because the faces of the sub-laminates are aligned at the root and the tip of the beam, figure 2.3.2 depicts the delamination as not full length, giving rise to end-pieces with length l_{u1} and l_{u2}. However, these lengths are assumed to be zero in the analysis, restraining the end-faces but having effectively zero length.

The result from this global delaminated beam model is then used to describe the local reduction in shear rigidity in the delaminated elements in the DSM.

Since no shear forces can be carried across a delamination, the bending moments and shear forces acting along the beam are re-distributed within the sub-laminates. These re-distributed bending moments cause a change in the deflected shape when compared to the undelaminated beam. The difference between the deflection of the ends of the delaminated and undelaminated beams is assumed to be represented as a reduction in shear rigidity.

For clarity, the analysis is carried out for one delamination in this section, but the full analysis for multiple delaminations is given in Appendix A.

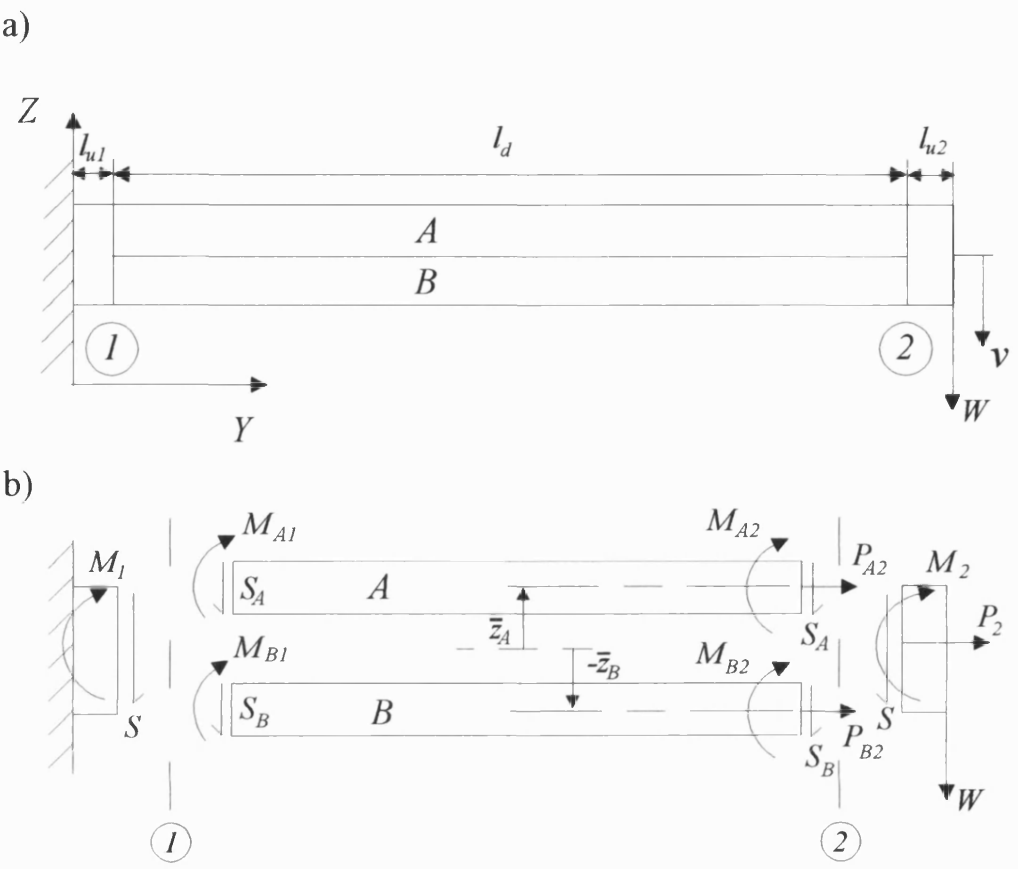

Figure 2.3.2 - a) Delaminated beam section of length l_d. Note that positive force W gives positive deflection v

b) Free body diagram of delaminated section showing the forces and moments acting upon each sub-laminate

The delaminated section of the beam is modelled as a cantilever with a tip load W, see figure 2.3.2. Such a beam has constant shear force (where $S=W$), and linear bending moment distribution along its length, i.e:

$$M = M_1 - Sy \qquad \ldots (2.3.1)$$

where M is the bending moment at a point y along the Y-axis, S is the shear force, and M_1 is the bending moment at the root of the beam.

2.3.1.1 Equilibrium

From figure 2.3.2, resolving horizontally at point 2:

$$P_{A2} + P_{B2} = P_2$$

where P are axial forces acting parallel to the neutral axis of the laminates. If P_2=0 then:

$$P_{A2} = -P_{B2} \qquad \ldots (2.3.2)$$

Taking moments about the neutral axis of the undelaminated laminate for points 1 and 2, and using equation (2.3.2), gives:

$$\begin{aligned} M_{A1} + M_{B1} + P_{A2}\left(\bar{z}_A - \bar{z}_B\right) &= M_1 \qquad \ldots (2.3.3) \\ M_{A2} + M_{B2} + P_{A2}\left(\bar{z}_A - \bar{z}_B\right) &= M_2 \end{aligned}$$

The variables $\bar{z}$ refer to the distance from the neutral axis of the sub-laminates to the neutral axis of the overall laminate. Using equation (2.3.1), the previous expression for sub-laminate 2 gives:

$$M_{A1} - S_A l_d + M_{B1} - S_B l_d + P_{A2}\left(\bar{z}_A - \bar{z}_B\right) = M_1 - S l_d \qquad \ldots (2.3.4)$$

where l_d is the length of the delaminated cantilever.

2.3.1.2 Deflection and Gradient Compatibility

Using simple bending theory, the curvature of a beam with axial-bending coupling is:

$$v'' = \frac{-M_1 + Sy}{EI} + K_{BA} P$$

where the primes signify differentiation with respect to y. Therefore:

$$v' = -\frac{M_1 y}{EI} + \frac{Sy^2}{2EI} + K_{BA}Py + C_1$$

$$v = -\frac{M_1 y^2}{2EI} + \frac{Sy^3}{6EI} + \frac{K_{BA}Py^2}{2} + C_1 y + C_2$$

where the constants C_1 and C_2 can be solved knowing the boundary conditions of the beam. For a cantilever beam, when $y = 0$, $v = 0$ and $v' = 0$. Therefore $C_1 = 0$ and $C_2 = 0$. Also, for the undelaminated beam, the resultant axial force is zero, and in any case, to apply to the restrictions of the DSM the laminate must be symmetric and hence $K_{BA}=0$. Therefore, the axial force term can be neglected. When $y = l_d$, and assuming that both l_{u1} and l_{u2} approach zero:

$$v_{y=l_d} = -\frac{M_1 l_d^2}{2EI} + \frac{Sl_d^3}{6EI} \qquad \ldots (2.3.5)$$

The deflections and gradients of sub-laminates A and B can be similarly calculated, but the axial-bending terms cannot be neglected:

$$v'_{A,y=l_d} = -\frac{M_{A1} l_d}{(EI)_A} + \frac{S_A l_d^2}{2(EI)_A} + K_{BA\,A} P_{A2} l_d \qquad \ldots (2.3.6)$$

$$v_{A,y=l_d} = -\frac{M_{A1} l_d^2}{2(EI)_A} + \frac{S_A l_d^3}{6(EI)_A} + \frac{K_{BA\,A} P_{A2} l_d^2}{2} \qquad \ldots (2.3.7)$$

$$v'_{B,y=l_d} = -\frac{M_{B1} l_d}{(EI)_B} + \frac{S_B l_d^2}{2(EI)_B} - K_{BA\,B} P_{A2} l_d \qquad \ldots (2.3.8)$$

$$v_{B,y=l_d} = -\frac{M_{B1} l_d^2}{2(EI)_B} + \frac{S_B l_d^3}{6(EI)_B} - \frac{K_{BA\,B} P_{A2} l_d^2}{2} \qquad \ldots (2.3.9)$$

Because the sub-laminates A and B are connected at their ends, the end deflection and gradients are equal. Therefore, relationships between M_{A1} and M_{B1}, and S_A and S_B can be determined. From equations (2.3.6) and (2.3.8):

$$-\frac{M_{A1}}{(EI)_A} + \frac{S_A l_d}{2(EI)_A} + \left(K_{BA\,A} + K_{BA\,B}\right) P_{A2} = -\frac{M_{B1}}{(EI)_B} + \frac{S_B l_d}{2(EI)_B} \qquad \ldots (2.3.10)$$

And from (2.3.7) and (2.3.9):

$$-\frac{M_{A1}}{(EI)_A}+\frac{S_A l_d}{3(EI)_A}+\left(K_{BA\,A}+K_{BA\,B}\right)P_{A2}=-\frac{M_{B1}}{(EI)_B}+\frac{S_B l_d}{3(EI)_B} \qquad \ldots (2.3.11)$$

Therefore, from equations (2.3.10) and (2.3.11):

$$M_{A1}=(EI)_A\left(\frac{M_{B1}}{(EI)_B}+\left(K_{BA\,A}+K_{BA\,B}\right)P_{A2}\right) \qquad \ldots (2.3.12)$$

$$S_A=\frac{(EI)_A}{(EI)_B}S_B \qquad \ldots (2.3.13)$$

Using equations (2.3.13) in (2.3.3) and (2.3.4), and solving, gives:

$$S_A=S\left(1+\frac{(EI)_B}{(EI)_A}\right)^{-1} \qquad \ldots (2.3.14)$$

2.3.1.3 Sub-Laminate End Face Compatibility

For the ends of the sub-laminates to be connected to the undelaminated section, or the end of the beam, the end faces must be aligned. The distance each sub-laminate must strain Δ, and therefore the axial force needed to strain each sub-laminate P, is dependent upon the gradient at the end, and the distance between the neutral axes of each sub-laminate $\bar{z}_A-\bar{z}_B$. With reference to figure 2.3.3:

$$\tan\eta\approx\eta=\frac{-\delta z}{\delta y}=-v'$$

$$\left(\bar{z}_A-\bar{z}_B\right)\sin(-\eta)\approx-\left(\bar{z}_A-\bar{z}_B\right)\eta=\Delta$$

$$\Rightarrow\Delta=-\left(\bar{z}_A-\bar{z}_B\right)v' \qquad \ldots (2.3.15)$$

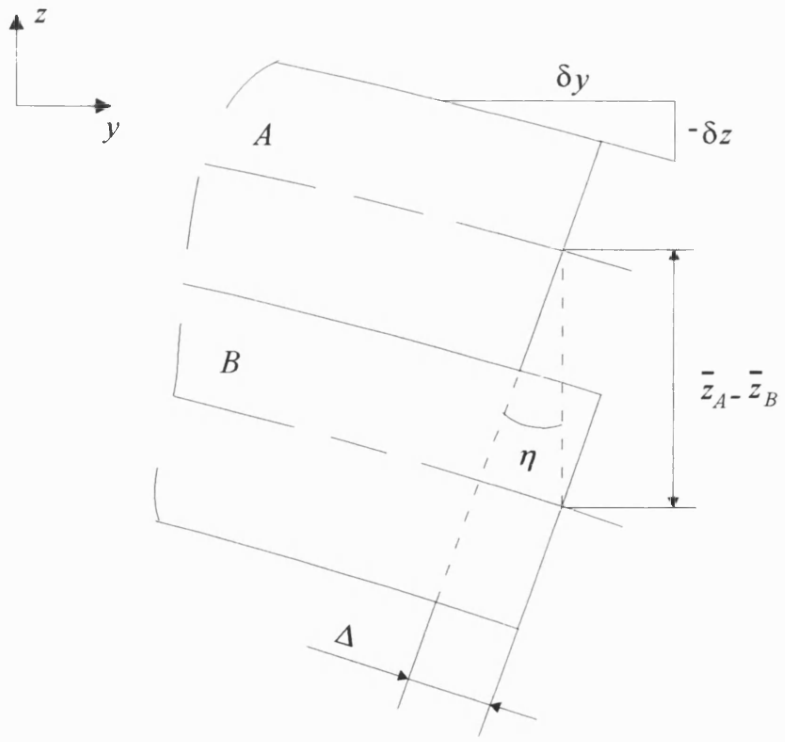

Figure 2.3.3 - End faces of sub-laminates A and B, showing difference in lengths due to gradient

Also, with reference to figure 2.3.4:

$$\Delta = u_A - u_B = \frac{P_{A2} l_d}{(EA)_A} - \frac{P_{B2} l_d}{(EA)_B} \qquad \ldots (2.3.16)$$

where EA denotes the axial stiffness of each sub-laminate. Therefore, from equations (2.3.15), (2.3.16) and (2.3.6):

$$\frac{P_{A2} l_d}{(EA)_A} - \frac{P_{B2} l_d}{(EA)_B} = -\left(\bar{z}_A - \bar{z}_B\right)\left[-\frac{M_{A1} l_d}{(EI)_A} + \frac{S_A l_d^2}{2(EI)_A} + K_{BA} P_{A2} l_d \right]$$

$$\Rightarrow P_{A2} = \frac{\frac{\left(\bar{z}_A - \bar{z}_B\right)}{(EI)_A}\left(M_{A1} - \frac{S_A l_d}{2} \right)}{\frac{1}{(EA)_A} + \frac{1}{(EA)_B} + \left(\bar{z}_A - \bar{z}_B\right) K_{BA\,A}} \qquad \ldots (2.3.17)$$

And, using equations (2.3.17), (2.3.14), (2.3.12) and (2.3.3), the bending moment acting on each sub-laminate can be determined. For sub-laminate A, the bending moment is:

$$M_{A1} = \frac{M_1 + \frac{Sl_d}{2}\frac{\bar{d}}{\bar{B}}\left[\frac{\bar{d} - \overline{BA}(EI)_B}{\bar{A} + \bar{d}K_{BA}}\right]}{1 + \frac{(EI)_B}{(EI)_A} + \frac{\bar{d}}{(EI)_A}\left[\frac{\bar{d} - \overline{BA}(EI)_B}{\bar{A} + \bar{d}K_{BA}}\right]} \quad \ldots (2.3.18)$$

where:

$$\overline{BA} = K_{BA\,A} + K_{BA\,B} \qquad \bar{A} = \frac{1}{(EA)_A} + \frac{1}{(EA)_B}$$

$$\bar{B} = (EI)_A + (EI)_B \qquad \bar{d} = \bar{z}_A - \bar{z}_B$$

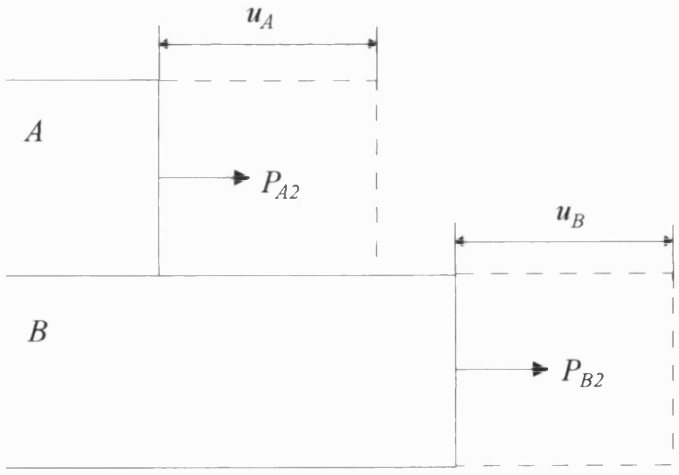

Figure 2.3.4 - Strain necessary to align faces of sub-laminates A and B

2.3.1.4 Delaminated Beam Maximum Deflection

Once the bending moments and shear forces acting on the sub-laminates are found, the end-deflection of the sub-laminates can be calculated. From equations (2.3.7), (2.3.14), (2.3.17) and (2.3.18), the deflection at the end of sub-laminate A can be found:

$$\delta_{delam} = -\frac{M_1 l_d^2}{2}\left[\frac{\overline{A}}{\left(\overline{A}+\overline{d}K_{BA\,A}\right)\overline{B}+\overline{d}\left(\overline{d}-\overline{BA}EI_B\right)}\right]$$
$$+\frac{Sl_d^3}{6}\left[\frac{\left(2-\overline{d}K_{BA\,A}\right)\left(\overline{A}-dK_{BA\,A}\right)^2-\overline{Ad}\left(\overline{d}-\overline{BA}EI_B\right)}{2\overline{B}^2\left(\overline{A}+\overline{d}K_{BA\,A}\right)^2+2\overline{dB}\left(\overline{d}-\overline{BA}EI_B\right)\left(\overline{A}+\overline{d}K_{BA\,A}\right)}\right]$$

... (2.3.19)

where the constants are defined in equation (2.3.18).

2.3.1.5 Deflection due to Shear

The value for shear rigidity for the delaminated beam is calculated from the difference between the end-deflection of the delaminated beam and the end-deflection of the equivalent undelaminated beam. As the delamination moves to the top or bottom surface of the laminate (so that the thickness of one sub-laminate tends to zero), the deflection of the delaminated beam found from (2.3.19) becomes identical to the deflection of the equivalent undelaminated beam, which produces an infinite value for effective shear rigidity of the delaminated beam. The difference in deflection is due to the deflection of the undelaminated beam due to shear force, which when included gives a non-infinite value for effective shear rigidity. The deflection due to shear is calculated using strain energy methods. This method can be found in many structural mechanics textbooks, such as Ryder (1969), but a brief summary is included here for completeness.

The strain energy due to shear U_s is:

$$U_s = \frac{1}{2G}\iint \tau^2 dA.dy \qquad \text{... (2.3.20)}$$

where G is the shear stiffness, τ is the shear stress, and dA and dy are elements of area and length, respectively. It is assumed that the shear stress distribution is parabolic (which, for wide thin beams and ones with varying modulus of elasticity is a simplification of reality (Zaslavsky (1980)):

$$\tau = \frac{4S}{kbd^3}\left[\left(\frac{d}{2}\right)^2 - z^2\right]$$

where k is the shear correction factor (also called the shape factor) for the cross-section, and is the ratio of average to maximum shear stress. For a rectangular cross-section k is 2/3. Therefore equation (2.3.20) becomes:

$$U_s = \frac{1}{2G}\int_0^{l_d}\left[\int_{-d/2}^{d/2}\left(\frac{4S}{kbd^3}\left[\left(\frac{d}{2}\right)^2 - z^2\right]\right)bdz\right]dy$$

And, integrating between the limits:

$$U_s = \frac{4}{15}\frac{S^2 l_d}{k^2 bdG} \qquad \ldots (2.3.21)$$

For a cantilever beam loaded at the tip with force W, the shear strain energy equated to the work done by the shear force:

$$U_s = \frac{W\delta_s}{2} = \frac{S\delta_s}{2} \qquad \ldots (2.3.22)$$

where δ_s is the end-deflection due to shear. Therefore, from equations (2.3.21) and (2.3.22), the deflection due to shear can be written as:

$$\delta_s = \frac{8}{15}\frac{Sl_d}{k^2 bhG} = \frac{8}{15}\frac{Sl_d}{k^2 AG} \qquad \ldots (2.3.23)$$

2.3.1.6 Equivalent Shear Rigidity

If equation (2.3.19) is compared to (2.3.5) it is possible to see that the deflection of the delaminated beam is greater than if it were not delaminated. It is assumed that this difference can be represented as a reduction in shear rigidity of the undelaminated beam. With reference to figure 2.3.5, the difference in deflection is:

$$\delta_{s_{delam}} = \delta_{delam} - \delta_{m_{no-delam}} + \delta_{s_{no-delam}}$$

where the values of beam end-deflection for the different load cases can be obtained from equations (2.3.19), (2.3.23) and (2.3.5). This, via equation (2.3.23), gives a value for the equivalent shear rigidity for the delaminated section:

$$(AG)' = \frac{8}{15} \frac{SI_d}{k^2 \delta_{S_{delam}}} \qquad \ldots (2.3.24)$$

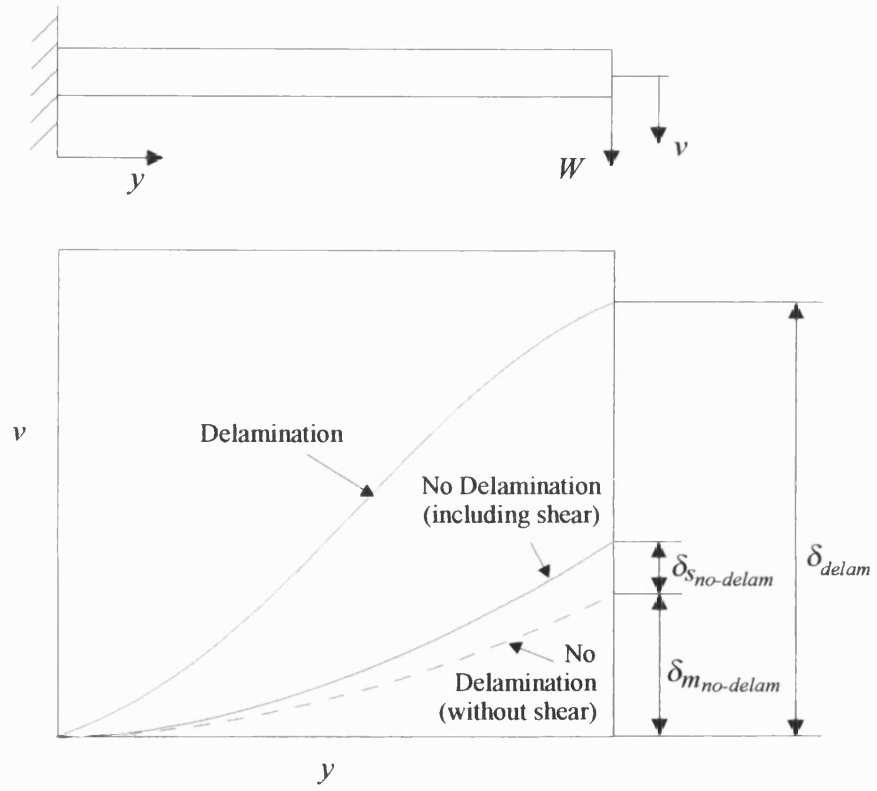

Figure 2.3.5 - Comparison of delaminated and undelaminated deflected shapes

2.3.1.7 Limitations of the Reduced Shear Rigidity Model

The static beam model described above uses a tip-loaded cantilever beam, which has constant shear force along its length. This is therefore assuming that for any section along a bending mode, the shear force distribution can be approximated as being constant. Figure 2.3.6 shows the average shear force distribution for an arbitrary bending mode. At position A, a delamination with a length that is one-eighth of the wavelength is located at the position of maximum shear force. Here, the constant shear force (shown shaded) approximates well the actual shear force. At

position B, the average shear force is zero, and no effect of delamination is seen, which is again a satisfactory approximation as long as the delamination remains small. At position C, the constant shear force approximation is less accurate, as the average shear force varies from a maximum to zero along the length of the delamination. This situation would best be approximated as a cantilever with a different loading, for example one with a constant distributed load along its length. If the shear force distribution at this point varied linearly with delamination length from S_{max} to 0, the tip-loaded cantilever would have a constant shear force distribution of $S_{max}/2$, giving a deflection of:

$$v_{y=l} = \frac{S_{\max} l^3}{6EI}$$

The equivalent deflection of a cantilever with a constant distributed load of S_{max}/l is (Gere and Timoshenko (1984)):

$$v_{y=l} = \frac{S_{\max} l^3}{8EI}$$

Showing that at this position, the constant shear force approximation is more severe than reality, and that the model will overestimate the reduction in shear rigidity. However, at the start of the same half-wavelength, the shear force distribution could be approximated more accurately as a cantilever beam with linear shear force varying from zero at the root to S_{max} at the tip. In this case the beam deflection is slightly greater than for the constant shear force approximation. This means that the constant shear force assumption results in an underestimation of the drop in shear rigidity. Because there are regions where the shear force distribution causes more deflection, and likewise there are regions where the deflection is reduced, a constant shear force approximation is therefore seen as the best compromise between the possible models that could be used, as long as the delamination remains small.

As the delamination size increases, however (shown for example in position D), the constant shear force approximation becomes more inaccurate, which limits the method to small delamination lengths compared to the wavelengths of the modes.

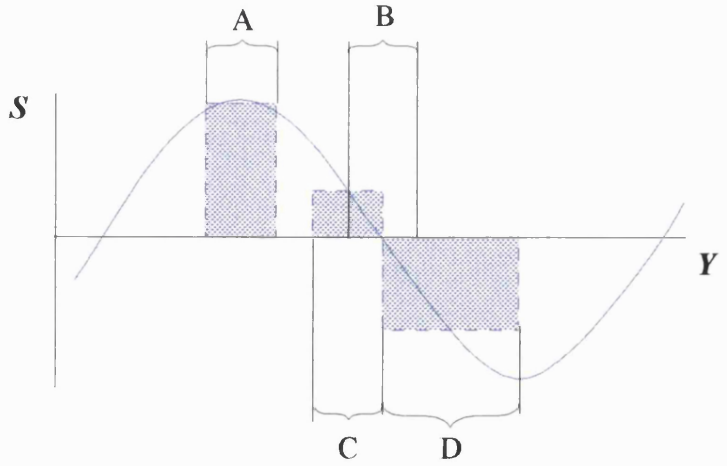

Figure 2.3.6 – Average shear force distribution for one wavelength of an arbitrary mode and the constant assumption made in the static beam model

However, there are other reasons that limit the application of the DSM as the delamination size increases. This model does not allow for contact between the sub-laminates as they vibrate. Modelling contact between the sub-laminates was shown by Mujumdar and Suryanarayan (1988) to relatively increase the natural frequencies. This becomes more apparent as the length of the delamination increases. Furthermore, for sub-laminates with high slenderness ratios (i.e. long delaminations that are close to the top or bottom surfaces of the laminate), local opening modes are seen, and the effects of non-linearity are more apparent (Lestari *et al.* (2000)).

2.3.2 Calculation of Equivalent Torsional Rigidity

This analysis is based on the torsion of composite cylinders. As such, the results from this analysis can only be considered as a very rough first approximation. The reasons for this, and some of the ramifications of the simplification, are given in section 2.3.2.1. For a discussion of the formulation, see Gere and Timoshenko (1984). As in the previous section, the analysis in this section will be carried out for one delamination. The result for multiple delaminations is given in Appendix B.

Consider the delaminated beam in figure 2.3.7. Taking equilibrium at the end of the delaminated section:

$$T = T_A + T_B \qquad \text{... (2.3.25)}$$

It is assumed that, since the delamination is fixed to the beam at its ends, the twist of each sub-laminate at their ends is equal. Hence:

$$\psi = \psi_A = \psi_B \qquad \ldots (2.3.26)$$

The angle of twist is related to the length and torsional rigidity of the section by:

$$\psi = \frac{Tl_d}{GJ}; \psi_A = \frac{T_A l_d}{(GJ)_A}; \psi_B = \frac{T_B l_d}{(GJ)_B} \qquad \ldots (2.3.27)$$

where the torsional rigidity for each sub-laminate is found by the expressions in section 2.2. Therefore using equations (2.3.25), (2.3.26) and (2.3.27), the torque acting on each sub-laminate can be found:

$$T_A = T\left(\frac{(GJ)_A}{(GJ)_A + (GJ)_B}\right) \qquad \ldots (2.3.28)$$

$$T_B = T\left(\frac{(GJ)_B}{(GJ)_A + (GJ)_B}\right)$$

And, equations (2.3.26) and (2.3.27) give:

$$\psi = \frac{Tl_d}{(GJ)_A + (GJ)_B}$$

Therefore, by inspection, the equivalent torsional rigidity for the delaminated section is:

$$(GJ)' = (GJ)_A + (GJ)_B \qquad \ldots (2.3.29)$$

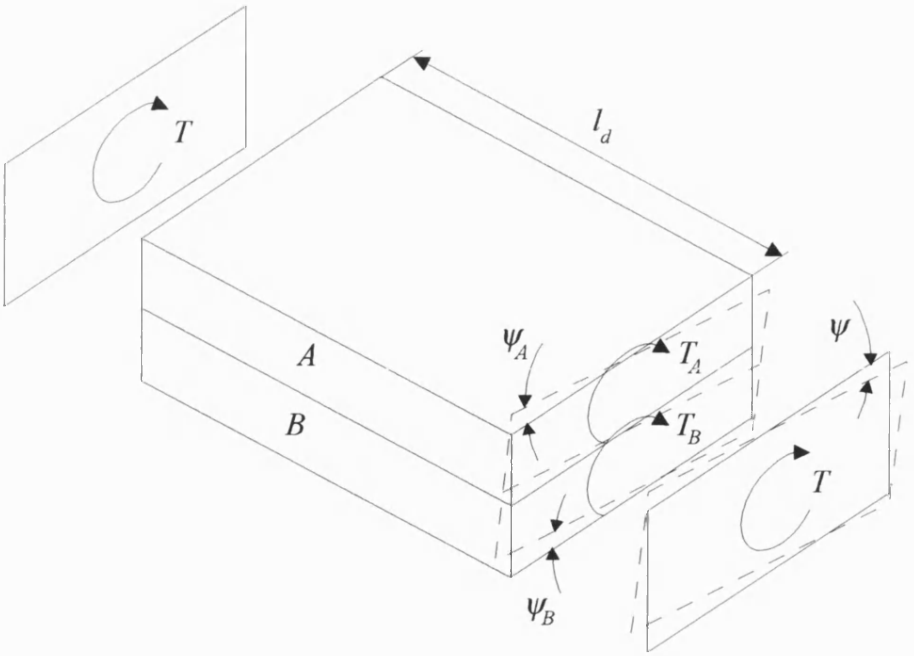

Figure 2.3.7 - Delaminated beam section showing the torque acting on each sub-laminate

2.3.2.1 Limitations of the Reduced Torsional Rigidity Model

At the beginning of section 2.3.2 it was mentioned that the model used to derive the reduced torsional rigidity of a delaminated section could only be used as a first approximation to the problem. Indeed, results using this model were later seen to be very inaccurate when compared to the FE model and experiment.

One inaccuracy of the model might arise from the fact that when the sub-laminates twist under an applied torque, the end-face compatibility condition, which was previously applied to the bending displacement to find the shear rigidity, is violated.

Figure 2.3.8 explains this more clearly. Here, the end of an isotropic beam with a centreline delamination and an applied torque, is shown. When a torque is applied to make the beam twist with an angle Ψ, the sides of the sub-laminates at their ends are no longer aligned. The distance between the sides of the sub-laminates, Δ^t (where the superscript t is used to differentiate it from the previously defined Δ, and is that due to twist), depends on the angle of twist and the thickness of the sub-laminates $d/2$.

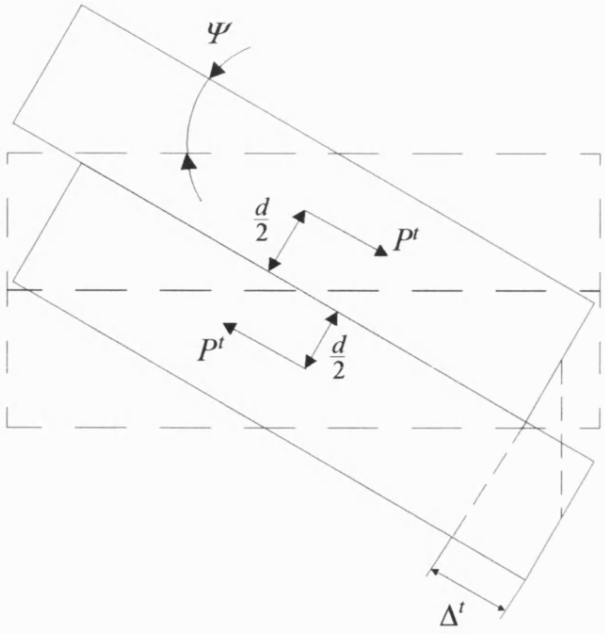

Figure 2.3.8 – Sub-laminate end faces showing end-face incompatibility due to twist

Imposing the condition that the sides of the sub-laminates must be aligned, means that a set of forces (P^t) must be present, the magnitude of which depends upon the shear rigidity and cross-sectional area of the sub-laminates. These produce a couple that acts in the same direction as the torque required to twist the sub-laminates. For equilibrium at the end of the beam therefore, the applied torque necessary to provide the same twist as previously, being the sum of the torque necessary to twist the laminates and that necessary to apply the couple, is greater.

Therefore, the stiffness of the delaminated section is in reality greater than the model outlined in section 2.3.2 suggests. The static model used in the thesis must therefore be taken as a lower bound on the torsional rigidity of the delaminated section, and it is suggested that work be carried out to include the end-face compatibility when deriving the torsional rigidity in the future. The ramifications of using this 'lower-bound' on the torsional stiffness are highlighted in Chapters 4 and 6.

2.4 Finite Element Analysis

Finite Element Analysis (FEA) was performed in order to assess the accuracy of the static model, and to compare the frequencies obtained via the Dynamic Stiffness Method. The FEA was carried out using the commercially available software package ANSYS (Swanson Analysis Systems (1992)). Two models were used during the research, a model based on a 2-dimensional plane

element using isotropic material, and one based on a 3-dimensional layered structural solid. Each model is described separately.

2.4.1 2-Dimensional Finite Element Model

The 2-dimensional model was used to verify the static beam model and to compare the frequencies provided by the Dynamic Stiffness Method. The ANSYS element *PLANE42* was used. This is a 2-D element, used in its plane stress form, which has large deflection and large strain capabilities. Each node of the element has two degrees of freedom; translation in the x and y directions. A representation of the beam model is shown in figure 2.4.1.

The delamination was modelled as a gap between the layers. Using a static cantilever beam model with dimensions of 1m×0.1m×0.01m, this gap was varied between 0.001m and 0.00001m, for a centreline delamination at the centre of the beam length. For each value of gap thickness, the end deflection of an example cantilever beam was calculated using the finite element model. This result was then extrapolated to a 'gap' of zero thickness. It was seen that the minimum gap allowed by ANSYS (that of 0.00001m) produced a difference in deflection of 0.2% or less when compared to the extrapolated zero thickness 'gap', and therefore this gap was used throughout the analysis. Table 2.4.1 shows the results of this analysis. No allowance for contact between the top and bottom layers in the delaminated region was made in this model.

The beam had 100 elements along its length, and the length of the delaminated (l_d) area could be varied to simulate different size delaminations. As the size and position of the delamination was varied, the sections were divided so that the two undelaminated sections and the one delaminated sections had as equal element size as possible. The beam also had as many elements through the thickness as possible whilst still ensuring each element had an acceptable aspect ratio and that the problem was within the capacity of the computer. This usually meant from 6 to 10 through thickness elements were used. The cantilever boundary conditions were ensured by allowing no displacements of the nodes at the root of the beam.

2.4.2 3-Dimensional Finite Element Model

The 3-D model is used later to verify the static beam model and to compare the frequencies provided by the Dynamic Stiffness Method. Unlike the 2-D model, 3-D model allowed layered material properties to be input in order to model a composite laminate. The ANSYS element

SOLID46 was used. Each node of the element has three degrees of freedom; translation in the x, y and z directions. The beam model is shown in figure 2.4.2.

The beam had 100 elements along its length, 6 or 8 elements along its width, and as many elements through its thickness as possible to ensure accuracy. The number of elements through the thickness of the beam was restricted by the necessity of each element having an allowable aspect ratio, and by the storage capacity of the computer. Usually this was 6 or 8 elements. As for the 2-D model, the cantilever boundary conditions were ensured by allowing no displacements of the nodes at the root of the beam, and for the static deflection analyses, the tip load was divided equally between the z=0 nodes at the tip. It was assumed that, as for the 2-D FE model, a gap of 0.00001m between the layers adequately models a delamination.

A more detailed description of the size of the beams (and therefore the element size), for both the 2-dimensional and 3-dimensional models, and the materials properties used, is given in Chapter 4.

Size of Delamination [% Beam Length]	**Gap Size [m]**	**End Deflection of Beam [m]**	**% Difference from Extrapolated 0m Gap**
0	-	0.10949	-
50	0.001	0.10835	9.7
	0.0001	0.11717	2.4
	0.00001	0.11972	0.2
	Extrapolated to 0.0	0.12000	-
100	0.001	0.17332	10.4
	0.0001	0.19043	1.0
	0.00001	0.19214	0.1
	Extrapolated to 0.0	0.19233	-

Table 2.4.1 - End-Deflection of a 1m×0.1m×0.01m delaminated cantilever aluminium beam with a 20N tip load (Material Properties Given in Section 4.1.1)

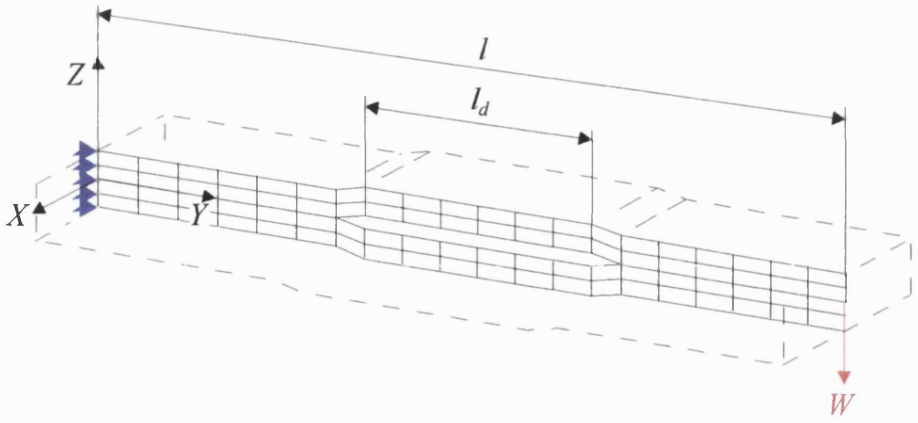

Figure 2.4.1 - Finite Element model using 2-D (*PLANE42)* elements

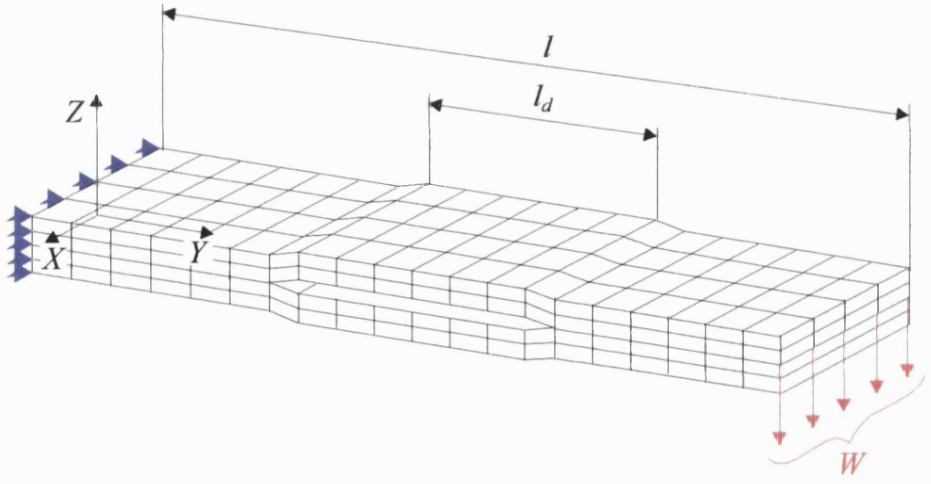

Figure 2.4.2 - Finite Element model using 3-D (*SOLID46)* elements

3. Optimisation and the Damage Detection Methodology

The procedure for detecting delaminations in composite beams using experimental vibrational behaviour can be divided into two processes; *structure characterisation* and *damage detection*. Characterisation of the structure is a model-updating method, which involves updating the material properties and boundary conditions of the beam using experimentally obtained vibrational behaviour of the undamaged beam. Once this has been carried out, the experimentally obtained vibrational behaviour of the damaged beam is used to locate the delaminations. Both of these processes involve using an optimisation method, where the dynamic response of the structure is compared to an estimate produced by the DSM, and the difference minimised. In this chapter, the optimisation methods used in these processes are described, and the methods used to implement the DSM into the optimisers are outlined.

3.1 Gradient-Based Optimisation

For this research, the gradient-based, numerical optimisation method the Modified Method of Feasible Directions (MMFD), contained within the program Design Optimisation Tools (DOT) was used. This section gives an overview of the method, because many of the conclusions made assume an understanding of the optimisation process involved. However, a more detailed description can be obtained in Vanderplaats Research & Development, Inc. (1995).

The optimisation problem is stated formally as:

Minimise the objective function:

$$O(X) \qquad \ldots (3.1.1)$$

Subject to the inequality constraints:

$$G_j(X) \le 0 \qquad j = 1 \ldots n_{con} \qquad \ldots (3.1.2)$$

and the side constraints:

$$X_i^L \le X_i \le X_i^U \qquad i = 1 \ldots n_{dv} \qquad \ldots (3.1.3)$$

The objective function, $O(X)$, is a measure of fitness of the design. This function is minimised by the MMFD, so that for an ideal solution $O(X)=0$. In both the characterisation and damage

detection stages, $O(X)$ quantifies the difference between experimentally derived data and that produced by the DSM.

X refers to the n_{dv} variables that can be changed by the optimiser to produce a solution, known as the design variables. The different combinations of values that the design variables can take is known as the design space. In the characterisation stage the design variables are the material properties and boundary conditions, and in the damage detection stage the design variables are the number, size and location of the delaminations.

The n_{con} constraints $G(X)$ are used to ensure that the design remains in the region desired by the user. In this research, this is achieved by the use of explicit inequality constraints. The constraints are explicit because they are direct functions of the design variables, and they are inequality constraints because they are restricted to be greater or less than some value. If one or more constraints are violated, the design is said to be unfeasible. Otherwise it is a feasible design. Usually, inequality constraints are normalised.

The side constraints define the upper X_i^U and lower X_i^L bounds that each design variable may take. In practice, the numerical conditioning of the optimisation is improved if the design variables are normalised with respect to their upper bound, so that equation (3.1.3) becomes:

$$0 \leq X_i \leq 1 \qquad i = 1 \ldots n_{dv} \qquad \ldots (3.1.4)$$

The first stage of the MMFD process, shown as a flow chart in figure 3.1.1, is to calculate the objective function and constraints for iteration q. This is specific to the problem, as the objective function and the number and type of constraints depends upon the structure, and is discussed in sections 3.3.1 and 3.3.2.

3.1.1 Design variable sensitivities

By using a finite difference method, the rates of change of the objective function and constraint values with design variables, depicted by the gradient operator ∇, are determined:

$$\nabla_i O(X) = \begin{bmatrix} \dfrac{O(X+\delta X_1) - O(X)}{\delta X_1} \\ \cdots \\ \dfrac{O(X+\delta X_{n_{dv}}) - O(X)}{\delta X_{n_{dv}}} \end{bmatrix} \qquad \nabla_i G_j(X) = \begin{bmatrix} \dfrac{G_j(X+\delta X_1) - G_j(X)}{\delta X_1} \\ \cdots \\ \dfrac{G_j(X+\delta X_{n_{dv}}) - G_j(X)}{\delta X_{n_{dv}}} \end{bmatrix}$$

$$i = 1 \ldots n_{dv} \qquad j = 1 \ldots n_{con} \qquad \ldots (3.1.4)$$

Here the step size δ is initially specified by the user, and subsequently after the first iteration is calculated by **DOT**.

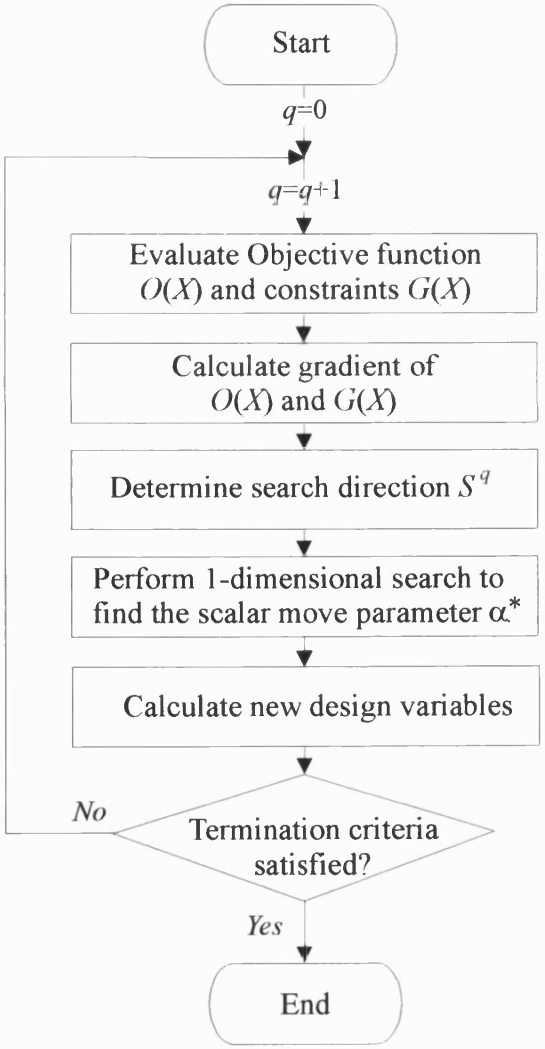

Figure 3.1.1 - Structural optimisation using the modified method of feasible directions

3.1.2 Finding the search direction

The next stage is to determine the search direction S^q. The method used to achieve this is dependent upon whether or not the constraints are violated.

Figure 3.1.2 shows a 2-dimensional design space with two constraints. According to equation 3.1.2, when a constraint is positive it is unfeasible and therefore violated, and when it is negative it is feasible. However, to ensure robust optimisation, an active region is defined. This is defined as:

$$\begin{aligned} G_i &< -0.03 && \text{Constraint inactive} \\ -0.03 &< G_i < 0.005 && \text{Constraint active} \\ G_i &> 0.005 && \text{Constraint inactive} \\ i &= 1 \ldots n_{con} && \ldots (3.1.5) \end{aligned}$$

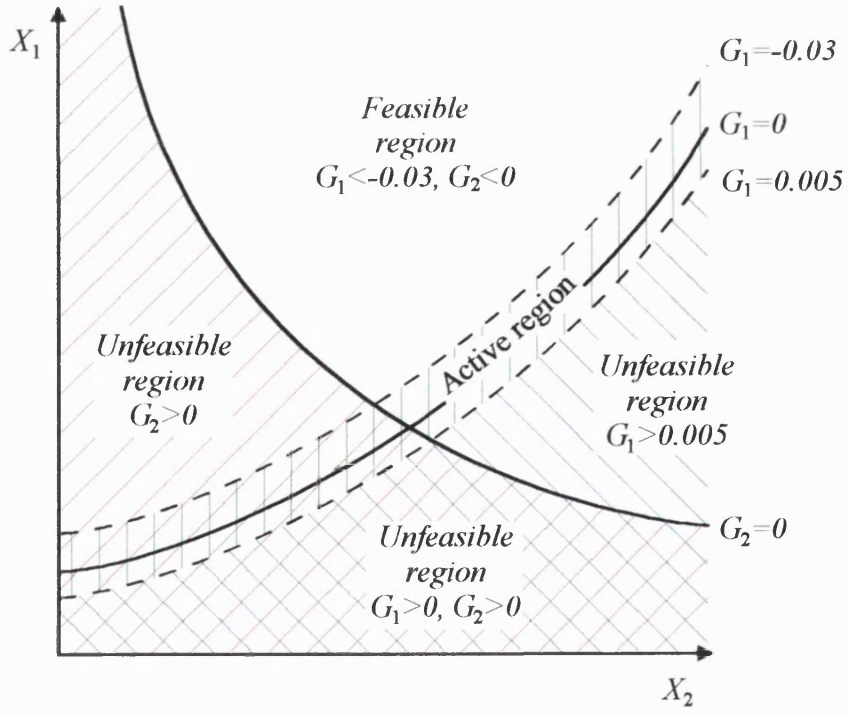

Figure 3.1.2 - 2-Dimensional design space with two constraints showing feasible, unfeasible and active regions (Only the active region for constraint G_1 is shown)

In figure 3.1.2, only the active region for the first constraint is shown.

The mathematical formulation of the search direction is not given here, as it depends on whether the design has no active or violated constraints, active but no violated constraints or one or more violated constraints. The formulation can be found in Vanderplaats Research & Development, Inc., (1995). Suffice it to say that when the design is feasible, the search direction is the path of steepest descent, given by $-\nabla O(X)$, modified so that the search direction for each iteration is slightly less than perpendicular with respect to the search direction of the previous iteration. When one or more constraints are active, the search direction is calculated to be as steep as possible, whilst ensuring that the design remains feasible. When one or more constraints are violated, the search direction is calculated to be towards the feasible region, whilst reducing the objective function if possible.

The search direction calculated in this step is out of necessity based on local information, i.e. the gradients are obtained from information in the local neighbourhood of the point. If the design space is complicated as many real-world problems are, the optimum design may be a local optimum, and the optimum of the whole design space, the global optimum, may not be found.

3.1.3 Finding the scalar move parameter

Once the search direction has been found, it is necessary to determine how far to move in this direction. A one-dimensional search is carried out to find an estimate of the scalar move parameter α^*_{est}. If no constraint is violated, α^*_{est} is the minimum value that moves the objective function by a user-specified amount, perhaps by 10%, whilst ensuring that no constraint becomes violated. If a constraint is violated, α^*_{est} is the largest value that makes all constraints feasible.

An interpolation process is then carried out to find the scalar move parameter α^*, such that the objective function is as small as possible, and the design variables remain within their upper and lower bounds.

Using the search direction and the scalar move parameter, a new set of design variables is calculated, as follows:

$$X^q = X^{q-1} + \alpha * S^q \qquad \ldots (3.1.6)$$

Use of the scalar move parameter and equation (3.1.6) assumes that the design variables can assume an infinite number of values, i.e. the problem is a *continuous* one. Using this method directly for damage detection is therefore not possible, as some of the design variables in the damage detection problem can assume only a finite number of values. This is called a *discrete* problem, and some further analysis must be undertaken if the MMFD is to be used. The steps undertake to remedy this are given in chapter 7.

3.1.4 Terminating the optimisation

The optimisation process outlined above continues, see figure 3.1.1, until one or more of the termination criteria are met. These are:

- The optimisation reaches a maximum number of iterations (usually 100) without any of the other termination criteria being met.
- The optimisation reaches a maximum number of iterations (usually 20) without a feasible solution being found.
- The optimisation has reached the point of diminishing returns. This occurs when the solution is converging asymptotically, and continued iterations are not justified. Stated algebraically, the criteria are:

$$\frac{\left|O(X^q) - O(X^{q-1})\right|}{\left|O(X^{q-1})\right|} \leq 0.001 \qquad \ldots (3.1.7)$$

or:

$$\left|O(X^q) - O(X^{q-1})\right| \leq \max\left\{0.0001, 0.001 \times \left|O(X^0)\right|\right\} \qquad \ldots (3.1.8)$$

- The Kuhn-Tucker criterion is met (Vanderplaats Research & Development, Inc (1995)). Stated simply, this tests to see whether the vector sum of the gradients of the objective function and all active constraints multiplied by a scalar is zero. If the optimisation problem given in (3.1.1) to (3.1.3) is unconstrained (i.e. equation 3.1.2 is removed), the Kuhn-Tucker conditions simply state that the gradient of the objective function must be zero.

In practice, unless problem is ill-conditioned, it is the third of the criteria which is usually met.

3.2 Optimisation via a Genetic Algorithm

In the previous section it was mentioned that gradient-based optimisation via DOT has two inherent problems when applied to detection of delaminations in composite laminates. Firstly, although DOT has processes to minimise this effect, gradient based techniques use the data at a local point, so that the optima they seek are the best in the neighbourhood of the current point. For complex functions the design space may have many troughs, called local optima, and a gradient-based search method may locate a local optimum rather than a global one.

Secondly, the gradient-based method used in DOT is inherently a continuous optimiser, where an infinite number of solutions is assumed to exist. However, this research concerns itself with inter-ply delamination, which, as described in Chapter 1 and seen experimentally in Chapter 6, is a predominant damage mechanism arising from low-velocity impact damage. Therefore only a discrete set of ply locations and number of delaminations is possible, and locating delaminations in composite laminates becomes a discrete problem.

Using a Genetic Algorithm (GA) as the structural optimiser overcomes these problems. A structure is encoded as a binary string, known as the gene, whose individual bits describes properties of the structure, meaning a discrete problem is easily handled. Also, at each iteration a random population of strings is produced, meaning that a GA is a global search routine.

The GA used in this thesis is GENESIS (Grefenstette (1990)), which is a program written in the programming language C, designed to allow a user-defined subroutine to be the evaluation function. A schematic representation of the optimisation process is given in figure 3.2.1.

The first stage in the optimisation process is to initialise the population P(q=0). This involves producing a random selection of structures in the form of binary strings. The size of the population, n_{pop}, is defined by the user.

The next stage is to define the fitness of each structure in the current population. This stage involves converting the binary gene into a physical representation of the damaged beam, including the number, size, and location of the delaminations. Once this is achieved, the value of an objective function is calculated for each structure. This quantifies the difference between the experimental frequencies and mode-shapes and those produced numerically by the DSM. The fitness, F, of the structure, i, is then defined as:

$$F(i) = O_{max} - O(i) \qquad i = 1...n_{pop} \qquad \ldots (3.2.1)$$

Where $O(i)$ is the objective function of the ith member of the current generation, and O_{max} is the maximum value of objective function of all the structures in the preceding generations. The number of generations used to define O_{max} is called the scaling window, and is defined by the user.

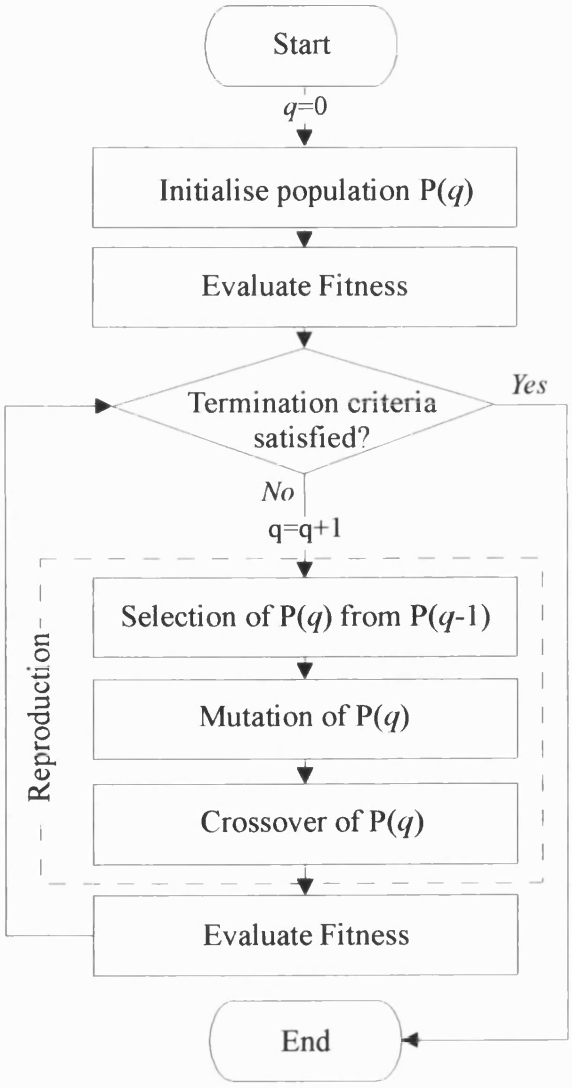

Figure 3.2.1 - Structural optimisation via the GENESIS genetic algorithm routine

The conversion between the binary gene and the representation of the physical structure, and the calculation of the objective function, is problem-specific, and is outlined in section 3.3.3.

Assuming none of the termination criteria have been satisfied at this stage, a new population is selected out of the old population. The probability of one structure being selected in preference to another is dependent upon its relative fitness, so that:

$$p_{selection}(i) = \frac{F(i)}{\sum_{j=1}^{n_{pop}} F(j)} \qquad i = 1 \ldots n_{pop} \qquad \ldots (3.2.2)$$

This is achieved by allocating each structure a portion of a spinning wheel, the proportion of which is equal to $p_{selection}$. The wheel is then spun n_{pop} times, creating a new population P(q) which is randomly shuffled via the spinning wheel process.

Next, the population of structures undergoes mutation, the probability (p_m) of which is defined by the user. Each bit in the binary string is given the chance to mutate, and is assigned a random value of 0 or 1, if it does. It is generally accepted (Goldberg (1989)) that the probability of mutation has a value of 0.001 to 0.01, with higher values giving a more global search to reduce local optimum, but at the expense of efficiency.

The last stage of the reproduction phase is crossover. In this process, the two neighbouring genes in the population, called the parent genes, have a probability of switching parts (or alleles) of the string to create two new offspring genes. This is depicted in figure 3.2.2. Here, each parent gene is treated as a ring, and two crossover points are randomly chosen. The segments are then exchanged to create the offspring genes. The probability (p_c) of crossover occurring is defined by the user, and is generally accepted to be between 0.6 and 0.8.

Parents:	0 1 0 0 ¦ 1 0 1 0 ¦ 0 1 0	1 1 0 1 ¦ 1 1 0 0 ¦ 0 1 1
Offspring:	0 1 0 0 ¦ 1 1 0 0 ¦ 0 1 0	1 1 0 1 ¦ 1 0 1 0 ¦ 0 1 1

Figure 3.2.2 - Crossover of two parent genes to produce two new offspring genes

After crossover has taken place, the population of genes is again evaluated via the objective and fitness functions.

In GENESIS, the optimisation is terminated either after a user-specified number of trials, or when a population is identical to one of its earlier generations. However, when comparing optimisation times with DOT, a similar termination criteria to the MMFD can be used by inspecting the optimiser output to determine at which generation the objective function reached the criteria specified in equations (3.1.7) and (3.1.8).

3.3 Integration of the Dynamic Stiffness Method into the optimisation process

In the preceding sections, the two optimiser methods used in this research were outlined. The following sections describe how the DSM is integrated into the optimisers for both the structural characterisation and the damage detection phases.

3.3.1 Structural Characterisation using DOT

When comparing experimental results with theoretical results for damaged beams, not all the differences can be explained by the damage. Two sources of inaccuracy are: incorrect material properties, and imperfectly stiff boundary conditions. These inaccuracies are catered for in the structural characterisation phase.

In this process, the MMFD is used to adjust the material properties and boundary conditions (by modelling the boundary conditions as springs and adjusting the spring constants), until the frequencies and mode-shapes for the undamaged beam, produced by the DSM, are as close as possible to those measured experimentally.

The objective function, which is similar to that used by others (Ruotolo and Surace (1996)), is defined as:

$$O(X) = \alpha \sum_{i}^{n_f} \left[100 \times \left(\frac{\omega_i^* - \omega_i(X)}{\omega_i^*} \right) \right]^2 + \beta \sum_{i}^{n_f} \sum_{j}^{n_p} \left(\phi_{ij}^* - \phi_{ij}(X) \right)^2 \qquad \ldots (3.3.1)$$

where $\omega_i(X)$ are the n_f natural frequencies calculated using the DSM for a particular set of design variables, and ω_i^* the experimental frequencies. The constants α and β are supplied by the user to ensure a well-conditioned objective function. Also, $\phi_{ij}(X)$ and ϕ_{ij}^* are the equivalent mode-shapes quantified defined by taking values at n_p points along the beam. A different method of defining $\phi_{ij}(X)$ and ϕ_{ij}^* is used, depending upon whether the modes are bending modes or torsion modes.

As described in section 2.1, the DSM produces a mode-shape vector, whose elements are divided by a constant value so that the value for either the maximum bending displacement h, bending rotation θ, or torsional rotation ψ is unity. In this thesis, a mode-shape is defined as a bending mode if, after the displacements have been normalised, the normalised torsional rotation does not exceed 0.6. Similarly, if both the normalised bending rotation and the normalised bending displacement do not exceed 0.6, the mode is defined as a torsion mode.

If the mode is a bending mode, the values of $\phi_{ij}(X)$ and ϕ_{ij}^* in equation (3.3.1) are the normalised vertical displacements at the n_p points along the beam. However, if the mode is a torsional mode, it is necessary to manipulate the experimental data so that equivalent modal vectors are compared. This is because the DSM produces a vector of normalised rotational angles, whereas experimental modal analysis produces vertical nodal displacements. In this procedure, the maximum normalised angle produced by the DSM is assumed to be equal to the angle produced by the experimentally measured normalised maximum vertical displacement. If the maximum angle produced by the DSM is ψ_{max}, the maximum nodal vertical displacement at the edge of the beam is $z_{max\ edge}$, and the corresponding displacement at the centre line is $z_{max\ cl}$, the elements of the experimental mode-shape vector can be found by:

$$\tan\phi_{ij}^* = \frac{z_{edge_{ij}} - z_{cl_{ij}}}{\tan\psi_{\max_i}} \qquad i = 1\ldots n_f,\ j = 1\ldots n_p \qquad \ldots (3.3.2)$$

where z_{edge} and z_{cl} are the experimentally obtained vertical displacements at some distance along the Y-axis.

It is assumed that the material properties supplied initially can be changed by 50% of their original value by the optimiser. The design variables can vary from 0 to 1, and therefore the first

nine design variables give the updated nine mutually independent material properties of a ply as follows:

$$E_1^q = [1 + 0.5(2X_1 - 1)]E_1 \quad \ldots (3.3.3)$$

$$E_2^q = [1 + 0.5(2X_2 - 1)]E_2 \quad \ldots (3.3.4)$$

$$E_3^q = [1 + 0.5(2X_3 - 1)]E_3 \quad \ldots (3.3.5)$$

$$\nu_{12}^q = [1 + 0.5(2X_4 - 1)]\nu_{12} \quad \ldots (3.3.6)$$

$$\nu_{23}^q = [1 + 0.5(2X_5 - 1)]\nu_{23} \quad \ldots (3.3.7)$$

$$\nu_{31}^q = [1 + 0.5(2X_6 - 1)]\nu_{31} \quad \ldots (3.3.8)$$

$$G_{12}^q = [1 + 0.5(2X_7 - 1)]G_{12} \quad \ldots (3.3.9)$$

$$G_{13}^q = [1 + 0.5(2X_8 - 1)]G_{13} \quad \ldots (3.3.10)$$

$$G_{23}^q = [1 + 0.5(2X_9 - 1)]G_{23} \quad \ldots (3.3.11)$$

where the superscript q refers to the updated value for iteration q.

The boundary conditions at the root of the cantilever beam are modelled as three springs, which can move in the h, θ or ψ directions. The spring constants are given the values k_h, k_θ and k_ψ, respectively.

By varying the values of spring constant and noting the change in frequency, shown in figure 3.3.1, it was determined that a spring stiffnesses of 1×10^9 N/m, 1×10^9 Nm/rad, and 1×10^9 Nm/rad could be interpreted as, for all intents and purposes, infinitely stiff. Therefore, each stiffness constant was allowed to vary from a value of 1 to 1×10^9, using a logarithmic scale, as follows:

$$k_h^q = 10^{9X_{10}} \quad \ldots (3.3.12)$$

$$k_\theta^q = 10^{9X_{11}} \quad \ldots (3.3.13)$$

$$k_\psi^q = 10^{9X_{12}} \quad \ldots (3.3.14)$$

In all tests, the problem was unconstrained, so that equation (3.1.2) could be removed from the problem.

Tests were carried out with and without mode-shapes (by setting β to 0), and are shown in Chapter 7.

When researchers use structural characterisation to determine the material properties of a material (for example Araujó *et al.* (1995)), free-free boundary conditions are usually used. This eliminates the significant errors that can arise from imperfect boundary conditions. However, the characterisation in this research is used to minimise the error in the structural model as well as to model imperfect boundary conditions. The material properties obtained by this method should not be taken as absolute material parameters, but are simply the material properties that give the best agreement between the model and experimental results.

a)

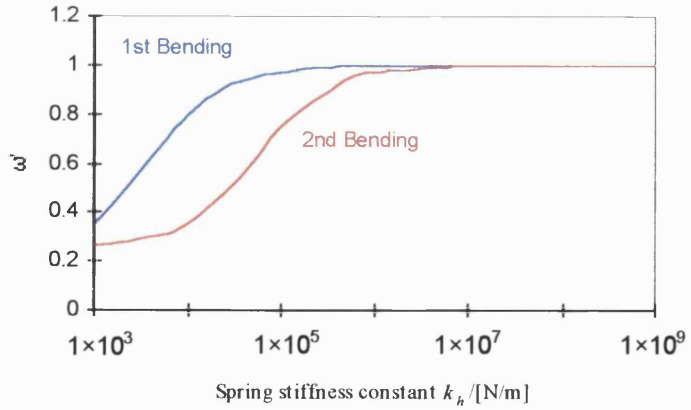

b)

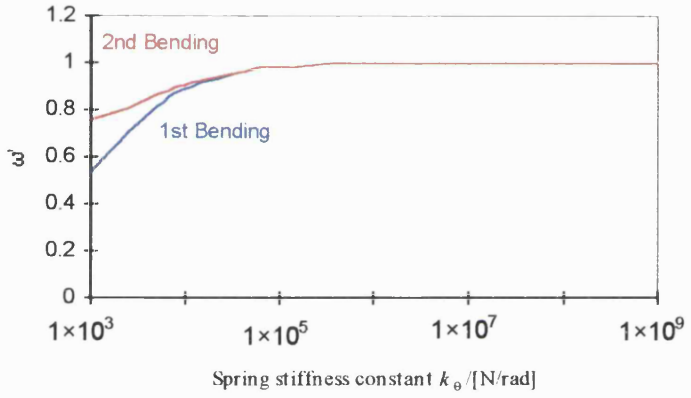

c)

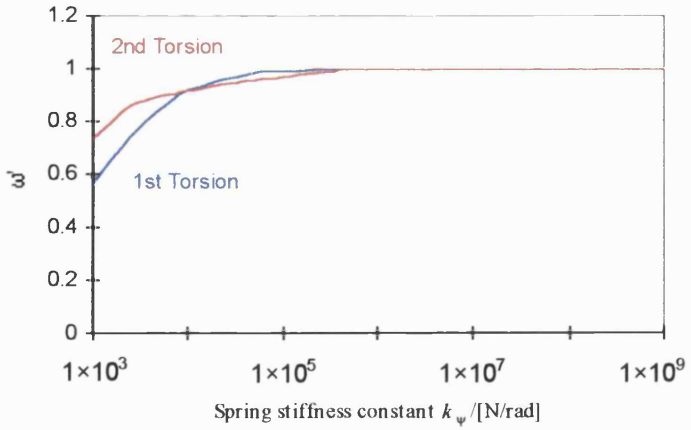

Figure 3.3.1 - Variation of ω' (natural frequency normalised to the maximum frequency) with boundary condition stiffness for a 1m×0.1m×0.01m aluminium beam

a) Variation of bending modes with k_h

b) Variation of bending modes with k_θ

c) Variation of torsion modes with k_ψ

3.3.2 Damage Detection using DOT

Once the characterisation has been carried out to reduce the error between the undamaged experimental data and the analytical model, the delaminations can be detected using the experimental data for the damaged beam. Because the damage is assumed to have occurred with the beam in-situ, the material properties and boundary conditions obtained from the characterisation process are assumed to remain constant for the damaged beam. (Note that later in this thesis, experimental results for damaged and undamaged beams are compared. In this case, the damaged and undamaged results are not obtained from the same beam. However, out of necessity it is assumed that the material properties and boundary conditions remain the same.)

The objective function is the same as for the characterisation stage, defined in equations (3.3.1) and (3.3.2).

The design variables define the location and size of the delaminations, and the number of delaminations are specified at the start of the optimisation. The design variables are defined as:

$$X_{2i-1} = \frac{l_{ai}}{l} \quad ; \quad X_{2i} = \frac{l_{di}}{l} \qquad i = 1...n_{delams} \qquad \text{... (3.3.15)}$$

where n_{delams} is the number of delaminations, and the other variables are shown in figure 3.3.2. If there is only one delamination, equation (3.3.15) reduces to:

$$X_1 = \frac{l_a}{l} \quad ; \quad X_2 = \frac{l_d}{l} \qquad \text{... (3.3.16)}$$

The dimension l_b shown in figure 3.3.2 is the through-thickness ply location of the delamination, which is a discrete design variable. A discrete design variable cannot be handled by the gradient-based optimiser used within this thesis, and the measures taken to overcome this are described later.

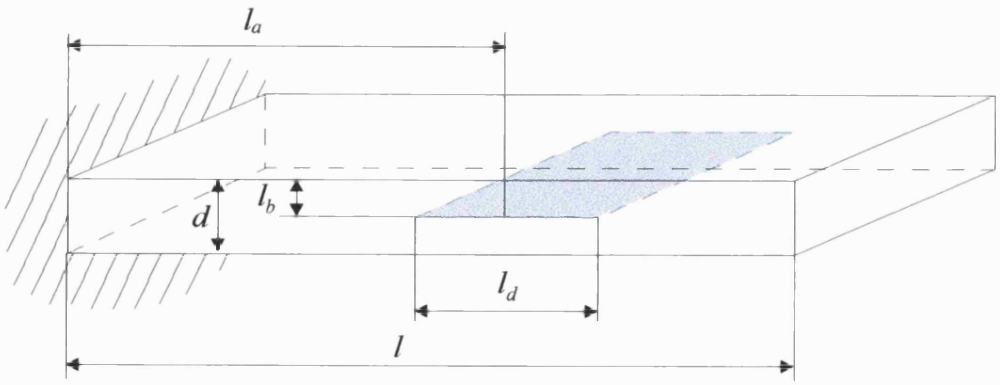

Figure 3.3.2 - Cantilever beam with a single delamination

To ensure that the start of each delamination lies after Y=0, i.e. that the delaminations lie within the beam, the lower bounds of the design variables used to describe the position of the delamination are defined as:

$$X_{L(2i-1)} = \frac{X_{2i}}{2} \qquad i = 1 \ldots n_{delams} \qquad \ldots (3.3.17a)$$

Also, the constraints ensure that the sum of the delamination length and the location of the delamination does not exceed the total length of the beam:

$$G_i(X) = \frac{X_{2i-1}}{2} + X_{2i} - 1 \leq 0 \quad i = 1 \ldots n_{delams} \qquad \ldots (3.3.17b)$$

When the problem includes multiple delaminations, or one or more delamination occurs at some ply location through the thickness of the laminate (l_b), a series of optimisation processes must be undergone.

For instance, if the problem is to locate a single delamination, where the ply location is not known, an optimisation run must be carried out for every discrete ply location, and the minimum objective function used to denote the correct location. This is also true if the exact number of delaminations is not known, where upon an optimisation run must be undertaken for all the possible combinations of delamination number and ply location. This would soon become

prohibitively time consuming as the problems became more complex, but some results for simple problems are given in chapter 7.

3.3.3 Damage Detection using Genesis

Use of the genetic algorithm overcomes some of the limitations of the gradient-based optimisation method, by allowing discrete values. The method used to encode the structural information into the gene, and the method used to incorporate the constraints, is given here.

As the genetic algorithm uses a binary gene to carry out the optimisation, the structural information contained in the design variables must be encoded into binary form. This was carried out using the "floating point to binary" encoding contained within GENSIS. Here, each design variable can be a floating point number, but can only have a finite number of values, the number of which must be a power of 2.

For one delamination in the Y direction, the design variables for the optimisation can be written (with reference to figure 3.3.2) as:

$$X_1 = \frac{l_a}{l} \qquad \text{(1024 possible values)} \qquad \ldots (3.3.18)$$

$$X_2 = \frac{l_d}{l} \qquad \text{(1024 possible values)} \qquad \ldots (3.3.19)$$

$$X_{2+j} = [\textit{Number of delaminations at ply position } j] \qquad j = 1 \ldots n_{plies} - 1$$

$$\text{(2 possible values - } \{0,1\}) \qquad \ldots (3.3.20)$$

If the number of delaminations in the Y direction is unknown, equations (3.3.18) to (3.3.20) become:

$$X_{1+(i-1)(n_{plies}+1)} = \frac{l_{ai}}{l} \qquad i = 1 \ldots n_{delamsY} \qquad \ldots (3.3.21)$$

$$X_{2+(i-1)(n_{plies}+1)} = \frac{l_{di}}{l} \qquad i = 1 \ldots n_{delamsY} \qquad \ldots (3.3.22)$$

$$X_{2+j+(i-1)(n_{plies}+1)} = [Number\ of\ delaminations\ at\ ply\ position\ j]$$

$$i = 1...n_{delamsY},\ j = 1...n_{plies} - 1 \qquad \ldots (3.3.23)$$

where $n_{delamsY}$ is the maximum number of delaminations allowed for the in the Y direction, and n_{plies} is the number of plies in the laminate. Equations (3.3.18) and (3.3.21) define the location of each delamination in the Y direction, and equations (3.3.19) and (3.3.22) define the size of the delamination in the Y direction. Also, equations (3.3.20) and (3.3.23) define the number and location of the delaminations in the Z direction. This is achieved by designating locations in the binary gene as ply locations, and denoting a 0 as no delamination and a 1 as a delamination at that location. It is assumed that through the thickness of the laminate, each delamination has the same size.

This can best be explained by the use of a simple example. Consider the delamination arrangement in figure 3.3.3. There is only one set of delaminations in the Y-direction, hence in equations (3.3.21) to (3.3.22) $n_{delamsY}$=1 (which is equivalent to equations (3.3.18) to (3.3.20)). The centre of the set of delaminations is located at Y=0.4502, and has a non-dimensional length of 0.1052. The laminate has four plies (n_{plies}=4), and the delaminations in the set are located after plies 2 and 3. Hence, for this example:

$$X_1 = 0.4502$$
$$X_2 = 0.1052$$
$$X_3 = 0$$
$$X_4 = 1$$
$$X_5 = 1$$

This is encoded in binary form in figure 3.3.3b.

To ensure that the sum of the delamination size plus the delamination location is not larger than the length of the beam, a penalty function was introduced. This performs the same function as the constraints in the gradient-based optimisation, but is achieved by adding terms to the objective function when the design is in an unfeasible region. The objective function becomes:

$$O'(X,r) = O(X) + \sum_{i=1}^{n_{con}} P_i\left(G_i(X)\right) \qquad \ldots (3.3.24)$$

where the prime denotes the transformed objective function. The penalty function $P\left(G(X)\right)$ is a quadratic loss function, given by:

$$P_i\left(G_i(X)\right) = r\left(\max\left\{0, G_i(X)\right\}\right)^2 \qquad i = 1 \ldots n_{con} \qquad \ldots (3.1.25)$$

where r is a scalar chosen by the user and G_i is the constraint given in equation (3.3.17b).

The processes outlined above are used to detect delaminations for a number of experimental and numerical problems, and the results are given in Chapter 7.

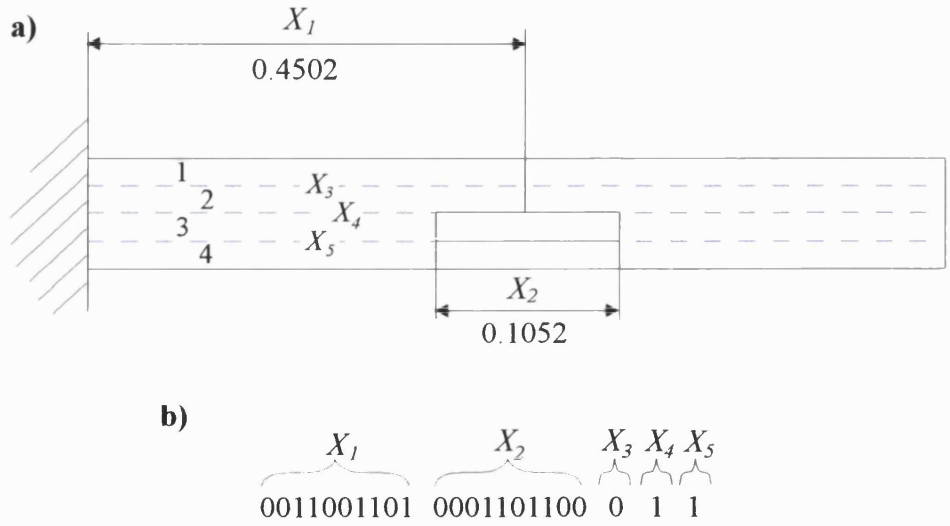

Figure 3.3.3 - Example of structural encoding within GENESIS

a) 4-Ply laminate with two delaminations after plies 2 and 3

b) Binary gene for the structural example

4. Numerical Results for Static and Dynamic Analysis of Delaminated Beams

In Chapter 2 the method used to predict the effect of delaminations on the frequencies and mode-shapes of composite beams was described. In this chapter, the equations derived in Chapter 2 are used to describe the effects of laminate geometry, and also the effects of size, location and number of delaminations on the vibrational behaviour of beams. The static beams models outlined in Chapter 2 are compared to finite element models, and comments are made as to the accuracy of the assumptions.

4.1 Static Beam Model Results

In this section the equations derived in Chapter 2 are used to investigate the behaviour of delaminated beams under static loading. The effect of delamination size and location is investigated, and results from the static beam model are compared with FE results. To help in the understanding of the behaviour, section 4.1.1 describes the behaviour of an isotropic beam, which possesses no material coupling. In section 4.1.2 the effect of laminate geometry is investigated, by applying the equations to delaminations that cause symmetric and un-symmetric sub-laminates.

4.1.1 Isotropic Beam

In order to fully understand the effects of delaminations predicted by the static beam model, a simple beam without coupling terms, and with a single delamination was used. The simplest type of "delaminated" beam is a homogeneous, isotropic material (i.e. not a laminated material), with a single, full-width slit running parallel to the *X-Y* plane.

Using equations (A10), (A18) and (A23) in appendix A (which gives the full analysis for n-1 delaminations), for any arbitrary loading, the bending moments, shear forces and axial forces acting on each sub-laminate can be obtained. Using these values and equation (A5) when $y \leq l_d$, the deflected shape of each sub-laminate can be calculated, and compared to the deflected shape obtained by the finite element method.

For this investigation the equations were applied to an aluminium beam with a full-length centre-line delamination, shown in figure 4.1.1. This had a length of 1m, a width of 0.1m and a

thickness of 0.01m, and had 20N applied to the tip. The material properties used in the analysis are given in table 4.1.1.

$E = 73.0\times10^9$ Pa	$G = 28.0\times10^9$ Pa
$\nu = 0.33$	$\rho = 2800.0$ kg/m^3

Table 4.1.1 - Material properties of the aluminium beam

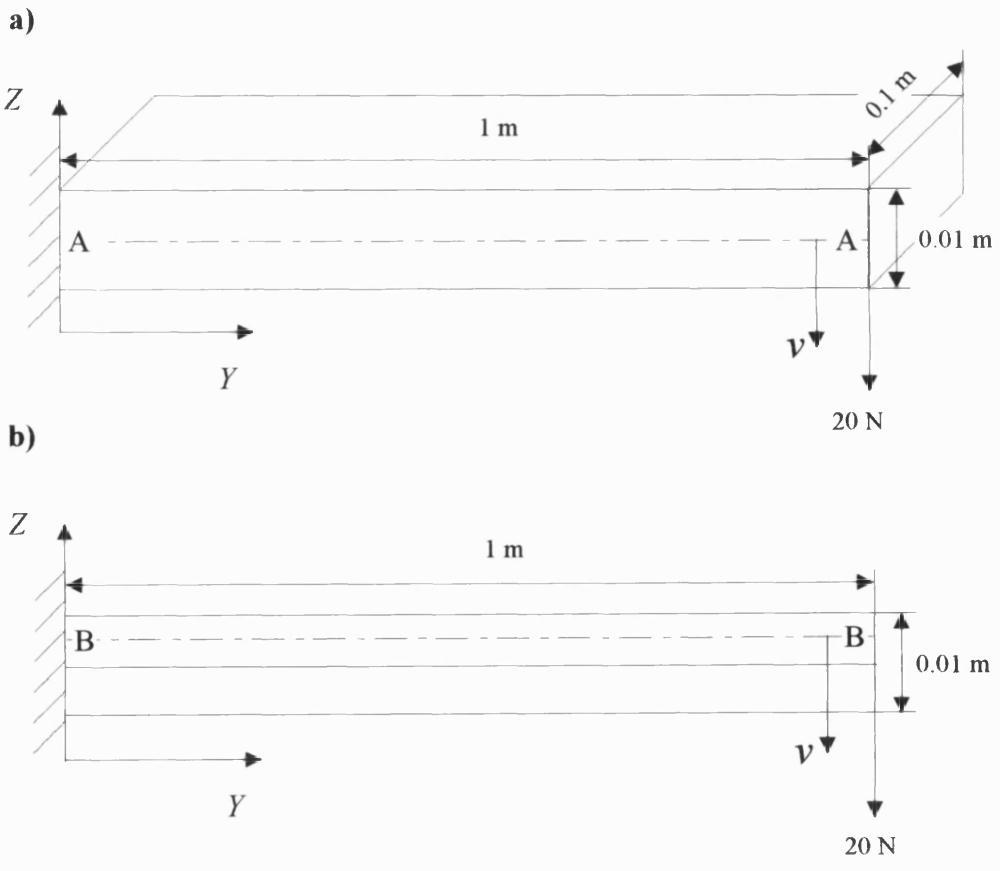

Figure 4.1.2 – (a) Undelaminated and (b) delaminated aluminium beam

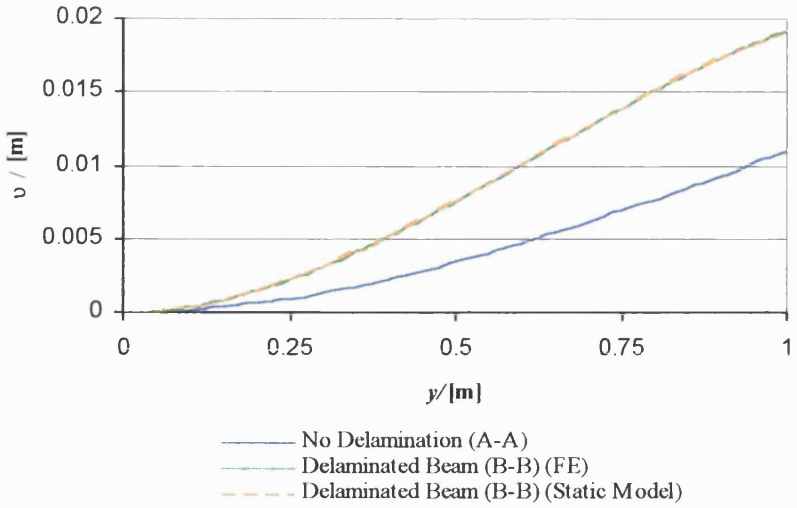

Figure 4.1.2 – Comparison of the deflection of an aluminium beam with a delamination produced by the static model and by the finite element method

In figure 4.1.2 the deflected shape of the top sub-laminate of the aluminium beam with a centre-line delamination (line A-A in figure 4.1.1), is shown. The centre line curve for the undelaminated beam (line B-B) is shown for comparison. These curves were calculated using the static beam model, and the 3 dimensional FE model described in chapter 2. This had 100 elements along the length (element length 0.01m), 6 elements along the width (element width 0.0167m), and 8 elements through the thickness of the beam (element thickness 0.00125m). It can be seen that, in this case, the static beam model agrees well with the FE model.

The curves of the delaminated beam in figure 4.1.2 show double curvature, with the curvature changing from positive to negative, which is typical of those produced by a delaminated cantilever beam. This is due to the fact that the bending moment changes sign from positive to negative towards the tip of the beam. This change in sign is necessary to counteract the couple due to the axial forces P_{A2} and P_{B2}, shown in figure 2.3.2.

Figure 4.1.3 shows the direct stress distribution at three sections along the beam length calculated by FE. By using simple graphical integration, the bending moment and axial forces can be obtained. These are assumed to be of the form shown in figure 4.1.3 (b), where the bending stress varies linearly between maximums at the top and bottom surfaces of the sub-laminate, with zero bending stress at the neutral axis. The stress due to the axial forces is assumed to remain constant through the thickness of each sub-laminate.

a)

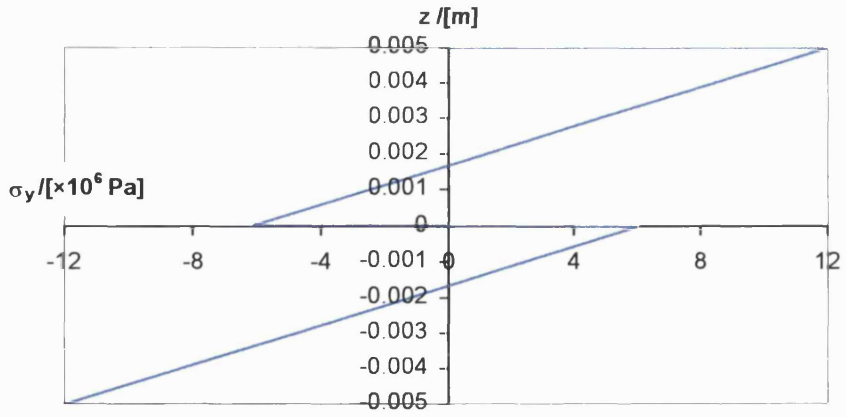

b)

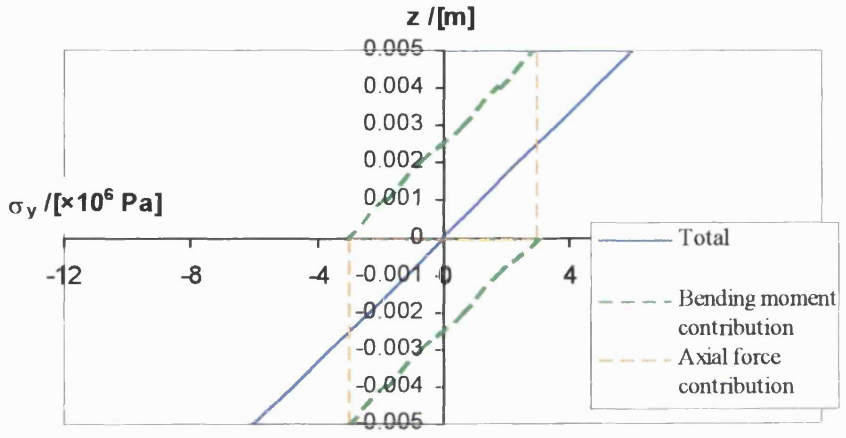

c)

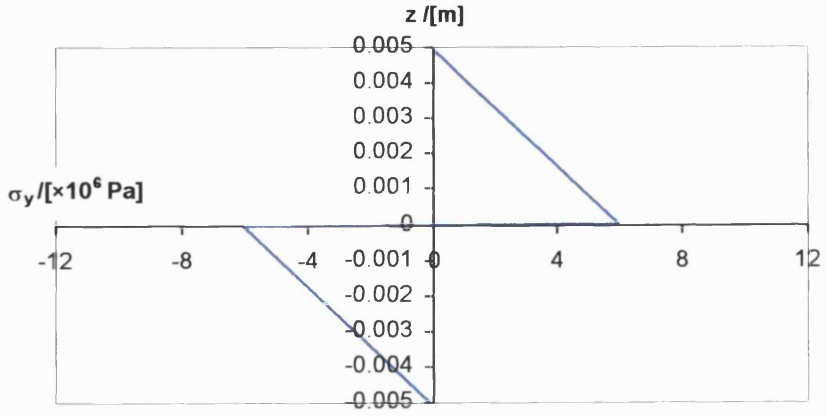

Figure 4.1.3 – Direct stress distribution for an aluminium cantilever beam

a) y =0.25 m b) y = 0.5 m c) y =0.75 m

The bending moment distribution and the couple due to the axial forces is plotted along the length of the beam in figure 4.1.4. Assuming a linear distribution of bending moment along the beam, the bending moment and axial force extrapolated to act at the end of the laminate, shown as dashed lines (M_{A1} and $P_{A2}\left(\bar{z}_A - \bar{z}_B\right)$, see equation (2.3.3)), agree with the beam model.

When examining the direct stress distribution produced by the FE model at the ends of the beam, the assumption of linear bending moment along the length of each sub-laminate was seen to be incorrect, as out-of-plane stresses appear at the joined ends of each sub-laminate. However, these act over a very small length compared to the overall length of the beam, and were therefore ignored.

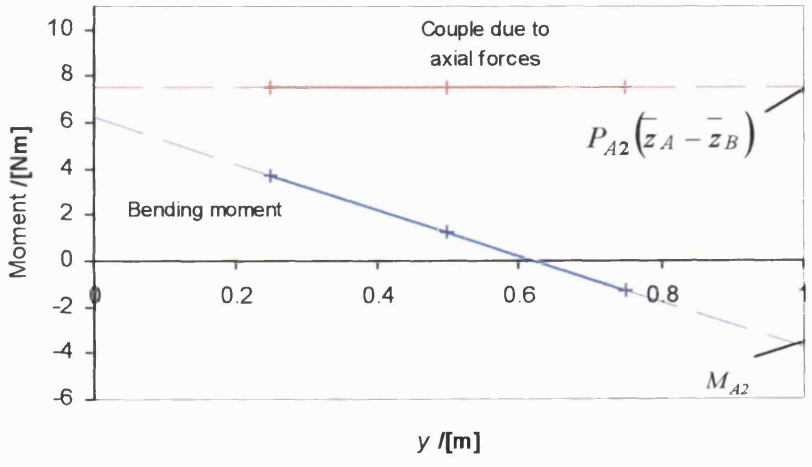

Figure 4.1.4 – Moment distribution acting on one sub-laminate of a delaminated aluminium beam

4.1.2 Effect of Laminate Geometry

The effect of laminate geometry on the stiffness of delaminated composite laminates can be determined with reference to the equations derived in Chapter 2. By varying individual properties of sub-laminates, the effect of different fibre orientations and material properties can be determined.

In this section, the effect of varying the individual components in equation (2.3.19) is described. By artificially treating the components as independent from one another, the contributions to the equivalent shear rigidity can be isolated. The effect of varying sub-laminate bending rigidity, axial stiffness and bending-axial coupling are discussed. This is necessarily a simplified discussion of the problem. With an actual delaminated laminate, the effect is a more complicated combination of these components.

It is also important to determine in each case whether it is valid to vary individual properties, as many structural properties are related. For clarity, it is assumed in this discussion that there is only a single centre-line delamination, creating sub-laminates A and B.

- Sub-Laminate Bending Rigidity:
  It is obviously not possible to vary the bending rigidity of a sub-laminate independently of the bending rigidity of the whole laminate. Assuming a symmetric laminate geometry for each sub-laminate to ensure no bending-axial coupling, the ratio of the sub-laminate bending rigidity to undelaminated bending rigidity $(EI)_A/EI$ was therefore varied and the effect of shear rigidity noted. As the ratio of the bending rigidities increases, so the effective shear rigidity of the delaminated section increases. This is because the shear rigidity is a function of the difference in deflections of the delaminated laminate and the equivalent undelaminated section. The deflection of the delaminated section is proportional to the inverse of the sub-laminate bending rigidity, and the deflection of the equivalent undelaminated section is proportional to the inverse of its bending rigidity. Therefore, as these values converge, so the deflections of the delaminated and equivalent laminates converge, resulting in converging values of shear rigidity.
- Sub-Laminate Axial Stiffness:
  The effective shear rigidity of the delaminated laminate is dependent upon the sub-laminate axial stiffness as it determines the amount of axial force necessary to align the sub-laminate end faces, shown in figure 2.3.1. As the axial stiffness $(EA)_A$ and $(EA)_B$ of the sub-laminates increases, the effective shear rigidity of the delaminated laminate increases. This is because as the axial stiffness of the sub-laminates increase, more force is required to align the sub-laminate end-faces. Therefore the moment produced by the couple of these forces is greater. As this moment is acting in the same direction as the internal bending moment distribution, for equilibrium the internal bending moment is lower. The sub-laminates therefore deflect less under the same applied load, which results in a higher effective rigidity. Sub-laminate axial stiffness can be increased independently

of the other parameters by changing the order of the plies. For example, increasing the number of 0° plies in a sub-laminate increases its axial stiffness, but locating them closer to the neutral axes can ensure that the bending rigidities remain constant.

- Sub-Laminate Bending-Axial Coupling:

  It is difficult to vary bending-axial coupling rigidity independently of the bending rigidity, and the effect of bending rigidity is far greater than that of bending-axial coupling. Therefore, to determine the effect of bending-axial coupling, the bending rigidity was kept artificially constant. This gives an insight into the effect of bending-axial coupling, which is combined to the effect of varying bending rigidity outlined above. If it is assumed that the undelaminated laminate is symmetric and has a centre line delamination, the bending-axial coupling constant of the top sub-laminate is equal and opposite in sign to the bending-axial coupling constant of the lower sub-laminate. In this situation, increasing the bending-axial coupling constant of the top laminate increases the effective shear rigidity of the laminate. This is because the axial forces in the sub-laminates act via the bending-axial coupling to reduce the bending of the cantilever. As the bending-axial coupling increases, the bending of the beam reduces to that of the undelaminated laminate, and the axial forces in the sub-laminates reduce to zero. The static beam model therefore predicts that the effective shear rigidity of the delaminated laminate converges asymptotically to that of the undelaminated laminate.

The accuracy of the static model can be determined by comparison with the FE model. Figure 4.1.5 shows the deflection of 1m long composite cantilever beams with widths of 0.1m and a 20N force at their ends. Each beam has a full-length delamination at the centre of the laminate. Each ply is 1.25mm thick, thereby eliminating elements with high aspect ratios in the FE model. A carbon-fibre epoxy laminate was assumed for the following analyses, with material properties given in table 4.1.2. This material was also used for the experimental beams, and is therefore described in more detail in Chapter 5.

Each laminate had 8 plies of this 1.25mm thickness, giving a total beam thickness of 0.01m. The FE model was identical to the model for the aluminium beam, with 100×6×8 elements. Because the 3-D element used in the model averages the stress through the thickness of the beam (Swanson Analysis Systems Inc. (1992)), it can sometimes give an inaccurate direct stress distribution for laminated materials. This effect is reduced by using more elements through the thickness of the laminate, but this was not possible due to limitations of the computing facilities involved.

Figure 4.1.5 (a) shows the deflection of a $[(0°,90°)_2]_s$ laminate. The inaccuracy of the FE model can be seen by examining the curves of the undelaminated beams, which no longer agree exactly. However, the relative deflections of the undelaminated and delaminated beams predicted by the FE model and the static beam model are such that the calculated values of shear rigidity are similar.

$E_1 = 138.0\times10^9$ Pa	$\nu_{12} = 0.263$	$G_{12} = 1.07\times10^9$ Pa
$E_2 = 9.65\times10^9$ Pa	$\nu_{23} = 0.263$	$G_{13} = 1.07\times10^9$ Pa
$E_3 = 9.65\times10^9$ Pa	$\nu_{31} = 0.018$	$G_{23} = 5.38\times10^8$ Pa
$\rho_{measured} = 1645$ kg/m^3		

Table 4.1.2 - Material properties of a Carbon-fibre/epoxy ply

Figure 4.1.5 (b) shows the deflection of a $[(90°,0°)_2]_s$ laminate. Again, the deflection of the undelaminated beam predicted by the FE model and the static model do not agree. Owing to the stress averaging of the *SOLID46* elements, the FE model predicts that the undelaminated $[(90°,0°)_2]_s$ beam will deflect only slightly more than the $[(0°,90°)_2]_s$ laminate. The FE model predicts that the undelaminated $[(0°,90°)_2]_s$ laminate has a deflection of 0.010 m, and the $[(90°,0°)_2]_s$ laminate a deflection of 0.012 m. This can be compared to the correct values of 0.008 m and 0.016 m calculated using the static beam model.

The two laminate geometries in figure 4.1.5 were chosen to show the effects of bending-extension coupling. A $(0°,90°)_2$ laminate has equal bending and extension rigidities to a $(90°,0°)_2$ laminate, but has opposite sign bending-extension coupling. When delaminated at the centre of the laminate, the $[(0°,90°)_2]_s$ laminate creates a top sub-laminate with $(0°,90°)_2$ lay-up, which has positive bending-extension coupling, and the bottom laminate has a $(90°,0°)_2$ lay-up with negative bending-extension coupling. The sign of the axial forces calculated in equation 2.3.17 is such that the extension-bending coupling causes decreased bending of the laminate. The deflections of the delaminated $[(0°,90°)_2]_s$ and $[(90°,0°)_2]_s$ beams are 0.019 m and 0.020 m respectively, for the FE model, and 0.018 m and 0.021 m respectively, for the static beam model. If the undelaminated

curves produced by the FE model were more accurate, the difference in end-deflection between the delaminated and undelaminated beams predicted by the FE model and the static beam model would be similar, and the calculated values of shear rigidity would show good agreemment.

a)

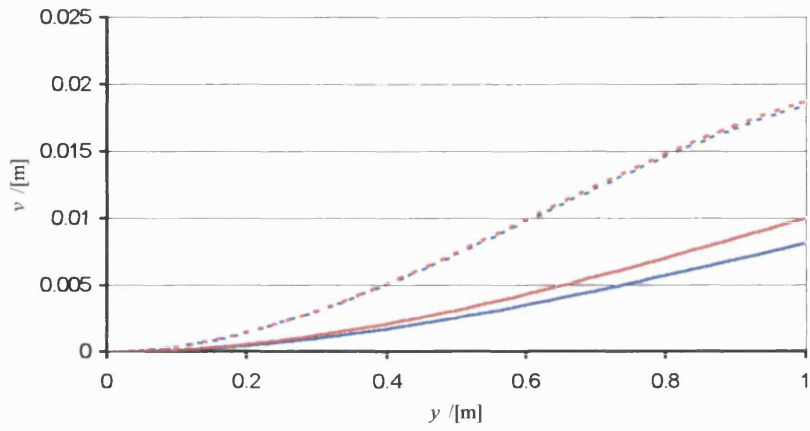

b)

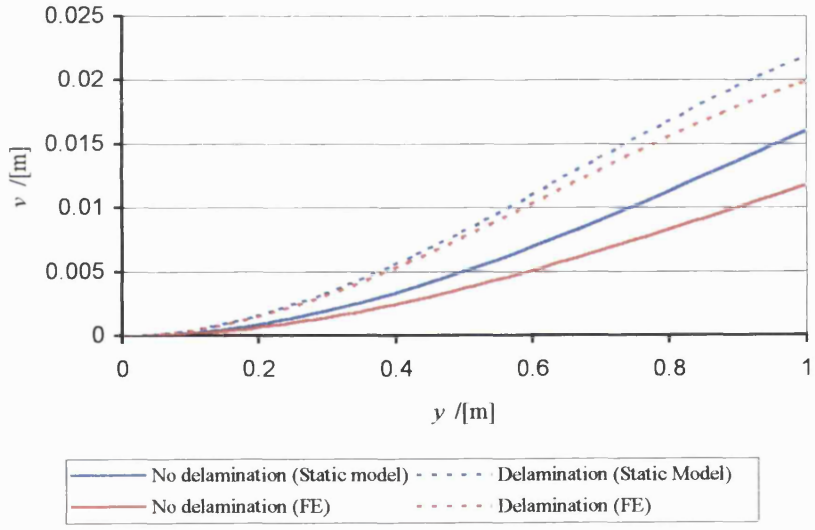

Figure 4.1.5 – Deflection of delaminated and undelaminated cantilever beams under a 20N load
a) $[(0°,90°)_2]_s$
b) $[(90°,0°)_2]_s$

Table 4.1.3 compares the values of effective shear rigidities of delaminated beams with different laminate geometries, calculated using equation 2.3.24. The beam dimensions are identical to the

previous example. It can be seen from the table that the static beam and FE models agree for unidirectional laminates, but disagree for laminates which create unsymmetric sub-laminates when delaminated. For the (45°,0°,90°,-45°)s laminate, which has a bending-extension coupling constant of $\approx 4\times10^{-5}$ $(Nm)^{-1}$, the static beam model underpredicts the effective shear rigidity by approximately 3 times. Some of this difference is due to the inaccuracies of the FE model; for example, the FE model predicts that the delaminated $(-45°,90°,0°,45°)_s$ laminate has a higher value of effective shear rigidity than the $(45°,0°,90°,-45°)_s$ laminate, which is incorrect. However, it is considered that most of the disagreement from the models comes from assuming that the laminates were symmetric when calculating the bending rigidity used in the static beam model. By approximating the effects of bending-extension coupling to a constant term the accuracy of this simplification is improved, but for highly unsymmetric laminates the value for effective shear rigidity of a delaminated laminate calculated by the static beam model still remains inaccurate.

Lay-up	$(kAG)'$ (FE) /[N]	$(kAG)'$ (static model) /[N]
0_8	3513.0	3683.4
90_8	256.9	257.2
$[(0°,90°)_s]_s$	2029.4	3790.8
$[(0°,90°)_2]_s$	1833.2	1551.0
$[(90°,0°)_2]_s$	1974.3	2731.8
$(45°,0°,90°,-45°)_s$	1203.9	362.3
$(-45°,90°,0°,45°)_s$	1258.6	336.8

Table 4.1.3 – Effective shear rigidity for 1m delaminated beams predicted by the FE and static beam models (Material properties given in table 4.1.2)

4.2 Effect of Delamination Location on the Dynamic Behaviour of Beams

In order for the optimisation process to be able to locate delaminations within a laminate, the natural frequencies or mode-shapes of the delaminated beam must depend on the location of the delaminations.

For convenience, figure 4.2.1 shows the delaminated beam given in figure 3.3.2, showing the definition of the delamination size and position. To investigate the effect of delamination location on the dynamic behaviour of a cantilever beam, a delamination was placed at different positions within the beams and the effect noted.

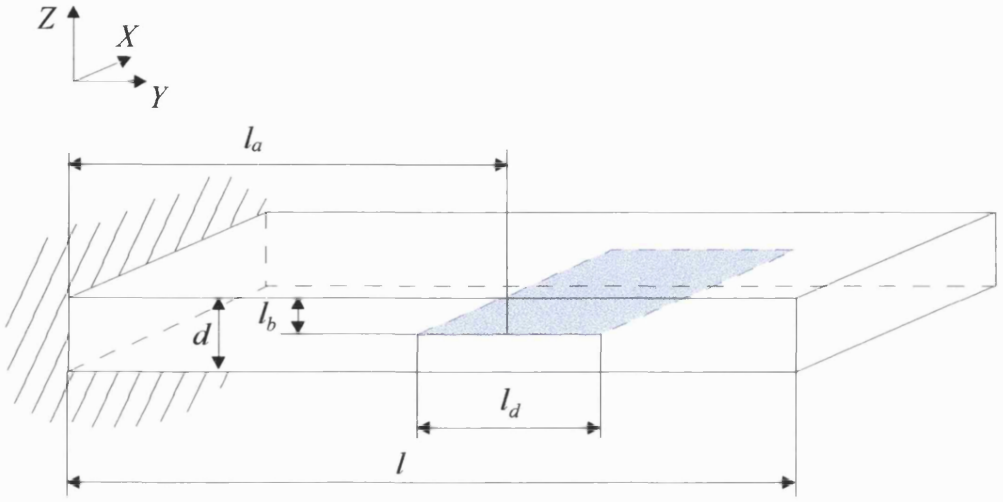

Figure 4.2.1 – Cantilever beam with a single delamination

As described in Chapter 2, to model a delamination with the DSM, the beam is split into elements along the *Y*-axis, and a delamination is modelled as a number of elements with reduced shear and torsional rigidities. Since the DSM is a one-dimensional beam model, the location of the delamination in the Z-direction will only have an effect if either of the rigidities vary. Figure 4.2.2 shows the variation of shear and torsional rigidities with l_b for the aluminium beam described in the previous section. In this case, both the size and axial position of the laminate were constant ($l_a = 0.5l$, $l_d = 0.05l$). It can be seen that the shear rigidity is lowest for a centre-line delamination, and that it increases towards the edges of the laminate. This is to be expected as the shear stress is maximum at the centre of a beam that is symmetric about the *Y*-axis. Likewise the torsional rigidity decreases as the delamination moves towards the centre of the delamination. This is because the torsional rigidity is proportional to the cube of the thickness. This has more of an effect than summing the torsional rigidities of each individual sub-laminate, which, according to equation (2.3.29), determines the effective torsional rigidity of a delaminated laminate.

a)

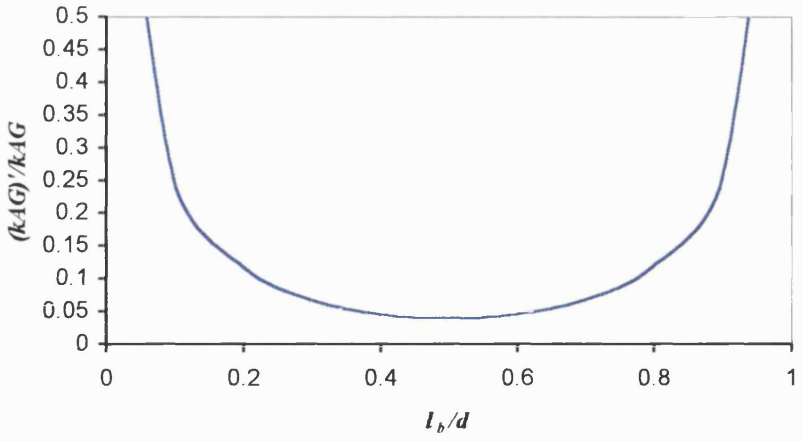

b)

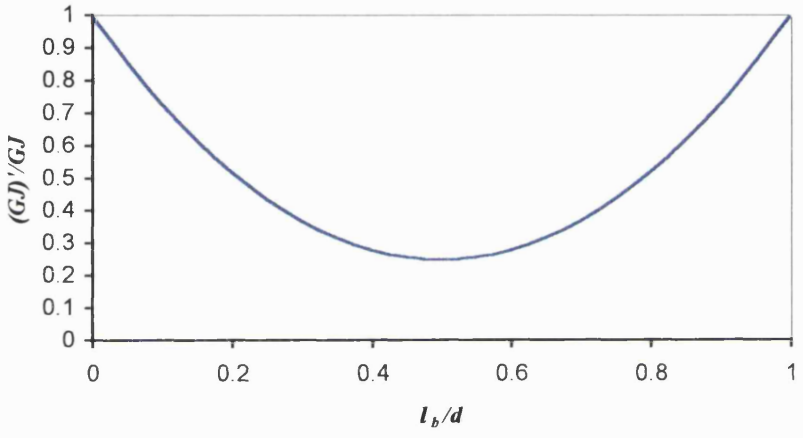

Figure 4.2.2 – Reduction in rigidity of an aluminium delaminated beam with varying position of delamination

a) Normalised shear rigidity

b) Normalised torsional rigidity

This is obviously more complicated for laminates with complicated structural geometries, when the parabolic distribution of effective shear and torsional rigidity against through-thickness position of delamination might no longer occur. Figure 4.2.3 shows the variation of shear and torsional rigidities with l_b for $[(0°,90°)_s]_s$, $[(0°,90°)_2]_s$ and $[45°,0°,90°,-45°]_s$ laminates. Figure 4.2.3 (a) shows the effect on shear rigidity. The pattern obtained by moving the delamination through the thickness of the laminate can be understood by determining which layers have the greatest effect on the bending stiffness of the laminate. For the laminates shown in figure 4.2.3 (a), the 0° layers, followed by the 45° layers, have the greatest Young's modulus in the Y direction and therefore contribute most to the axial stiffness and bending rigidity of each sub-laminate. Therefore, when a delamination causes the total thickness of the 0° layers to reduce, the beam will deflect more under load and therefore result in a lower effective shear rigidity. This can be most clearly seen when the delamination is located at the first ply intersection, as the shear rigidity drops sharply for the for $[(0°,90°)_s]_s$ and $[(0°,90°)_2]_s$ laminates, and less so for the $[45°,0°,90°,-45°]_s$ laminate.

This effect is further complicated by the bending-axial coupling caused by un-symmetric sub-laminates, although this effect is smaller than the effect of bending rigidity. For example, when the $[(0°,90°)_2]_s$ laminate is delaminated at the centre-line it creates a $(0°,90°)_2$ laminate and a $(90°,0°)_2$ laminate. These have bending-extension coupling constants which decreases the bending of the beam, causing the effective shear rigidity to be closer to that of the $[(0°,90°)_s]_s$ laminate. This effect is, however, small. With the bending-extension coupling excluded, the effective shear rigidity for a 0.1m delamination reduces from 1.20×10^5N to 1.09×10^5N.

a)

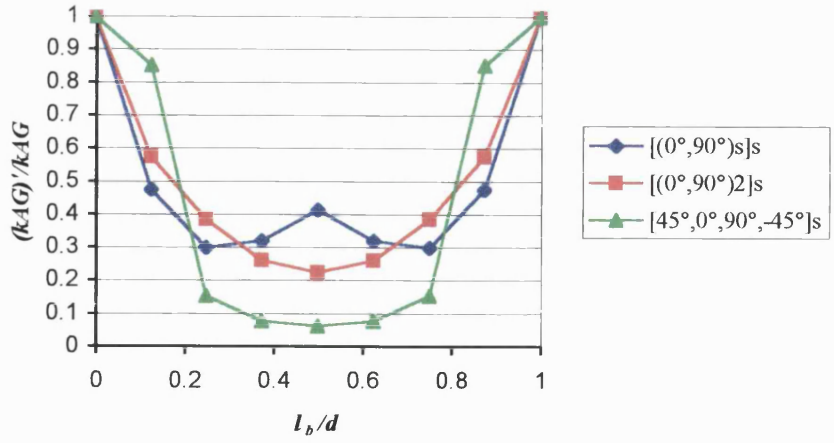

b)

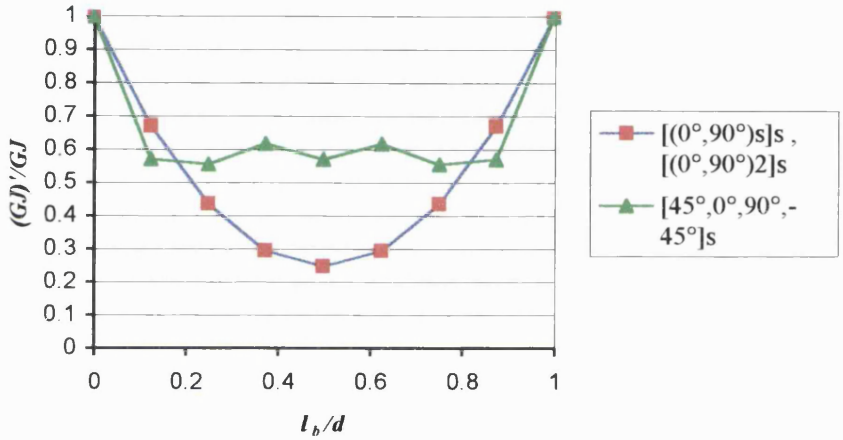

Figure 4.2.3 – Variation of rigidity with delamination position for three example laminates

a) Normalised shear rigidity

b) Normalised torsional rigidity

Figure 4.2.3 (b) shows the reduction in torsional rigidity with delamination position for the same laminates. Even though the torsional rigidity for the delaminated beams will be under-estimated because of the reasons outlined in Chapter 2, it is expected that the results here will show the same general trends as a model that includes compatibility of the end-faces. Figure 4.2.3 (b) shows that the two laminates made up of only 0° and 90° layers do not show any difference in torsional rigidity, since the torsional rigidity for a 0° ply is equal that of a 90° ply. However the third laminate geometry shows a different pattern as the delamination moves through the thickness of the laminate. This is because the 45° layers are more torsionally rigid than the 0° or 90° layers, and reducing the effective thickness of these has a much greater effect. If the end-face

compatibility condition was included in the model it is expected that the 45° plies would have an even greater effect, as they also contribute more to the shear rigidity in the transverse direction than the 0° or 90° plies (G_{xy}, where the axes are shown in 4.2.1).

When modelling a delamination using the static model, the shear rigidity is calculated assuming the delamination is full-length along the cantilever. This simplification means that the shear rigidity is independent of the location along the Y-axis. This is also true of the torsional rigidity. Therefore, for a delamination to show the effect of axial location, the natural properties must be affected by the location of the reduced shear and torsional rigidities. The variation of bending frequency, normalised with respect to the frequency of the undelaminated mode, with axial location for the aluminium beam with $l_b = 0.5d$ and l_d=0.1l, is shown in figure 4.2.4. It can be seen that as a delamination moves into a position of high shear stress for a particular mode, the frequency reduces. Using simple beam deflection theory, the shear stress is proportional to the derivative of the curvature of the beam, i.e.:

$$-\kappa' = -v''' = \frac{S}{EI}$$

So that maximum shear stress is seen at the maximum rate of change of curvature of a mode, a point of inflection. The relative shear stress distribution (shown as normalised third derivative of deflection) for the fourth mode shape is shown in figure 4.2.5.

The magnitude of the beam curvature is greater if there are more points of inflection in a mode. Therefore a delamination has a greater effect on higher order modes. In figure 4.2.4, the maximum frequency reduction for the fourth bending mode (labelled 4B) is approximately 25% greater than for the third, which is itself over 150% greater than for the 2nd bending mode. Because there is relatively little curvature in the fundamental bending mode, the frequency reduction is significantly smaller.

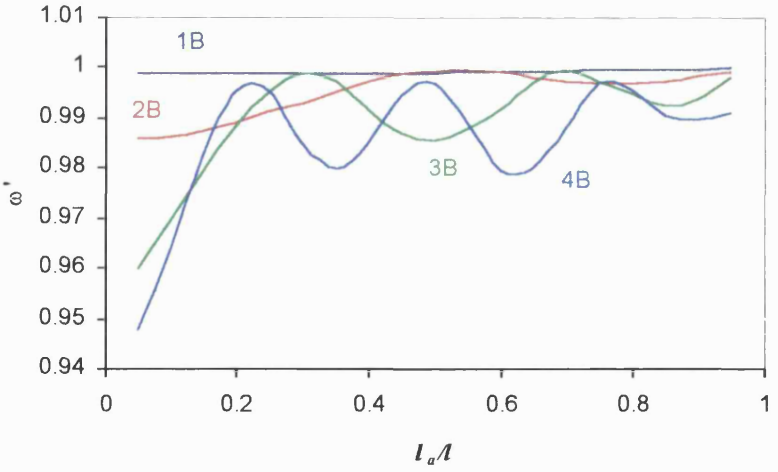

Figure 4.2.4 – Normalised bending frequencies (normalised with respect to the equivalent undelaminated frequency) for an aluminium beam with a delamination at different axial locations

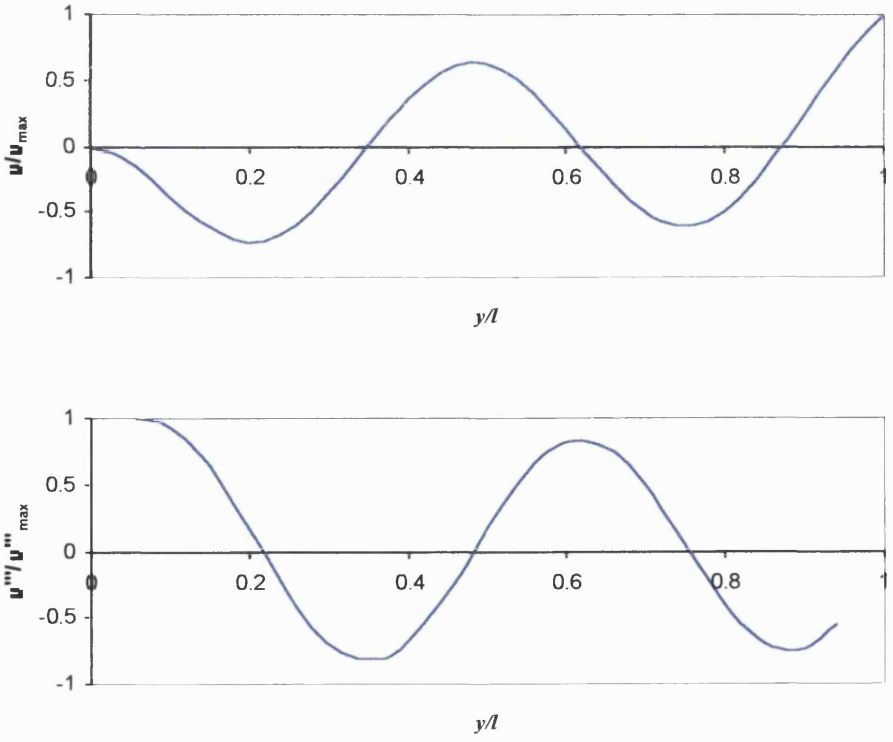

Figure 4.2.5 – Normalised displacement and corresponding shear force distribution for the fourth bending mode of a cantilever beam

Despite the fact that the torsional model outlined in Chapter 2 is considered to predict the 'worst-case' torsional rigidity, the same analysis carried out for the bending modes was also carried out for the torsional modes. This is valid because a reduction in torsional rigidity applied to the DSM will give similar trends to using a torsional rigidity calculated by a more accurate model, but will underestimate the torsional frequencies. Figure 4.2.6 shows the variation of torsional frequency with delamination position for the aluminium beam with $l_b = 0.5d$ and $l_d=0.1l$. It can be seen from this figure that, apart from the frequency of the fourth torsion mode, the effect of the reduced torsional rigidity is similar to the effect of reduced shear rigidity on bending frequencies. The greatest effect on the torsional frequency is seen when the delamination lies in a region of high shear stress, which for a given cross-section and location within the cross-section, is proportional to the first derivative of the torsional deflection of the beam. The static model also predicts that the greatest effect will be seen for the lower-order modes. This was not however verified by the FE model or by experiment, which, as shown later, showed approximately equivalent reductions in frequency for all modes (at different positions of delamination). The variation of frequency for the fourth torsion mode does not appear to show the same characteristics as the first three modes, as the variation in frequency is much lower, and appears to be very similar in shape to the variation in frequency for the third mode. This may be due to the DSM calculating a second, fourth order torsion mode (a mode with three peaks or troughs), which has a higher frequency, but otherwise shows the same behaviour as the third torsion mode. This effect, which has also been observed for lower order modes, causes a problem when applying the DSM to damage detection. If a second mode of the order n is calculated by the DSM, it will be compared to a mode of order n+1 when integrated into the objective function, causing an erroneous result during the optimisation process.

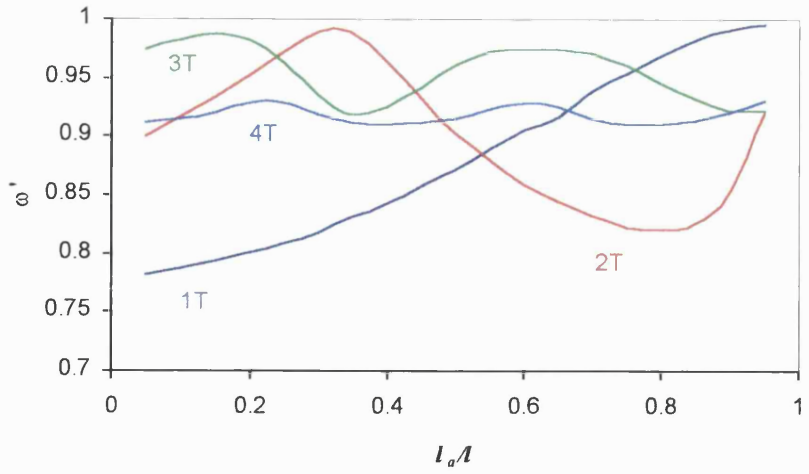

Figure 4.2.6 - Normalised torsional frequencies for an aluminium beam with a delamination at different axial locations

Figure 4.2.7 (a) shows the variation of bending frequency with axial location of delamination calculated using the FE model, which can be compared to figure 4.2.4. Overall, the results from the FE model agree well with the DSM. The worst agreement occurs for the fourth bending mode, where the DSM has underestimated the normalised fourth bending frequency slightly. This is because the delamination is a higher proportion of the wavelength of the 4th bending mode-shape, and the assumed constant shear force distribution becomes more inaccurate.

Even though the model used to calculate the torsional rigidity of the delaminated section is known to be inaccurate, the torsional behaviour is also compared with the FE results. When comparing torsion modes calculated by the DSM and by FE, which is shown in figure 4.2.7 (b), a similar pattern is also seen, but, as expected, the DSM predicts that the frequency reduction created by the reduced torsional rigidity is too large. The underestimation in the frequencies predicted by the DSM is most severe for the low order modes, and a better correlation is seen for higher order modes. The FE model does however agree with the DSM that the greatest effect on the torsional frequency is seen when the delamination lies in a region of high shear stress. This suggests that using a reduced torsional rigidity term is correct, but that the simple method outlined in Chapter 2 calculates a torsional rigidity parameter that is too low. This is probably due to the fact that in the simple analysis the end-face compatibility condition is violated, so that the torsional rigidity is

greatly underestimated. There is also the possibility that the thin rectangular cross-sections considered display considerable warping, which increases the effective stiffness of the laminates.

a)

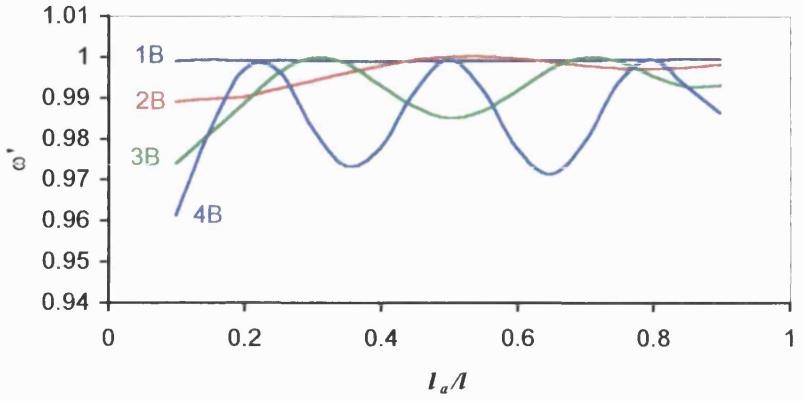

b)

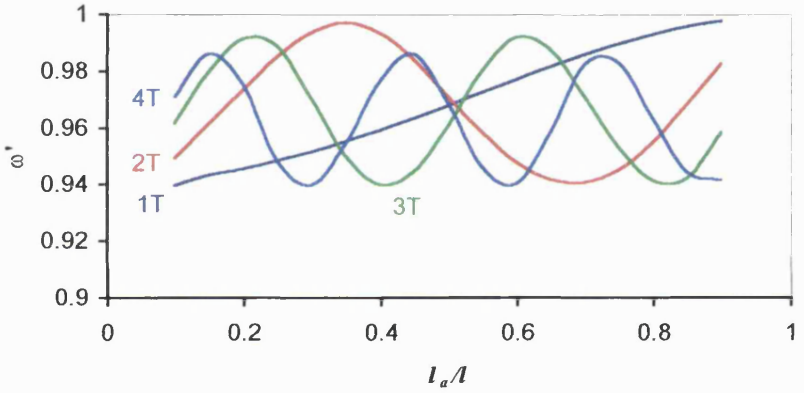

Figure 4.2.7 – Normalised frequencies for an aluminium beam with a delamination at different axial locations calculated by F.E

a) Bending frequencies

b) Torsional frequencies

Of course, a vibrating beam with a delamination is more complicated than either the static model and the DSM, or the FE model. Motion of the delaminated area would cause sub-laminates to come in contact with each other, causing friction and other non-linear effects, which has not been taken account of in the FE model. This effect is small for centre-line delaminations, as the overlapping of the two sub-laminates is small, but for thin delaminations near either surface of the laminate, the error is more significant (Mujumdar and Suryanarayan (1988)). This is normally overcome by assuming that the delamination creates a gap between the plies, so that the

overlapping is small. However, as described later in the thesis, even this simple model is capable of detecting delaminations, and has advantages over other possible more complicated models.

4.3 Effect of Delamination Size on the Dynamic Behaviour of Beams

Equation (2.3.9) defines the deflection of a cantilever beam with a single delamination, and equations (A23) and (A5) give the deflection for a cantilever with multiple delaminations. It can be seen from these equations that the deflection is proportional to the cube of the length of the delamination. However, the maximum deflection is used to define the effective shear rigidity of the delaminated laminate, which, as shown in equation (2.3.24), varies linearly with length. Therefore the assumption of (2.3.24) is effectively fitting a straight line through the curve defined by the difference in undelaminated and delaminated beams, as shown in figure 4.3.1. This means that the value of effective shear rigidity is proportional to the inverse of the square of the length of the delamination, converging on zero shear rigidity for an infinitely long delamination. The reduction in shear rigidity with delamination size, for a centreline delamination, is shown in figure 4.3.2 for a few example laminates. Because they are obtained from the static beam model, the results in this figure are independent of the location along the length of the beams.

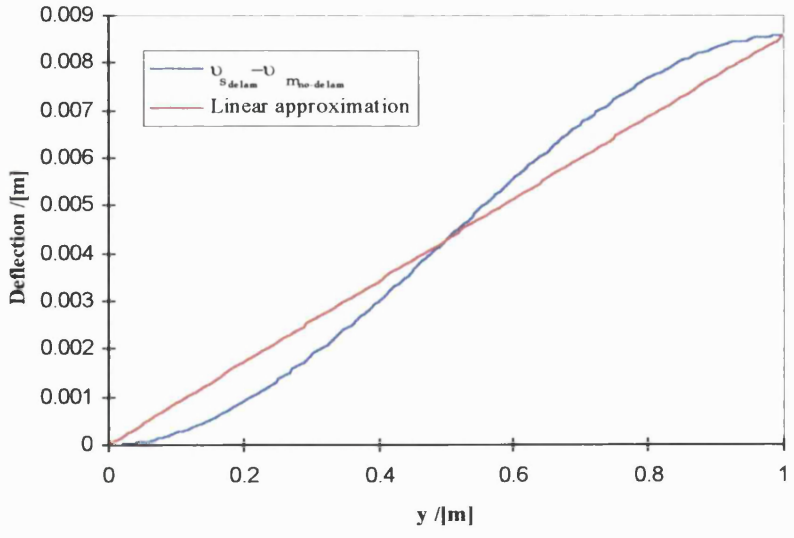

Figure 4.3.1 – Linear approximation of actual difference in deflection of delaminated and undelaminated beams, used to calculate shear rigidity

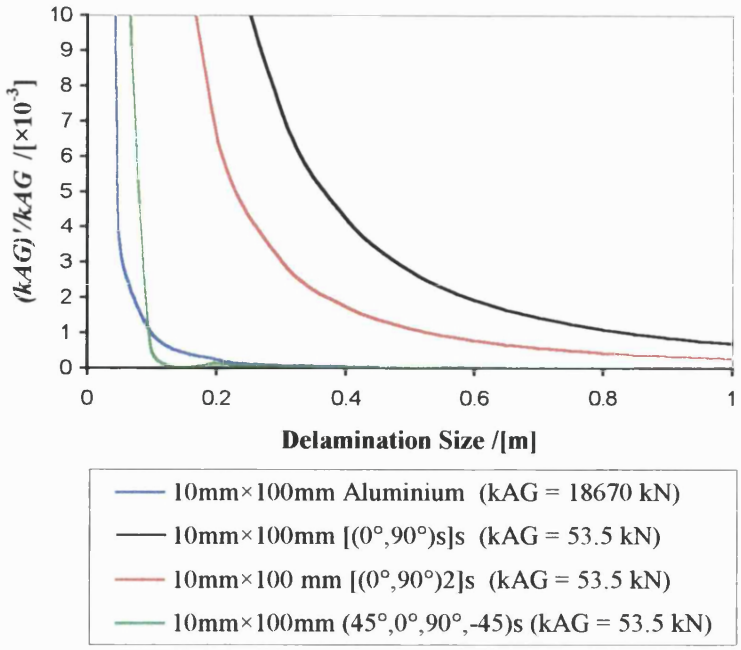

Figure 4.3.2 – Reduction in shear rigidity with delamination size

However, the DSM predicts that the bending frequencies of a cantilever beam are scarcely affected for small drops in shear rigidity. Figure 4.3.3 shows the drop in the first four bending frequencies with shear rigidity for the aluminium beam. It can be seen that it is not until the shear rigidity drops to almost a hundredth of its original value that an effect on the bending frequencies can be determined.

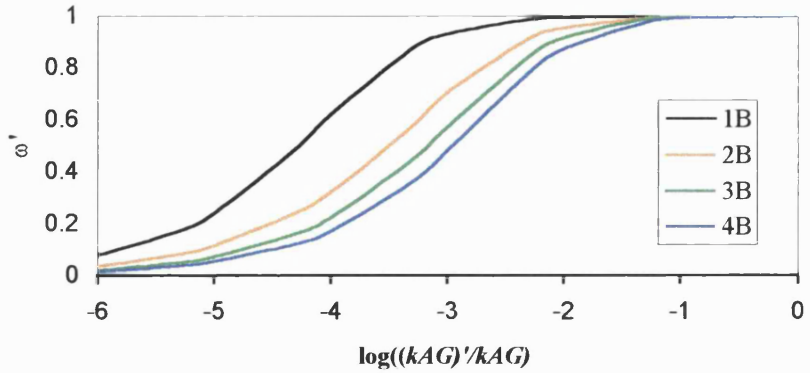

Figure 4.3.3 – Reduction in bending frequency with shear rigidity for a 1m aluminium cantilever beam

The effect of combining these two effects can be seen in figure 4.3.4, which shows the variation of bending frequencies with delamination length for a centre line delamination at the middle of a cantilever ($l_a = 0.5l$. See figure 4.2.1). These figures are in good agreement with Tracy and Pardoen (1989), for delamination lengths up to 25% of the beam (Okafor *et al.* (1995)), but as the delamination increases in size, the static beam model and DSM overestimates the drop in frequency. Also, as seen in the previous section, when the delamination enters into a region of high shear force for a particular mode, the effect of the delamination is increased.

The errors again occur because the approximation of a constant linear shear force distribution becomes more inaccurate as the length of the delamination increases compared to the wavelength of the bending modes. Comparing results from Okafor et al., at 0.75 of the beam length for a centreline delamination, the frequency ratios when divided by the undamaged frequencies are 0.84, 0.75, 0.68 and 0.69 for modes 1 to 4, respectively. (Note: Okafor presents results for a $[0°,90°]_{2,s}$ laminate, which has a different ratio of sub-laminate axial stiffness to overall bending rigidity than an isotropic beam. Using the ratio of the two stiffnesses and figure 5 in Tracy and Pardoen (1989), the bending frequencies are multiplied by 1, 1.01, 1.04 and 1.11 for modes 1 to 4, respectively.) This can be compared to figure 4.3.4, which gives 0.79 for mode 1, 0.50 for mode 2, 0.38 for mode 3 and 0.30 for mode 4. It can be clearly seen that for such a large delamination, the discrepancy in the model increases as the wavelength of the mode reduces.

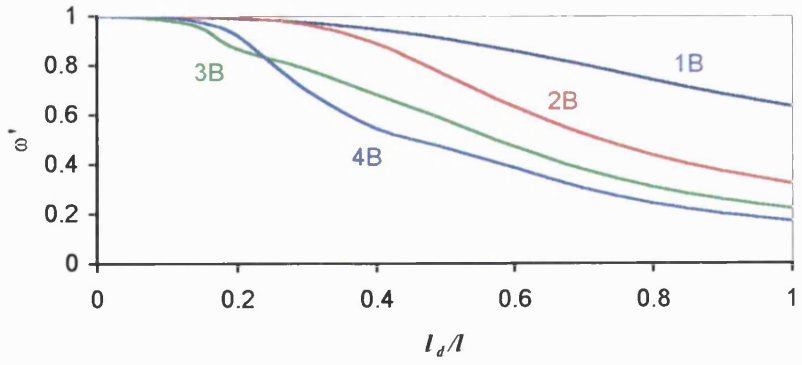

Figure 4.3.4 – Reduction in bending frequency with delamination size for a 1m aluminium cantilever beam

Figure 4.3.5 gives an indication of the accuracy of using the static beam model to predict a frequency drop via a reduction in shear rigidity. The finite element model was used to produce the

first four bending frequencies of the aluminium cantilever described in section 4.1.1. A centre line delamination was then introduced into the FE model at various sizes and positions, and new frequencies produced. Using a simple linear step algorithm and the DSM, the shear rigidity necessary to produce the frequencies obtained by the FE model was found.

It can be seen from figure 4.3.5 that the static beam model agrees with the FE model reasonably well, although again the accuracy reduces as the size of the delamination increases. However, since such large delaminations would be easily discovered by a visual inspection, it is more important that there is good accuracy at smaller delamination sizes.

In figure 4.3.5, the value of shear rigidity that best describes the frequency reduction predicted by the FE model, varies with the position of the delamination. Because the static beam model assumes a full-length delaminated cantilever beam, this effect is not predicted by the static beam model. This is because at certain positions along the beam the shear force distribution is not approximated well by a constant shear force.

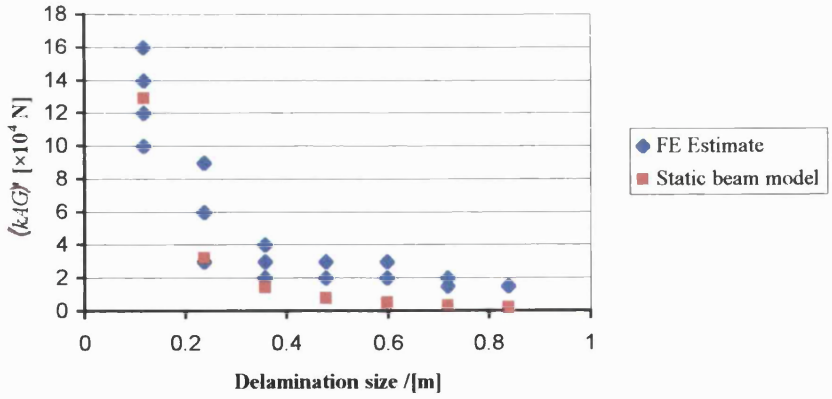

Figure 4.3.5 – Comparison of shear rigidity with delamination size calculated by FE (delaminations at different lengthwise positions) and by the static beam model

A similar investigation can be carried out for reductions in torsional frequency. Equation (B8) predicts that a value for the torsional rigidity of a delaminated laminate is simply the sum of the torsional rigidities of the individual sub-laminates, and does therefore not vary with the length of the delamination. The variation of torsional frequency with delamination size is shown in Figure 4.3.6, for the aluminium beam. Only the first and second torsional frequency can be ascertained

as the delamination increases to the full length of the beam, as only the first ten frequencies were calculated, and the bending frequencies soon drop below the higher order torsional frequencies. The dashed line indicates that the shear rigidity was artificially kept constant to allow the second torsional frequency to be calculated. Even though the torsional rigidity of the delaminated section is underestimated by the beam model, because the torsional rigidity remains unchanged as the delamination size increases, the drop in torsional frequency is less pronounced than for the bending frequencies.

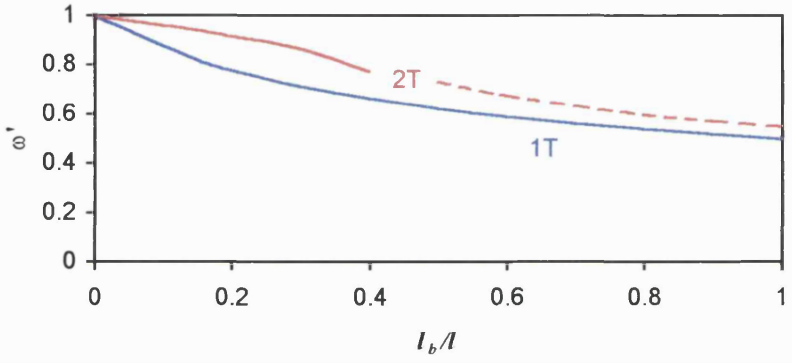

Figure 4.3.6 – Reduction in torsional frequency with delamination size for the 1m×0.1m×0.01m aluminium cantilever beam

These results mean that there are multiple combinations of delamination size and location that give the same or similar reductions in frequency for the different modes. For example, a delamination with $l_a/l = 0.1$ and $l_d/l = 0.1$, shown in figure 4.2.7 (a), has very similar bending frequencies as a delamination with $l_a/l = 0.5$ and $l_d/l = 0.145$, given in figure 4.3.4. Therefore, if only the bending frequencies were used to locate damage by optimisation, there would be two possible solutions. For this example, the torsional frequencies would be different for the two cases, but torsional frequencies were not used during the optimisation process due to the reasons outlined above. Also, including higher order modes would remedy this problem, but experimental data is often limited to lower order modes owing to equipment limitations.

The above problem is overcome by using the mode-shapes of the individual modes. The reduced rigidity of the delaminated area causes a steeper gradient to be seen for the same load, which differentiates between the two damage cases. Figure 4.3.7 shows this effect for the third bending

mode of the beam with a delamination of $l_a/l = 0.1$ and $l_d/l = 0.1$ shown in figure 4.2.7 (a), and with $l_a/l = 0.5$ and $l_d/l = 0.145$, given in figure 4.3.4. A difference in the mode shapes can be seen, which allows correct location of the damage during the optimisation process.

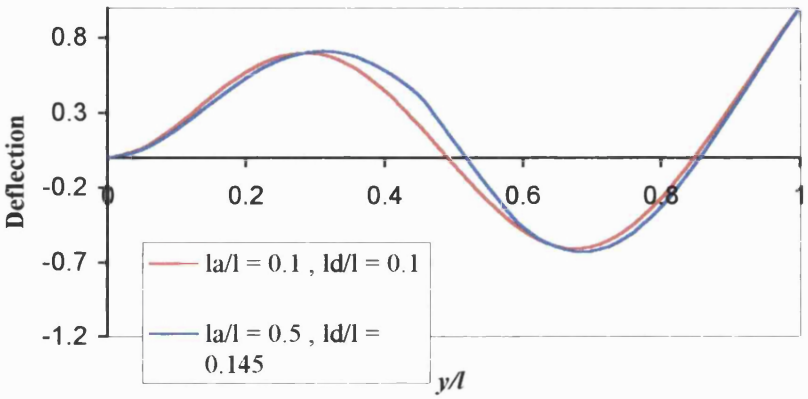

Figure 4.3.7 – Third bending mode for the 1m×0.1m×0.01m aluminium beam with a delamination in two locations

5. Experimental Procedure

The natural frequencies and mode-shapes of composite beams and plates, with and without delaminations, were measured experimentally. The results from these experiments were used to assess the accuracy of the analytical model, and to assess the validity of the damage detection methodology. Beams with two types of delamination were measured; "simulated" delaminations, where strips of Teflon-coated material were inserted between the layers during the manufacturing process, and actual delaminations caused by low velocity impact.

This chapter describes the manufacturing procedure and materials used, and describes the experimental procedure used to measure the frequencies and mode-shapes.

5.1 Description of the Experimental Beams

Thirteen laminates were tested experimentally. These can be divided into two sections; beams manufactured in-house, which were used to compare the experimental results of damaged beams by inserting simulated delaminations during manufacture, and beams manufactured by British Aerospace Airbus Ltd., where the damage was produced by a drop-weight test.

The first set of beams can be further sub-divided into beams with a $[0°,90°]_{2,s}$ laminate geometry, and identically sized beams with a $[0°,\pm45°,0°]_s$ laminate geometry. Similarly, the British Aerospace laminates can be further sub-divided, into a set with a uni-directional lay-up construction with dimensions of 350×250 mm, and one with a tri-axial weave construction, with dimensions of 550×250 mm. (These had various thicknesses, and are shown in table 5.1.3.)

This section describes the manufacture of these laminates.

5.1.1 Beams with Simulated Delaminations

Two sets of beams with different laminate geometries were manufactured using an in-house compression moulding manufacturing technique. During manufacture, strips of teflon-coated material were inserted between certain layers to produce a delamination of known area. Many researchers have used this technique to simulate delaminations. For example Shi and Hull (1991) used PTFE film embedded in a 24-ply laminate to initiate delamination growth under flexure.

Eight beams were manufactured with different laminate geometries and delamination locations. Three of these beams were manufactured and tested as part of a final year research project at the University of Bath (Cox (1999)). The remaining five were manufactured by the author. When the manufacturing technique and measurement procedures are described within this chapter, they refer to the work carried out by the author, unless otherwise indicated. However, the manufacturing techniques and experimental procedures given by Cox (1999) are similar.

A carbon fibre/epoxy pre-impregnated unidirectional fibre sheet was used (Hexcel Composites Ltd. Fiberdux T300/913C). The material properties for the cured carbon-fibre material with a 60% fibre volume fraction are given in table 5.1.1. Note that where no material properties were available from the manufacturer's data, values have either been calculated or assumed. Also, the density of the material was measured after manufacture, and considerable difference between the manufacturer's data and the measured values was noted. The measured value for density was therefore used for all post-characterised numerical analyses, as described in Chapter 7.

$E_1 = 138.0\times10^9$ Pa	$\nu_{12} = 0.263$	$G_{12} = 1.07\times10^9$ Pa
$E_2 = 9.65\times10^9$ Pa	$\nu_{23} = 0.263$	$G_{13} = 1.07\times10^9$ Pa *
$E_3 = 9.65\times10^9$ Pa *	$\nu_{31} = 0.018$ †	$G_{23} = 5.38\times10^8$ Pa ‡
$\rho = 1787.0$ kg/m^3	$\rho_{measured} = 1645$ kg/m^3	$t_{ply} = 0.125$ mm *

* - Assumed value

† - Calculated value: $\nu_{31} = \nu_{13}\frac{E_3}{E_1} = \nu_{12}\frac{E_3}{E_1}$

‡ - Assumed value: $G_{23} = \frac{G_{13}}{2}$

Table 5.1.1 - Material properties of T300/913C Carbon-fibre/epoxy laminates

The compression moulding technique was:

- Apply 2000 kN/m² pressure
- Heat to 80°C for 90 minutes, or heat to 150°C for 20 minutes
- Remove from press whilst still hot, and cool at room temperature for 24 hours

The manufacturing process created a plate 450 × 300 mm, from which 400 × 50 mm beams were cut. All beams had a nominal thickness of 1mm. During manufacture, two strips of Teflon material were inserted between the layers of carbon-fibre at each desired delamination position. In each case, the delaminations were 50 × 50 mm, and had a nominal thickness of 0.05 mm. A representation of a beam with a simulated delamination is given in figure 5.1.1, where l_{clamp} is the length of the beam that was clamped during the experiments, and was 0.1m.

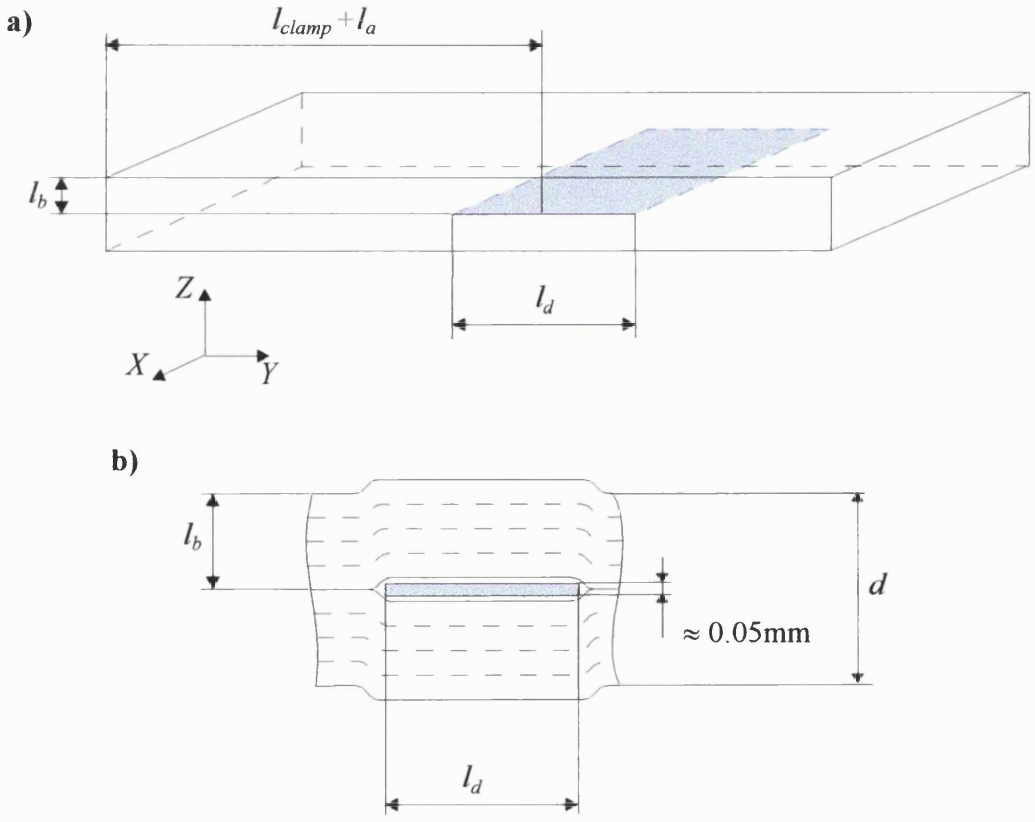

Figure 5.1.1 - Beam with simulated delamination.

a) Whole beam showing the location of the delamination. Note: $l_{clamp}+l_a$ is the distance from Y=0 to the centre of the delamination

b) Detail of the simulated delamination.

The two lay-ups chosen were $[0°,90°]_{2,s}$, described by Cox (1999), and $[0°,\pm45°,0°]_s$, which, together with the position of the delaminations in each case, are given in table 5.1.2.

Because the maximum length of the beams was limited by the manufacturing process, beams with dimensions of 400 × 50 mm with a $[0°,90°]_{2,s}$ lay-up were chosen, so that when supported as a cantilever the first four bending modes of vibration were expected to lie within the range of the experimental equipment. Using the equations in chapter 2, the stiffness properties of the undelaminated section were calculated to be:

$$EI = 0.4136\ \text{Nm}^2\ ;\ GJ = 0.01783\ \text{Nm}^2\ ;\ K_{BT} = 0.0\ \text{Nm}^2\ ;\ kAG = 2.675\times10^4\ \text{N}$$

It can be seen that the beams are very flexible in torsion when compared to the bending rigidity, and this subsequently led to problems with the experimental results (outlined in chapters 6 and 7).

The second set of beams (Cases 4 - 8 in table 5.1.2) were designed to remedy this, by including ±45° layers to increase the torsional rigidity. For continuity, the length, width and thickness of the beams were chosen to be the same as the first set of beams. The stiffness properties of the undelaminated section were calculated to be:

$$EI = 0.3610\ \text{Nm}^2\ ;\ GJ = 0.2255\ \text{Nm}^2\ ;\ K_{BT} = 0.01\ \text{Nm}^2\ ;\ kAG = 3.121\times10^4\ \text{N}$$

This meant that the DSM predicted that the first four bending modes remained within the range specified by the experiment, and also included four well-spaced torsion modes for analysis. The experimental and analytical frequencies and mode-shapes are given in Chapter 6.

As explained in Chapter 4, when a delamination is located in a region of high shear force for a particular mode, a larger effect on the frequencies and mode-shapes is expected. Cases 2 and 5 are located in a position of high shear force for the third bending modes, and a large drop in frequencies was expected for this mode. Similarly, with the knowledge of the expected bending mode-shapes, it was expected that cases 3 and 6 would have a greater effect of the fourth bending modes, and cases 7 and 8 would affect second to fourth bending modes. It was also expected that, because the delamination was located closer to the surface for case 8, a smaller effect of frequencies and mode-shapes would be seen than for case 7.

It was also expected from Chapter 4 that the delamination would have a greater effect on the torsional modes of vibration. For cases 2 and 5, it was expected that the delamination would have the greatest effect for the first torsion mode, with a smaller but significant effect on the second to fourth modes. For cases 3 and 6, it was expected that the first and second torsion modes would be affected the most, with a lesser effect being expected for the third and fourth modes. Again, because the delamination was located nearer the surface, it was expected that case 8 would have a smaller effect than for case 7.

Test Case Number	Lay-Up	$l_{clamp}+l_a$ [mm]	l_d [mm]	l_b [mm]
1	$[0°,90°]_{2,s}$	-	-	-
2	$[0°,90°]_{2,s}$	247	50	0.5
3	$[0°,90°]_{2,s}$	286	50	0.5
4	$[0°,\pm45°,0°]_s$	-	-	-
5	$[0°,\pm45°,0°]_s$	247	50	0.5
6	$[0°,\pm45°,0°]_s$	286	50	0.5
7	$[0°,\pm45°,0°]_s$	135	50	0.5
8	$[0°,\pm45°,0°]_s$	135	50	0.25

Table 5.1.2 - Laminate geometry and position of delamination for the beams with simulated delaminations (Note: Ply thickness = 0.125 mm)

5.1.2 Plates with Delaminations produced by Low-Velocity Impact

Experimental tests were also carried out on plates supplied by British Aerospace Airbus. Two types of plate were investigated, which used different types of laminate geometry and plate dimensions. A summary of the plates is given in table 5.1.3.

Cases 9 - 11 were made up of Uni-Directional (UD) layers of HTA-12k/977-2 carbon-fibre/epoxy material. Cases 12 and 13 were made from Non-Crimp Fabric (NCF) blankets of T300/914 carbon-fibre/epoxy. The material properties for one ply of T300/914 are given in table 5.1.4. No material properties of HTA-12k/977-2 were available. However, it was assumed that,

since the fibres were identical for both materials and the material properties are dominated by the fibre properties, the material properties were similar to those given in table 5.1.4.

To determine the ply thickness, t_{ply}, used in the analytical modelling and optimisation, the average thickness of the laminates given in table 5.1.3 was divided by the number of plies in the laminate.

Test Case Number	Dimensions [mm]	Lay-Up	Unit Ply Geometry
9	375×250×4	$[(+45°,-45°,0°,90°)_2]_s$	UD
10	375×250×8.1	$[(+45°,-45°,0°,90°)_4]_s$	UD
11	375×250×8.2	$(+45°_4,-45°_4,0°_4,90°_4)_s$	UD
12	550×250×3.1	$[(+45°,-45°,0°)_s]_2$	NCF
13	550×250×6.8	$[(+45°,-45°,0°)_s]_4$	NCF

Table 5.1.3 - Laminate geometry of the low-velocity impact damaged plates. (UD - Uni-Directional, NCF - Non-Crimp Fabric)

Each NCF blanket is made up of a triaxial weave of fibres, consisting of units with either a (-45°,+45°,0°) or (+45°,-45°,0°) lay-up, stitched together with polyester yarn. A laminate is then made up of a combination of these units. A description of the plate manufacture is given by Ball and Almond (1998), and a general review of this type of stitched laminate construction is given by Mouritz *et al.* (1997). This type of construction results in a laminate with a higher interlaminar shear strength, but can reduce the in-plane properties due to damage caused by stitching. The NCF construction also gave a slightly greater thickness per layer laminate than the UD laminates. However, for the purposes of the validation of the analytical model, the fact that the laminates were made up of NCF blankets was ignored.

$E_1 = 121.9\times10^9$ Pa	$\nu_{12} = 0.3$	$G_{12} = 4.875\times10^9$ Pa
$E_2 = 9.25\times10^9$ Pa	$\nu_{23} = 0.3$	$G_{13} = 4.875\times10^9$ Pa
$E_3 = 9.25\times10^9$ Pa	$\nu_{31} = 0.023$	$G_{23} = 3.558\times10^9$ Pa
$\rho = 1498.0$ - 1679.0 kg/m^3		

Table 5.1.4 - Material properties of T300/914C Carbon-fibre/epoxy laminates

The delaminations were produced using a Rosand Instrumented Falling Weight Impact Tester (Type 5). This was carried out for British Aerospace Airbus at Cranfield University. For this procedure, the plates were clamped below an adjustable weight. The plates were supported along each edge, and held in place using four clamps. A 16 mm hemispherical diameter striker was connected to the weight, and was then dropped onto the plate. By adjusting the mass above the striker, different impact energies were made possible, whilst the velocity of the impactor was kept at ≈2.2 m/s. After impact, the striker was held to ensure the plate was not repeatedly impacted. The energy transferred to the plate was recorded using a force transducer attached to the striker. Laminates number 9 and 12 were impacted with approximately 15 J, and laminates 10, 11 and 13 with approximately 30 J. A similar procedure is described by Ball and Almond (1998), where the delaminations are subsequently located using a transient thermography technique.

The plates were later examined using a double through transmission ultrasonic C-scan method. Figure 5.1.2 gives the C-scan images of the delaminated plates. In these images, the white area indicates the maximum area of the delamination. The delamination may extend over more than one ply interface, but it is not possible from these images to determine at which interface the delaminations occur.

On the front surface of the laminates, only small indentations were evident where the striker had impacted. However, some damage could be seen on the back surface of the laminates. In some cases the surface was raised slightly by the delamination, and in other cases there was some splitting of the plies in the direction of the fibres. For case 13, some fibre-breakage was also evident. In general, the delaminations were seen to be most extensive in the direction of the fibres at the back surface of the laminates, so that the delaminations appeared to run in a 45° direction. However, inspection of the C-scan images only verified this for cases 9 and 11. It can be seen from these images that the largest delamination had an area of 5650 mm^2, which corresponds to 32% of the width and 24.6% of the length of the undelaminated laminate.

a)

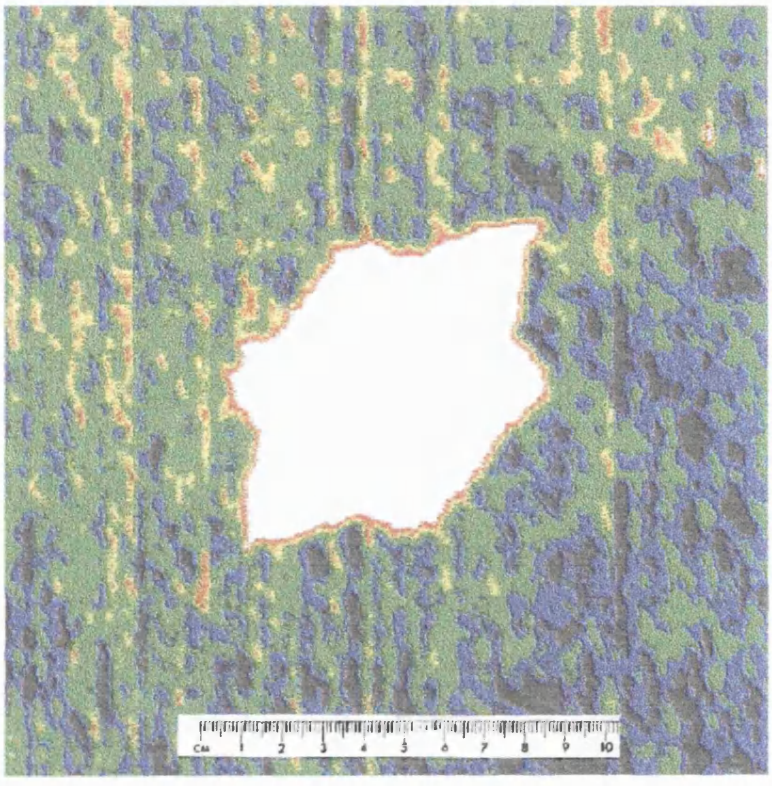

b)

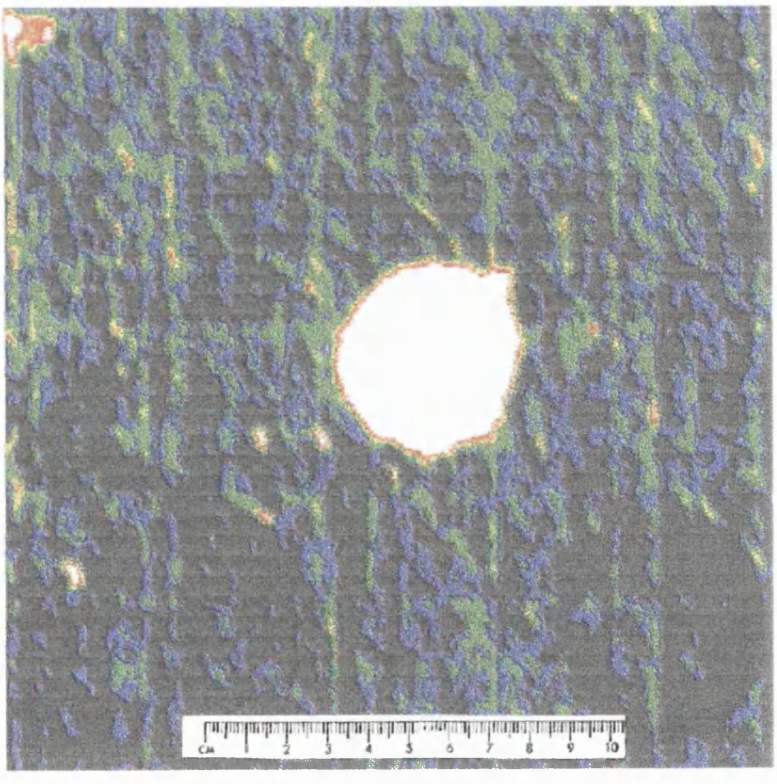

c)

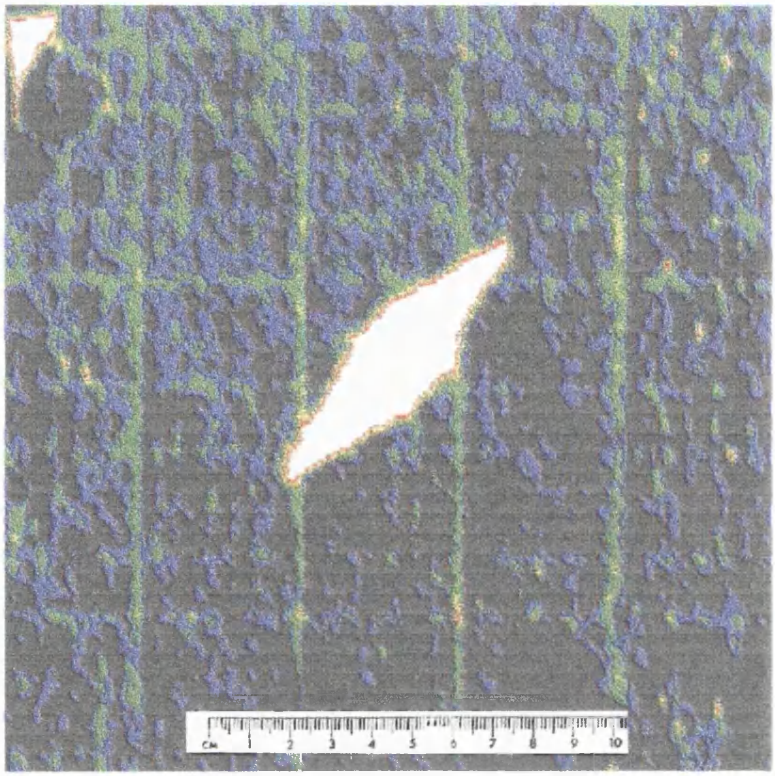

d)

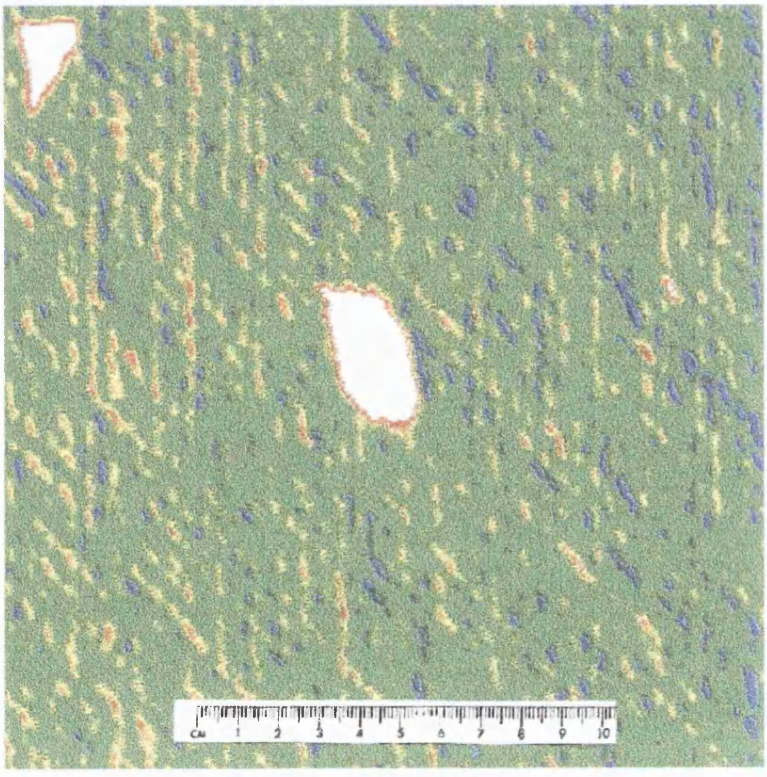

e)

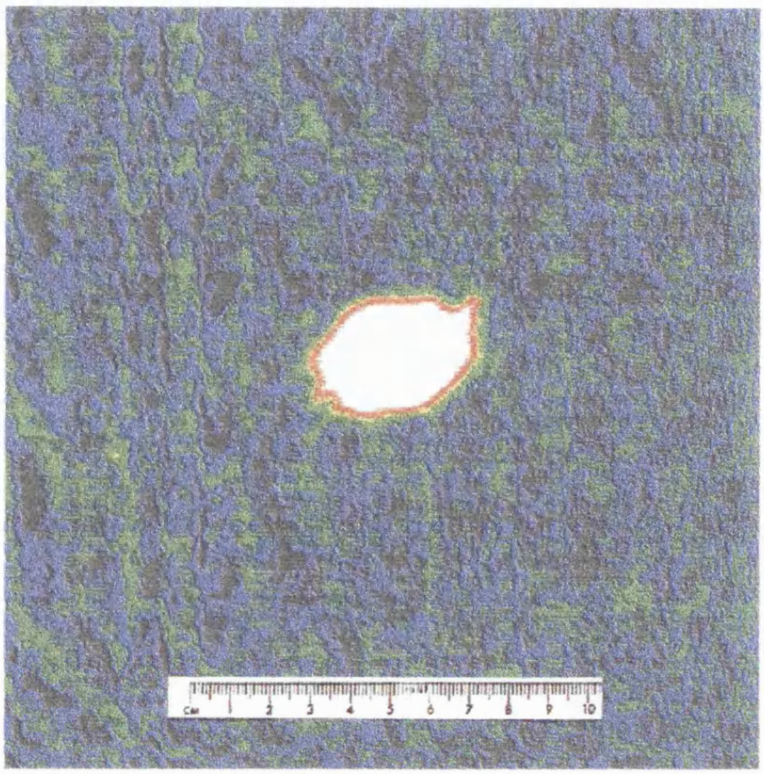

Figure 5.1.2 – C-scans of the carbon-fibre plates with impact damage (Courtesy of British Aerospace Airbus Ltd.)

a) $[(+45°,-45°,0°,90°)_2]_s$ UD laminate (Case 9)

b) $[(+45°,-45°,0°,90°)_4]_s$ UD laminate (Case 10)

c) $(+45°_4,-45°_4,0°_4,90°_4)_s$ UD laminate (Case 11)

d) $[(+45°,-45°,0°)_s]_2$ NCF laminate (Case 12)

e) $[(+45°,-45°,0°)_s]_4$ NCF laminate (Case 13)

5.2 Experimental Modal Analysis

Modal analysis was performed on the laminates in order to verify the frequencies and mode-shapes produced by the analysis, and to generate data to test the damage detection methodology. Modal analysis involves exciting the structure with a known, frequency dependent force, and measuring the resultant vibration. A frequency analyser then produces the Frequency Response Function (FRF) in the form of accelerance, $H(\omega)$, for the structure (Ewins (1984)):

$$H(\omega) = \frac{a(\omega)}{f(\omega)} \qquad \ldots (5.2.1)$$

where a is the measured acceleration in the frequency domain, and f is the measured force in the frequency domain. $H(\omega)$ is a complex function which contains both real and imaginary terms, and which can be presented in terms of gain and phase information. The frequency response of any point in a structure can be described by the reciprocal theorem for dynamic loads, i.e. the response of a point i to a force at point j is equivalent to the response at point j due to the same force at point i. In order to obtain mode-shapes for the structure, a FRF must be obtained for many points on the structure. Because the reciprocal theorem applies, this can be carried out with an accelerometer fixed at one position, by applying a measured force at different points in turn. This is sometimes referred to as a modal survey.

Each beam was clamped at the root to a steel table to create a cantilever. For the beams with simulated delaminations, the first 0.1m of the beams (l_{clamp} = 0.1m) were clamped between two steel plates using four bolts. The steel plates were then secured to the steel table using a G-clamp. The clamping arrangement and a diagram of the experimental equipment is shown in figure 5.2.1.

The impact damaged plates were secured directly to the steel table using a steel block and G-clamps. In order to keep the aspect ratio of the plates acceptable (in order to reduce anticlastic bending to a minimum), only the first 0.05 m of the plates were clamped to the steel table.

By removing and re-clamping the test specimens, a measure of the errors inherent in the clamping mechanisms was assessed. The results of this test are given in Chapter 6.

An accelerometer with a frequency range of 0-600 Hz (Entran Ltd. EGA-125-50D) was attached to one point of the beam with wax, after ensuring that the accelerometer did not lie on a nodal

point of any of the modes. This measured acceleration in the Z direction. The beams were excited with an impact hammer at different excitation points. Each point was excited three times, and an average taken. The vertical impact force was measured with a force transducer (Brüel & Kjær B&K 8200), and this force signal was used to trigger the recording of the data. The data was recorded using a Data Physics Corporation SignalCalc Ace frequency analyser (Data Physics Corporation (1999)).

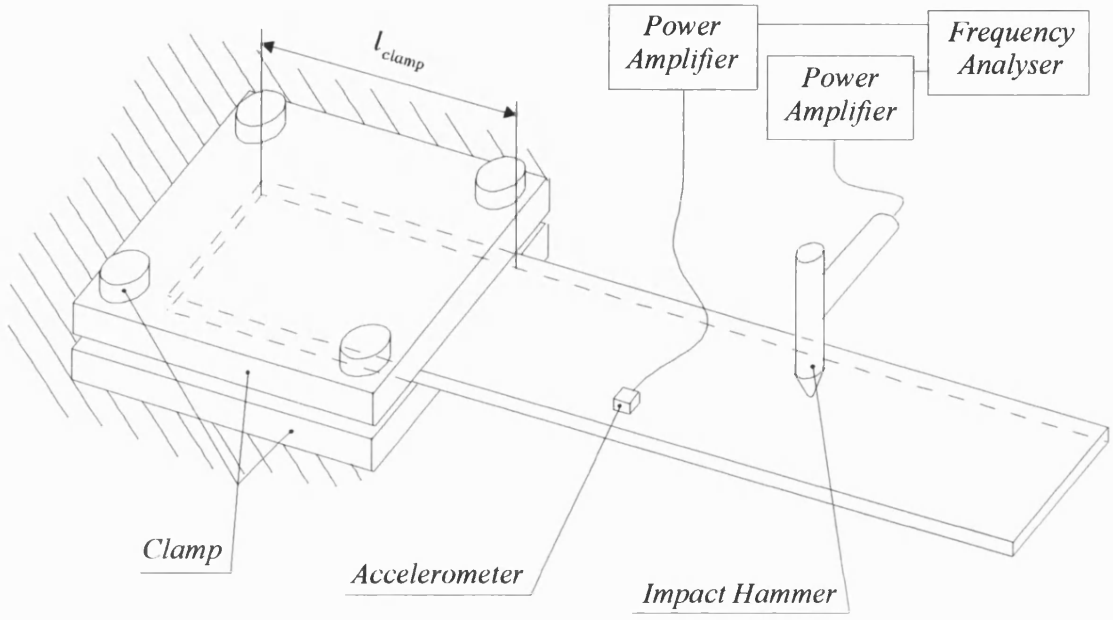

Figure 5.2.1 - Schematic arrangement of experimental beams with simulated delaminations

By attaching the accelerometer to the steel table, a simple test was carried out to ascertain that the natural frequencies of the support laid outside the range of the experiment and would not therefore influence the results.

For cases 1 to 3 of the beams with simulated delaminations, described by Cox (1999), the beam had nine excitation points along the Y-axis, which were used to determine the bending mode-shapes, and six points offset by 12.5mm from the Y-axis. These were used to determine the torsional mode-shapes. It was later determined that this produced mode-shapes with insufficient resolution for the damage detection methodology, and the number of impact measurement points was increased for cases 4 to 8. For these cases, the number of impact points was increased to eighteen points along the Y-axis, and eighteen offset from the Y-axis by 12.5 mm. The impact

points and accelerometer positions for these cases are shown in figure 5.2.2. For the plates with low-velocity impact damage, test cases 9 to 11 had forty-five points, spaced equally in the *Y* and *X* directions, and cases 12 and 13 had ninety-eight equally spaced points. The impact points and accelerometer positions for the impacted plates are shown in figure 5.2.3.

Once an FRF was obtained for each point, the commercially available package Star System (Spectral Dynamics Inc. (1994)) used a curve fitting process to determine the frequency and peak amplitude for each of the nodes. A polynomial curve-fit method was used in this process. This determined the vertical amplitude (which was normalised to the maximum displacement of the nodes), the phase and the natural frequency of motion. Using the gain and phase information for each of the nodes, an animation could then be produced for each natural frequency, from which it is possible to ascertain the type of mode being displayed.

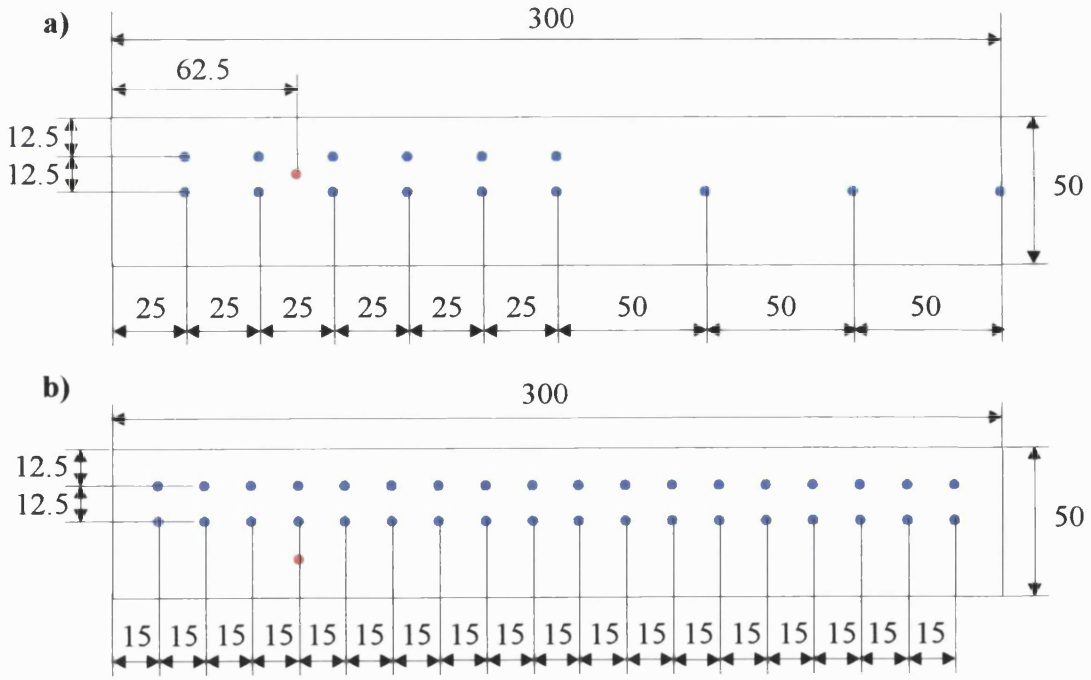

Figure 5.2.2 - Impact points (blue) and accelerometer positions (red) for the beams with simulated delaminations (All dimensions in mm)

a) Cases 1 - 3

b) Cases 4 - 8

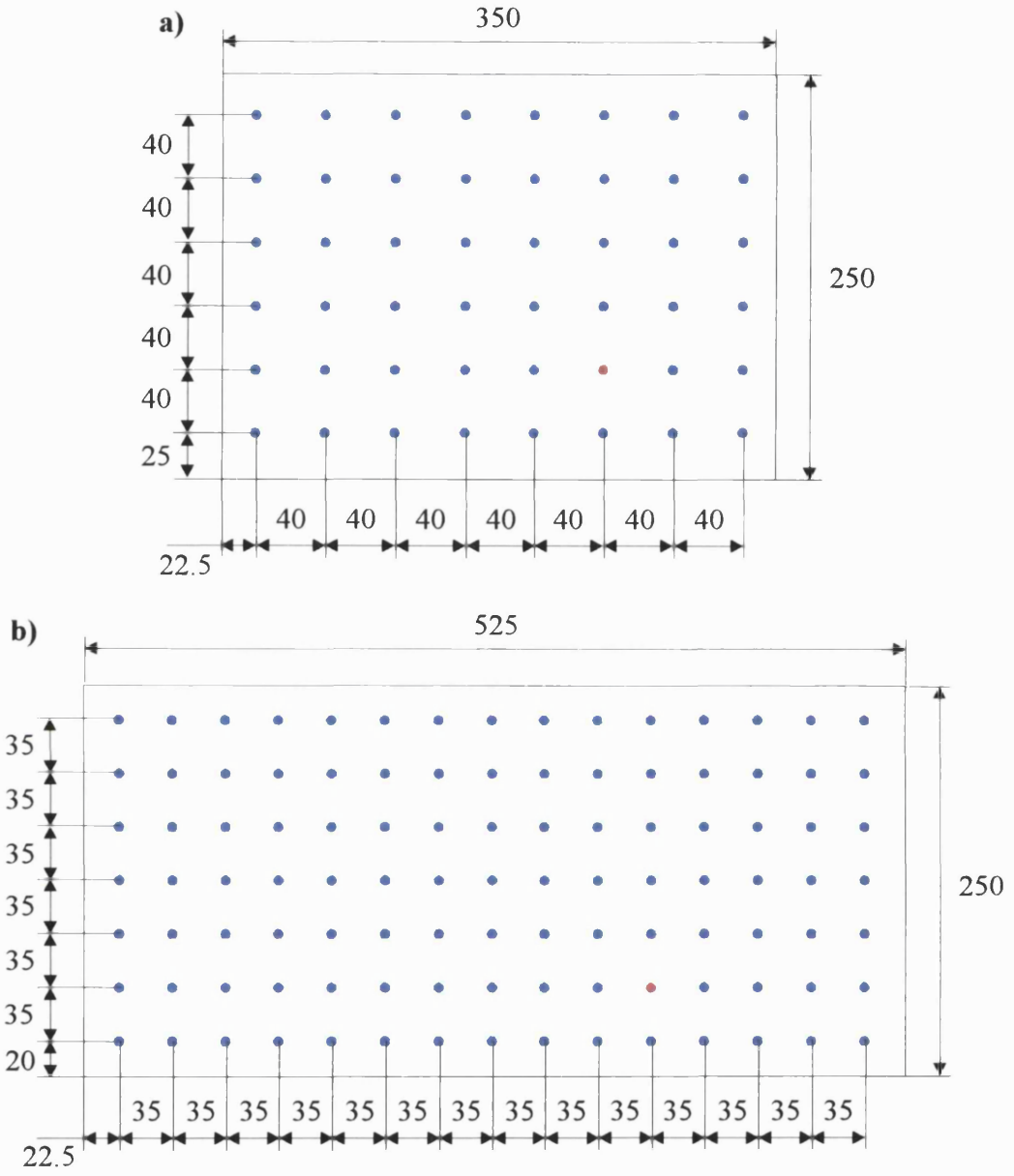

Figure 5.2.3 - Impact points (blue) and accelerometer positions (red) for the impacted beams (All dimensions in mm)

a) Cases 9 - 11

b) Cases 12 and 13

6. Experimental Validation

In Chapter 5 a description of the experimental beams, and the procedure used to obtain experimental results, was given. In this chapter the results obtained by these experiments are presented, and compared to the results obtained by numerical analysis. This gives an indication of the accuracy of the DSM in calculating the frequencies and mode-shapes of the laminates studied, as well as indicating the accuracy of the theoretical assumptions made when calculating the reduced rigidity of the delaminated beams.

6.1 Experimental Results of Undamaged and Damaged Laminates

This section presents the experimental results for both the damaged and undamaged laminates, and compares the results with theoretical predictions.

In section 6.1.1 the results obtained for the beams manufactured at the University of Bath are presented. The results for the beams with "simulated" delaminations are compared to undamaged beam results, by comparing the difference in natural frequency and the difference in the modeshapes, via the Modal Assurance Criterion (MAC). An assessment of the experimental error is made, and comments are made as to whether the results agree with the theory presented in Chapter 2. In section 6.1.2 this is carried out for the plates which had delaminations produced by impact.

Section 6.2 then compares experimental results to the results obtained via the DSM. In section 6.2.1 this is carried out for the beams manufactured in-house, some of which had "simulated" delaminations, and in section 6.2.2 for the plates with impact damage.

6.1.1 Beams with Simulated Delaminations

Table 5.1.2 shows the location and extent of the simulated damage covered in the experiment. For each beam, frequencies and mode-shapes were obtained from five tests. For cases 1 to 3, as the dimensions and lay-up were designed with bending frequencies only in mind, values for the torsional frequencies were obtained only once in each case.

When discussing the experimental results, it is assumed that a mode with predominantly vertical motion along the Y-axis (see figure 2.1.1), or predominately rotational motion about a line parallel to the X-axis offset along the Y-axis, is a "bending mode". A mode with predominantly rotational motion about the Y-axis is a "torsion mode". When neither type of motion appears to dominate the other, the mode is called a "mixed mode". This definition is necessary as a consequence of the experimental procedure, when absolute values for vertical displacement of nodes, or rotation of nodal lines is not available. Therefore a more strict definition like the one used in the numerical analyses is not possible.

Because of the amount of data collected, for convenience the experimental natural frequencies for the beams are given in Appendix C. Table C1 shows the experimental natural frequencies for the undamaged $[0°,90°]_{2,s}$ laminate (Case 1), which can be compared to the natural frequencies for the two damaged cases of the same laminate (Tables C2 and C3 for cases 2 and 3, respectively). Because of the low torsional stiffness of the beams, some difficulty was encountered when distinguishing the peaks of the torsional modes, and only four torsional modes could be determined. The results for these cases are presented by Cox (1999), but because results for only two of the five tests are given, the full results are presented here.

From inspection of the frequencies in tables C1 to C3, it can be seen that the variation in frequencies, given by the standard deviation, is quite low. The standard deviations of the mean values, defined in Appendix C, remained in all cases under 3% of the mean value.

Tables C4 to C8 show the equivalent experimental results for the $[0°,\pm45°,0°]_s$ laminates (Cases 4 to 8). In this case, results for both the first four bending modes and the first three torsional modes have been obtained from five tests. Again the variation in frequencies was reasonable, with the standard deviation remaining under 2% of the mean value in all cases.

Figure 6.1.1 shows the FRF for cases 4 to 8 (Point 21 of test 1 of each case), from which it is also possible to determine the frequency drop. This is typical of the quality of results seen during the experiments. It should be noted that figure 6.1.1 displays the FRFs within a frequency range of 0-1000 Hz. However, the accelerometer used had only an acceptable error when measuring frequencies under 600 Hz, and any modal peaks occurring over 600 Hz were ignored.

It can also be seen from these measurements that the beams were only lightly damped. The quality factor Q, which is outlined in many vibration textbooks, gives a measure of the damping

of the system, and hence how well defined the peaks of the FRF were. For the accelerance FRF $H(\omega)$, the quality factor is defined as the natural frequency ω_0, divided by the width of the response curve at the half power points $\Delta\omega$:

$$Q = \frac{\omega_0}{\Delta\omega} \qquad \ldots (6.1.1)$$

The half power points are the points on the curve where:

$$|H(\omega)|^2 = \frac{1}{2}|H(\omega_0)|^2 \qquad \ldots (6.1.2)$$

For all but the first bending modes, the quality factor ranged from 20.6 to 232.8. For the first bending modes, the quality factor ranged from 2.2 to 23.2. Hence the FRF for most experimental results was deemed acceptable, with a slight inaccuracy expected for the first bending modes.

Figure 6.1.1 also highlights the problems inherent when a low frequency mode is found using a high frequency range. In the region of the peaks due to the first bending mode, significant noise is evident. This leads to inaccurate curve fitting of the peaks, which in turn leads to inaccurate mode shapes. This can be remedied by including more lines of measurement in the desired frequency range, known as "zooming". This was however not carried out, and instead a low confidence factor was employed for the first bending mode frequencies during the optimisation. This is described in chapter 7.

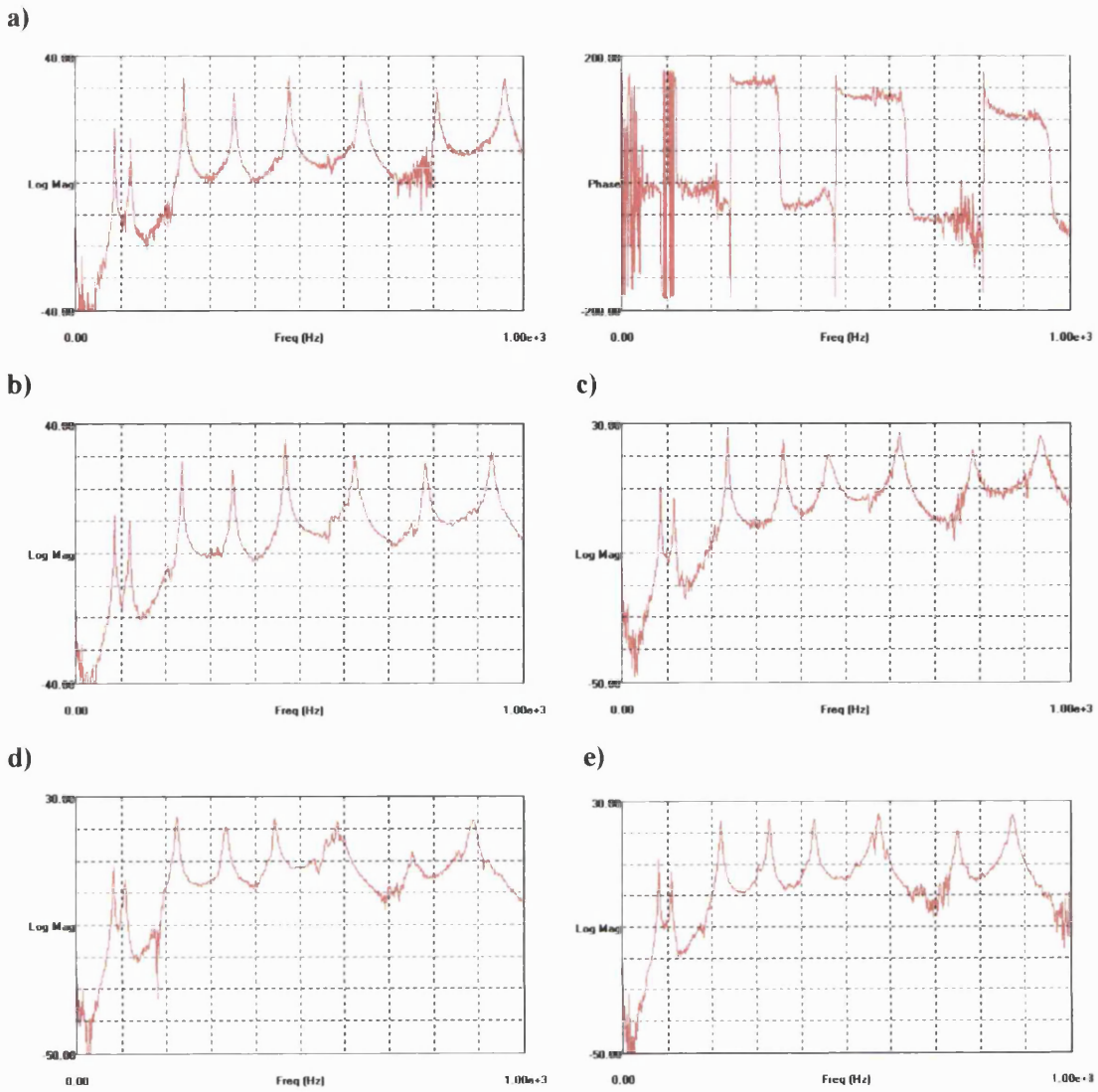

Figure 6.1.1 - Frequency response functions for the $[0^o,\pm45^o,0^o]_s$ beams

a) Gain and Phase results for the undamaged laminate (Case 4)

b) Gain results for the Case 5 delaminated beam

c) Gain results for the Case 6 delaminated beam

d) Gain results for the Case 7 delaminated beam

e) Gain results for the Case 8 delaminated beam

A useful way of comparing mode-shapes is the Modal Assurance Criterion (MAC), which is a scalar quantity. When comparing a mode-shape i with mode-shape j (Ting (1993)) the MAC is defined as:

$$MAC = \frac{\left(\phi_i^T \phi_j\right)^2}{\left(\phi_i^T \phi_i\right)\left(\phi_j^T \phi_j\right)} \qquad \ldots (6.1.3)$$

where ϕ_i and ϕ_j are the mode-shapes of mode i and j, respectively, and the superscript T denotes vector transposition. A MAC of 1 denotes a perfect correlation between two mode-shapes, whereas a MAC of 0 signifies no correlation. It is generally found that, when comparing experimental and analytical mode-shapes, MAC>0.9 is a good correlation, and MAC<0.05 signifies two uncorrelated modes (Ewins (1984)).

In this thesis, the MAC is used to compare experimental modeshapes, modeshapes produced by numerical analysis, and experimental modeshapes with ones produced by analysis.

Table 6.1.1 shows the average of the experimental bending frequencies for cases 2 and 3 normalised with respect to the average undelaminated frequencies, and the MAC for each mode when compared to the equivalent undelaminated mode-shapes. When comparing mode-shapes using the MAC, the modal vector used is the average displacement of the five tests. A delamination can be highlighted using this table by a low value of normalised frequency, showing that the frequency has dropped for the delaminated beam, and by a low MAC, showing that the delamination has significantly affected the mode-shape.

As expected, the largest drops in frequency occur for third bending and fourth bending modes for cases 2 and 3, respectively. MAC values for these modes also show a lower correlation, indicating that their mode-shapes are significantly different. The 8% drop in frequency for the first bending mode was unexpected, and can be put down to the higher measurement error encountered for this mode.

Figure 6.1.2 compares the third bending mode for cases 1 and 2, and the fourth bending mode for cases 1 and 3. Although because of the low number of test points the resolution of the mode-shapes is poor, these comparisons do show the characteristic features seen in the numerical

analyses. As explained in Chapter 4, both an increased gradient at the delamination location, and the shift in maximum peak location, is evident.

	Case 2		Case 3	
Mode	ω'	MAC	ω'	MAC
1B	0.92	0.98	0.97	0.97
2B	0.95	1.00	0.99	0.99
3B	0.85	0.92	0.96	0.99
4B	0.95	0.98	0.85	0.83

Table 6.1.1 - Normalised bending frequencies and MACs compared to the undelaminated (Case 1) mode-shapes for cases 2 and 3

The average frequencies for cases 5 to 8, normalised with respect to the undelaminated frequencies, and the MAC for each mode when compared to the equivalent undelaminated mode, are presented in table 6.1.2.

Comparing the bending frequencies for the four delaminated cases, it can be seen that the expected large frequency drops did not occur. It was expected from the position of the delaminations that for case 5, a large drop would occur for the third bending mode, whereas the frequency reduced by only 1%. For case 6, a larger drop was expected for mode 4, and this did occur, but was only 3%. For cases 7 and 8, a significant frequency drop was expected for modes 2, 3 and 4, and this was seen in the experiment, although there is a greater frequency drop for case 8, when the delamination in case 7 was expected to show a greater effect.

The torsion modes show greater drops in frequency than the bending modes, with the greatest drop in frequency evident for the third torsion modes. The third torsion modes however, suffer from greater experimental error due to the frequency being close to the accelerometer acceptable range in frequency. This can be seen when comparing the modes-shapes for the third torsion modes (Figures 6.1.3 to 6.1.6), which show significant error.

a)

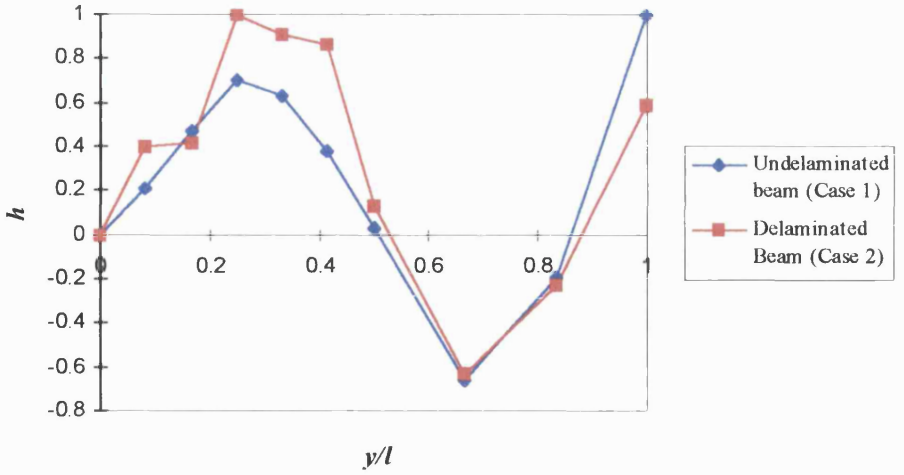

b)

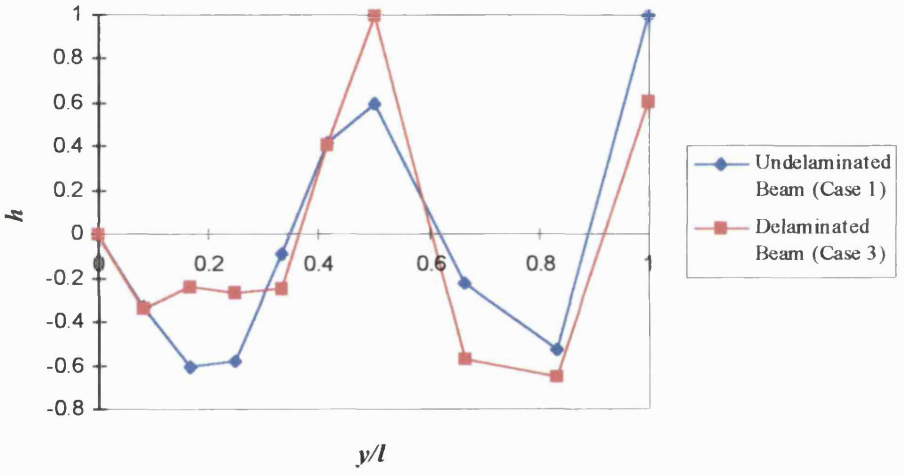

Figure 6.1.2 - Bending mode-shape comparison for delaminated and undelaminated $[0^o,90^o]_{2,s}$ beams

a) Third bending of cases 1 and 2

b) Fourth bending mode of cases 1 and 3

	Case 5		Case 6	
Mode	ω'	**MAC**	ω'	**MAC**
1B	1.00	0.88	0.96	0.98
2B	0.99	1.00	0.99	0.99
3B	0.99	0.99	0.99	0.98
4B	0.98	1.00	0.97	0.97
1T	0.97	1.00	0.94	1.00
2T	0.99	0.99	1.01	0.99
3T	0.97	0.89	0.98	0.90

	Case 7		Case 8	
Mode	ω'	**MAC**	ω'	**MAC**
1B	0.97	0.98	0.97	0.99
2B	0.95	1.00	0.93	0.98
3B	0.93	0.99	0.91	0.99
4B	0.92	0.97	0.89	0.98
1T	0.88	1.00	0.89	0.99
2T	0.94	0.97	0.92	0.98
3T	0.91	0.75	0.87	0.90

Table 6.1.2 - Normalised frequencies and MACs compared to the undelaminated mode-shapes for cases 5 to 8

Discounting the fundamental bending and torsional modes, which had large experimental error, and looking at the values of MAC in table 6.1.2, it can be seen that eight modes seem to have been affected by the presence of delaminations. These were:

- Third torsion for case 5
- Fourth bending and third torsion for case 6
- Fourth bending and third torsion for case 7, and
- Second, third and fourth bending and third torsion case 8

These modes are shown compared to the modes for the undelaminated beam (Case 4) in figures 6.1.3 to 6.1.6. For the bending modes, both an increased gradient at the delamination location, and the shift in maximum peak location, is again evident. Also, the third bending mode for case 5 and second bending mode for cases 4 and 7, are plotted. Although these did not show low MAC values, it was expected from the numerical analyses in Chapter 4 that the delaminations would show a significant effect. Although having MACs of 0.99 and 1.00, the delaminated beam again has an increased amplitude away from the tip of the beam, and increased gradient at the delamination location. The MAC cannot distinguish between modes that are scaled to be larger or smaller, but are otherwise identical. Therefore, because the peaks have not moved significantly along the *Y*-axis, but only increased in amplitude, the MAC shows little effect.

The characteristic effects of a delamination of the mode-shape of a beam is less pronounced for the $[0°,\pm45°,0°]_s$ than for the $[0°,90°]_{2,s}$ beams. This is probably due to the low number of test points used for the $[0°,90°]_{2,s}$ beams, which tend to amplify the differences due to the normalisation process. However, some of the effect may be due to the higher pressure used for the $[0°,\pm45°,0°]_s$ laminates, which may have reduced the resin leakage and produced delaminations with lower area. Another reason for the smaller effects encountered for these beams could be slippage of the Teflon plies, moving the delamination to regions of lower shear force for a particular mode. This problem was reported by Almond *et al.* (1996), when the delamination size, measured by transient thermography, was different to the size of the Teflon they had inserted in the laminate.

The low values of MAC for the torsion modes, showing the lack of correlation between the undelaminated and delaminated beams, appear to be more due to experimental error than the effect of delamination, as no characteristic effects can be seen when examining the changes in mode-shapes.

a)

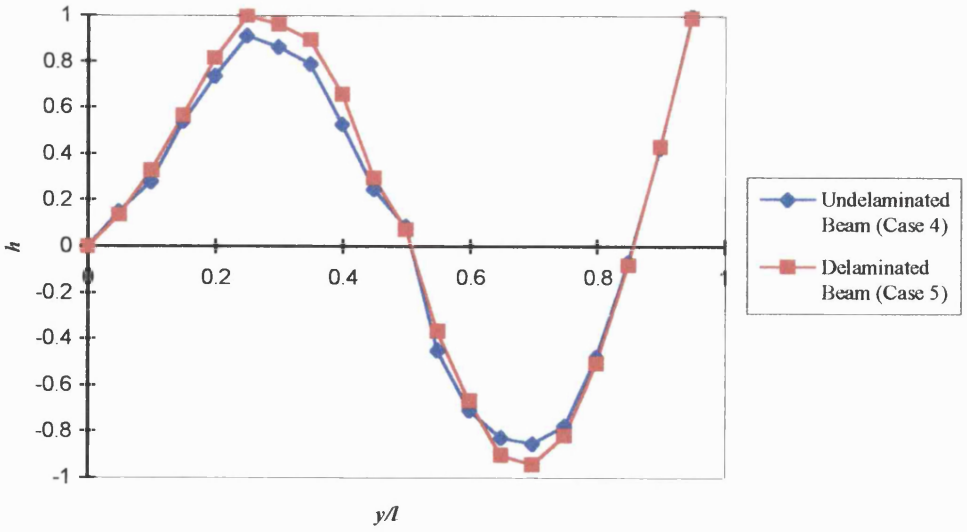

b)

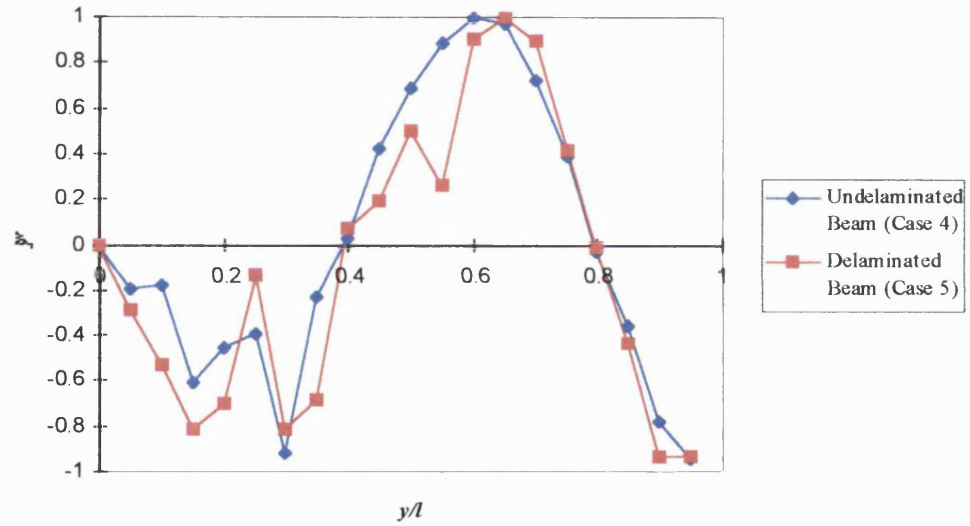

Figure 6.1.3 - Mode-shape comparison for delaminated and undelaminated $[0^o,\pm45^o,0^o]_s$ beams

a) Third bending of cases 4 and 5

b) Third torsion of cases 4 and 5

a)

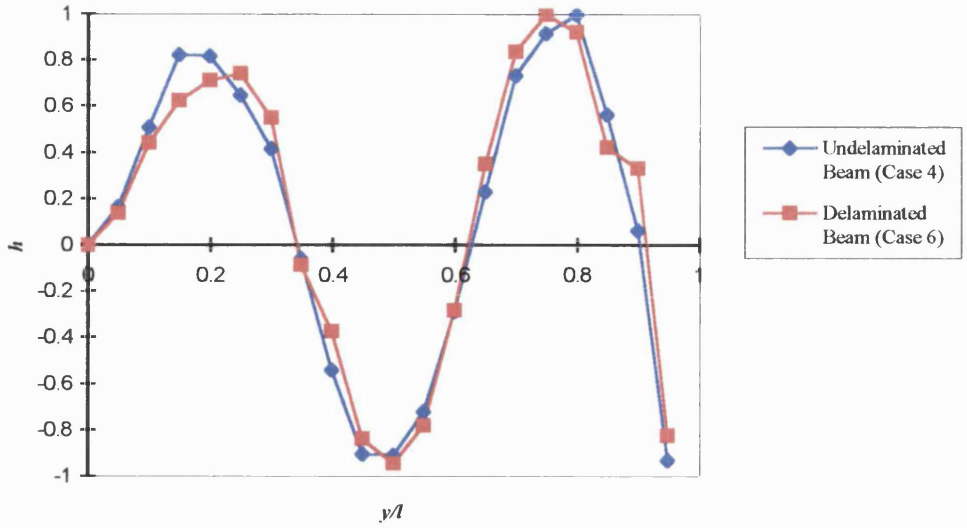

b)

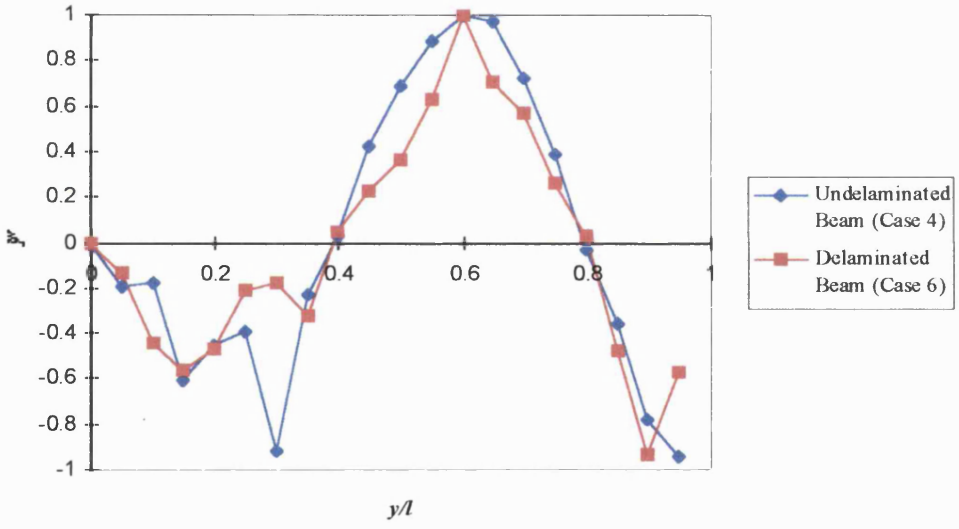

Figure 6.1.4 - Mode-shape comparison for delaminated and undelaminated $[0^o,\pm45^o,0^o]_s$ beams

a) Fourth bending of cases 4 and 6

b) Third torsion of cases 4 and 6

a)

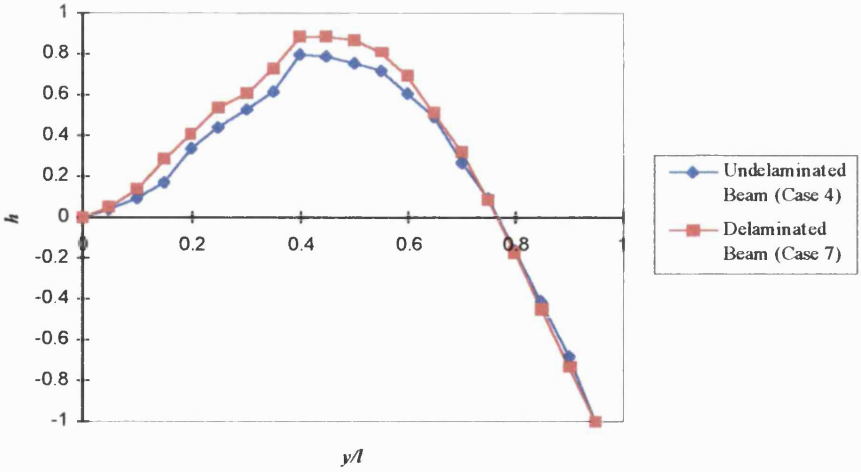

b)

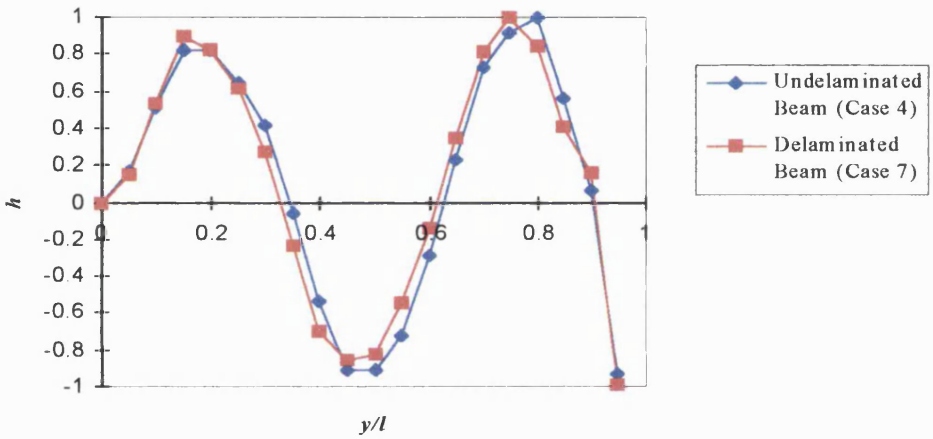

c)

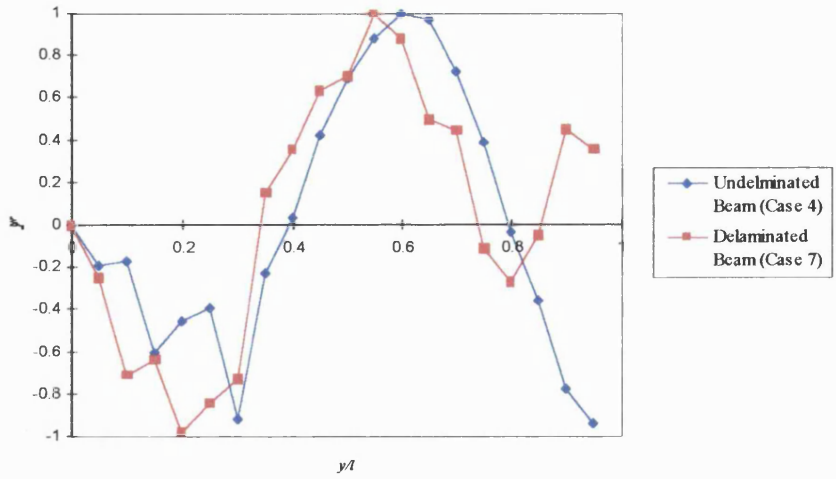

Figure 6.1.5 - Mode-shape comparison for delaminated and undelaminated $[0^o,\pm45^o,0^o]_s$ beams a) Second bending of cases 4 and 7 b) Fourth bending of cases 4 and 7 c) Third torsion of cases 4 and 7

a)

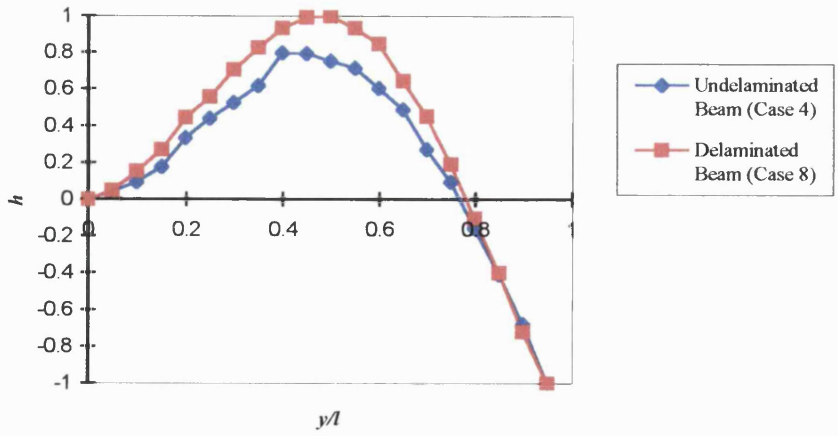

b)

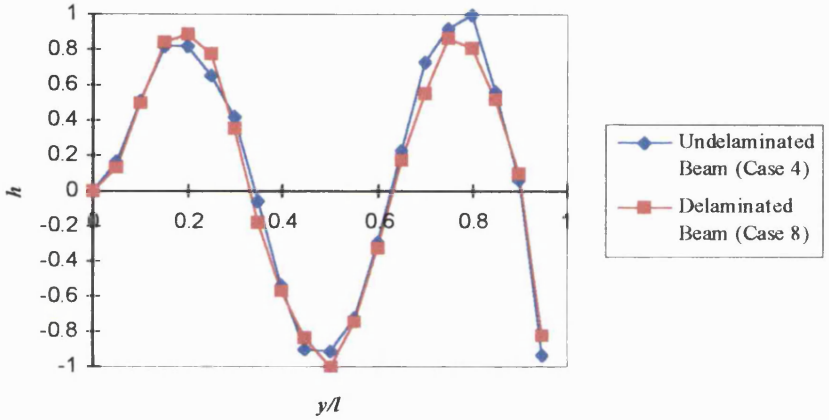

c)

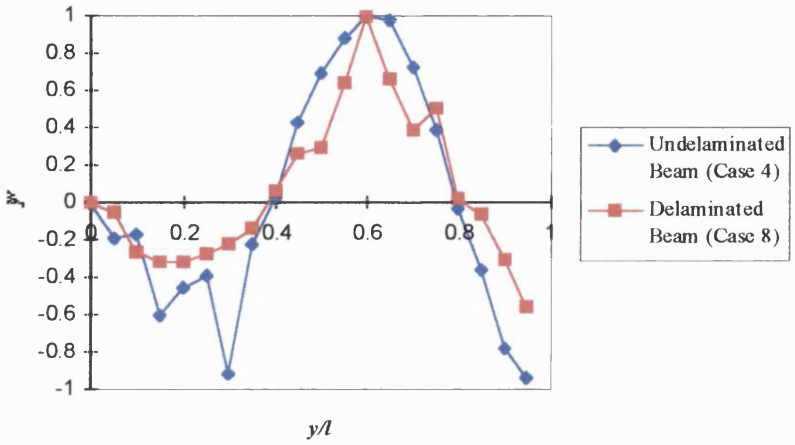

Figure 6.1.6 - Mode-shape comparison for delaminated and undelaminated $[0^o,\pm45^o,0^o]_s$ beams a) Second bending of cases 4 and 8

b) Fourth bending of cases 4 and 8 c) Third torsion of cases 4 and 8

6.1.2 Beams with Low-Velocity Impact Damage

In this section, the experimental results for the beams with low-velocity impact damage are presented. The laminate geometry and extent of damage is described in Chapter 5. Each beam was tested before and after damage.

Appendix C again presents the frequencies measured for each beam in the undamaged and damaged states, together with the ratio of damaged to undamaged frequencies for each mode. It appears from the ratio of damaged to undamaged frequencies that the effect of the impact damage was too small to be detected using modal analysis. In no case has the frequency dropped by over 2% of the original value, and most of the variation in frequency can be accounted by experimental error.

However the frequencies and mode-shapes of the undamaged laminates can be used to assess the accuracy of the DSM. Mode-shapes for the two laminate types are shown in figures 6.1.7 and 6.1.8. Only two laminates are displayed because the mode-shapes for the equivalent laminate of different thickness are similar. Both laminates show significant plate-like behaviour, with significant anti-clastic bending evident.

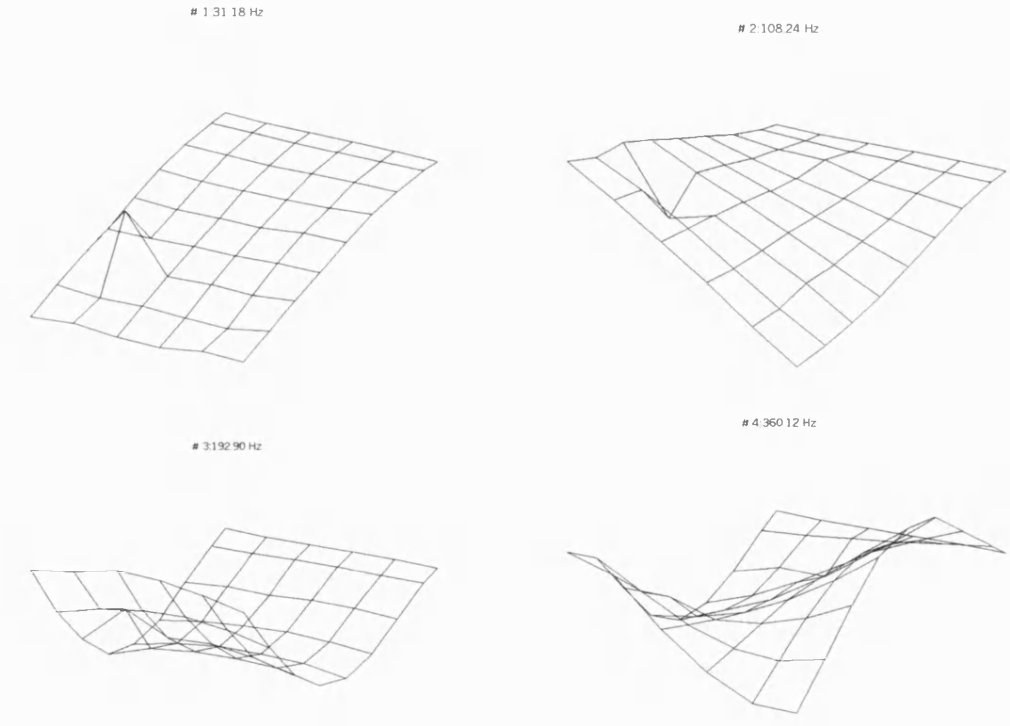

Figure 6.1.7 - Mode-shapes for the $[(-45°,+45°,0°)_s]_n$ uni-directional unit ply laminate (#1 - 1B, #2 - 1T, #3 - 2B, #4 - 2T)

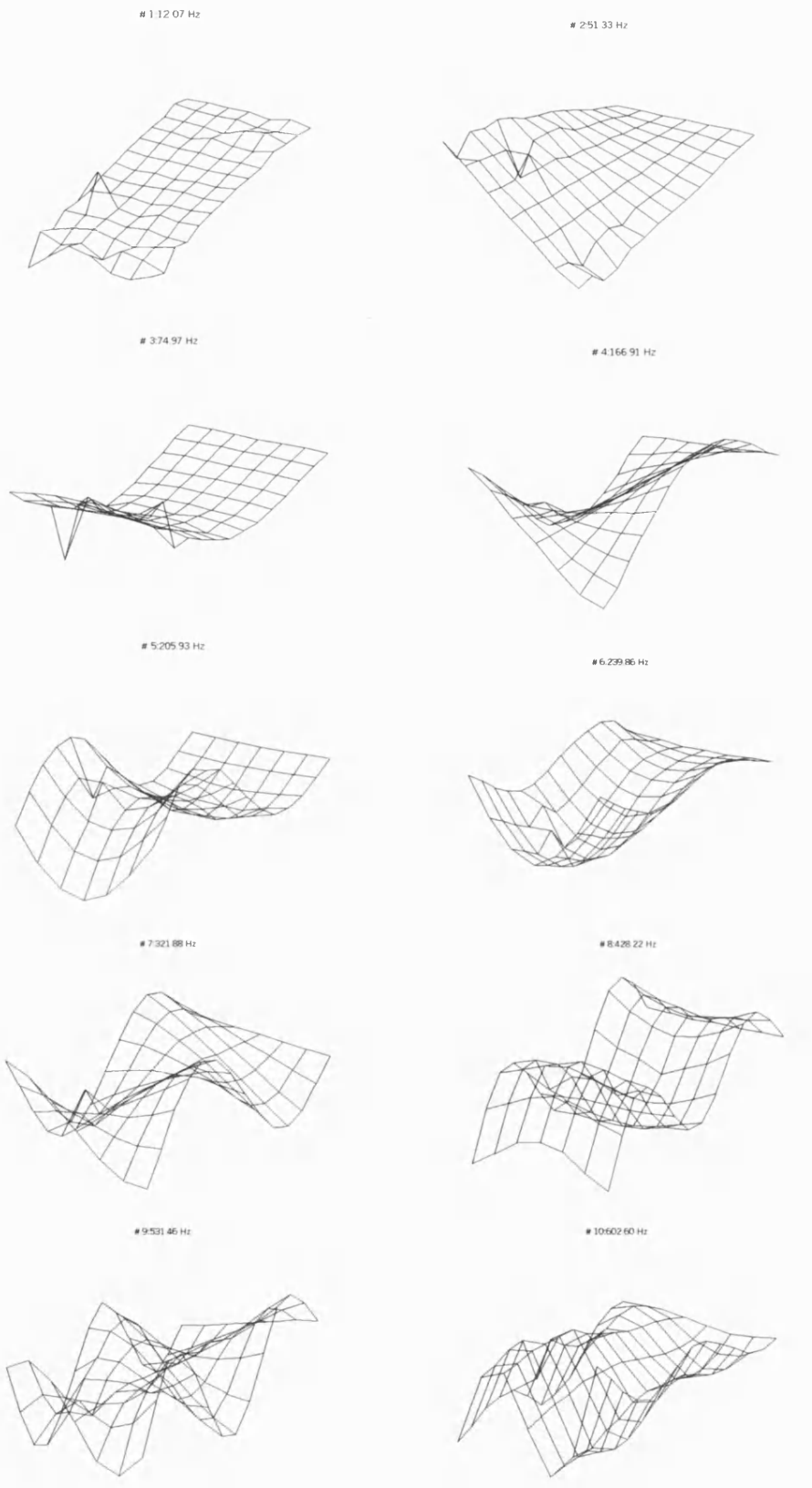

Figure 6.1.8 - Mode-shapes for the $[(-45°,+45°,0°)_s]_n$ non-crimp fabric unit ply laminate (#1 - 1B, #2 - 1T, #3 - 2B, #4 - 2T, #5 - 3B, #6 - 4B, #7 - 3T, #8 - 5B , #9 - 1M, #10 - 2M)

6.2 Comparison of Experimental and Numerical Results

The experimental values presented in the preceding section were used to assess the accuracy of the numerical models. Values for frequency and mode-shapes of the undelaminated beams are used to assess the accuracy of the material properties and clamping arrangements assumed, as well as assessing the accuracy of the DSM. The results from the beams with simulated delaminations are used to assess the accuracy of incorporating the equivalent shear rigidity in the DSM. Although it is known that the model used to derive the reduced torsional rigidity of a delaminated section is inaccurate, this was also carried out for the torsional modes. Frequencies and mode-shapes from the undelaminated plates are used to assess the accuracy of the beam model DSM in simulating plate-like behaviour, and comments are made as to the suitability of using the beam model for damage detection in such structures.

6.2.1 Beams with Simulated Delaminations

6.2.1.1 Comparison of Experimental and Numerical Results for the Undelaminated Beams

Using the manufacturer's material properties given in table 5.1.1, the element properties were calculated for the undelaminated beam. These were then incorporated into the DSM to obtain frequencies and mode-shapes. Twenty DSM elements were used. For the $[0°,90°]_{2,s}$ laminate (Case 1), the element properties were calculated to be:

$$EI = 0.4136\ \text{Nm}^2\ ;\ GJ = 0.01783\ \text{Nm}^2\ ;\ K_{BT} = 0.0\ \text{Nm}^2\ ;\ kAG = 2.675\times10^4\ \text{N}$$

and for the $[0°,\pm45°,0°]_s$ laminate (Case 4), they were calculated to be:

$$EI = 0.3610\ \text{Nm}^2\ ;\ GJ = 0.2255\ \text{Nm}^2\ ;\ K_{BT} = 0.01\ \text{Nm}^2\ ;\ kAG = 3.121\times10^4\ \text{N}$$

Table 6.2.1 and 6.2.2 compares the frequencies and mode-shapes (via the MAC) obtained from the DSM, with those measured experimentally.

When comparing the experimental torsion mode-shapes with those produced by the DSM via the MAC, the experimental torsional mode-shape vectors were transformed via equation (3.3.2).

Mode	Experimental Frequency [Hz]	Analytical Frequency [Hz]	% Difference	MAC
1B	14.45	13.44	-6.99	0.83
2B	91.28	83.91	-8.07	1.00
3B	250.79	226.30	-9.77	0.98
4B	486.03	414.83	-14.65	0.98
1T	71.97	25.79	-64.17	0.92
2T	221.85	77.36	-65.13	0.99
3T	422.77	128.94	-69.50	0.81
4T	684.09	180.52	-73.61	0.51

Table 6.2.1 - Comparison of frequencies and mode-shapes produced experimentally and numerically for the $[0°,90°]_{2,s}$ laminate (Case 1)

Mode	Experimental Frequency [Hz]	Analytical Frequency [Hz]	% Difference	MAC
1B	14.20	12.54	-13.24	0.98
2B	88.25	78.30	-12.71	0.99
3B	242.58	211.27	-14.82	0.99
4B	482.12	387.38	-24.46	0.99
1T	123.08	91.64	-34.31	0.96
2T	355.52	274.93	-29.31	0.89
3T	641.93	458.32	-40.06	0.83
4T	-	641.93	-	-

Table 6.2.2 - Comparison of frequencies and mode-shapes produced experimentally and numerically for the $[0°,\pm45°,0°]_s$ laminate (Case 4)

For case 1, shown in table 6.2.1, the bending mode-shapes show good agreement between the numerical results and experiment, with the difference in frequency remaining under 15%. The MACs also seem to show good correlation, apart from mode 1. This is probably due to experimental error, as very low frequencies are more susceptible to noise if a wide experimental frequency band is used. The bending modes for case 4, given in table 6.2.2, also show good agreement, although the differences are greater, and the MACs show a good correlation.

The frequencies of the bending modes predicted by the DSM are consistently lower than the experimental frequencies, which suggests that this is not due to random experimental error. The underestimation could be due to anti-clastic stiffening of the beams, but with a ratio of length to width of 6, the effect is probably small. The error is probably due to incorrect material properties being used, perhaps owing to a too low estimation of fibre volume fraction.

Compared to the bending modes, the frequencies of the torsional modes have not been predicted well by the DSM. The frequencies for the $[0°,90°]_{2,s}$ laminate are consistently underestimated by approximately 60%, and for the $[0°,\pm45°,0°]_s$ by approximately 30%. This was not expected, as previous work has shown the DSM agreeing well both with experimental and FE results. Similar beams analysed by the DSM (Taylor and Butler (1997)) have shown less than 7% difference with experimental results.

The differences in the frequencies are too large to be attributed to incorrect material properties, and, at least for the $[0°,\pm45°,0°]_s$ beams when the beams were removed and then re-clamped for each test, the clamping arrangements were not seen to be responsible for much of the discrepancy. It is suspected that the laminates are so thin that, during torsional deformation, some of the beam edges are out of phase when compared to the majority of the beam. A representation of this out of phase deformation is shown for an arbitrary position along the beam in figure 6.2.1.

This extra strain in the torsion modes results in an effective increase in the stiffness of the beam, and an increase in frequency for the modes affected. This effect is less pronounced when the torsional rigidity is increased, and hence the error is less for the $[0°,\pm45°,0°]_s$ beams. For thicker beams, which have relatively higher torsional rigidities, the error is small. A comparison study using FE seemed to confirm this, as the FE model agreed well with the experiment for the thin beam, and also agreed well with the DSM for thicker laminates of the same lay-up,

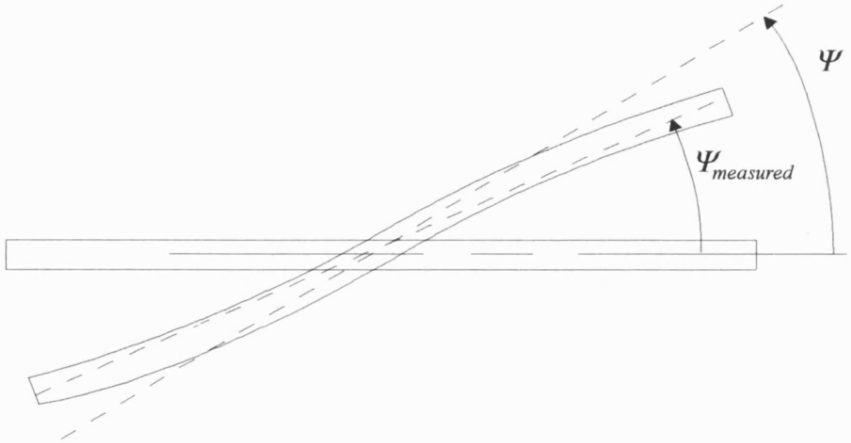

Figure 6.2.1 – Torsional deflection of a beam cross-section, showing theoretical definition of torsional deflection, Ψ, and the measured deflection due to out-of-phase motion, $\Psi_{measured}$

6.2.1.2 Comparison of Experimental and Numerical Results for the Delaminated Beams

Tables 6.2.3 and 6.2.4 show the analytical normalised delaminated frequencies and MACs when compared to the undelaminated modes, for cases 2 and 3 and 5 to 8, respectively. These can be compared to tables 6.1.1 and 6.1.2 to assess the accuracy of modelling a delamination as a reduced shear and torsional rigidity in the DSM.

	Case 2		Case 3	
Mode	ω'	**MAC**	ω'	**MAC**
1B	0.99	1.00	0.99	1.00
2B	0.99	1.00	0.99	1.00
3B	0.89	0.98	0.95	0.98
4B	0.94	0.95	0.83	0.93

Table 6.2.3 - Normalised numerical bending frequencies and MACs compared to undelaminated (case 1) mode-shapes for cases 2 and 3

	Case 5		Case 6	
Mode	ω'	**MAC**	ω'	**MAC**
1B	1.00	1.00	1.00	1.00
2B	1.00	1.00	1.00	0.99
3B	0.97	1.00	0.99	0.99
4B	0.98	0.99	0.95	0.98
1T	0.50	0.52	0.57	0.85
2T	0.72	0.66	0.61	0.71
3T	0.65	0.32	0.62	0.32

	Case 7		Case 8	
Mode	ω'	**MAC**	ω'	**MAC**
1B	0.99	1.00	0.99	1.00
2B	0.96	0.99	0.92	0.99
3B	0.93	0.97	0.87	0.99
4B	0.93	0.94	0.87	0.98
1T	0.40	0.59	0.77	0.99
2T	0.76	0.60	0.88	0.64
3T	0.63	0.25	0.93	0.73

Table 6.2.4 - Normalised numerical frequencies and MACs compared to undelaminated (case 4) mode-shapes for cases 5 to 8

In all cases the frequency drop calculated by the DSM is in good agreement with that measured experimentally for the bending modes, with a maximum difference of 4%. The MAC values also show reasonable agreement, although in most cases the DSM predicts a lower correlation than seen experimentally. This is unexpected, as the experimental values for MAC include the effect of measurement error, which should drive the values lower than those predicted numerically.

The DSM also agrees with the experimental results which show that the $[0°,\pm45°,0°]_s$ laminate is effected less by the delaminations than the $[0°,90°]_{2,s}$ laminate. This is at odds with Tracy and Pardoen (1989), who state that a higher ratio of sub-laminate axial stiffness to undelaminated

bending stiffness should give a larger frequency drop. Using the non-dimensionalised ratio defined by Tracy and Pardoen, gives:

$$\left[\frac{(EA)_A d^2}{12EI}\right]_{[0,90]_{2s}} = 0.324$$

$$\left[\frac{(EA)_A d^2}{12EI}\right]_{[0,\pm 45,0]_s} = 0.423$$

where EI is the bending stiffness of the undelaminated laminate, $(EA)_A$ is the axial stiffness of sub-laminate A (shown in figure 2.3.2), and d is the thickness of the laminate.

Even though it is known that the model used to predict the torsional rigidity of a delaminated section is inaccurate, and because of the geometry of the beams the DSM does not predict the undelaminated dynamics very well, the drop in torsional frequencies and change in mode-shapes are also shown. It can be seen that DSM prediction of the delaminated torsional frequencies and mode-shapes is not accurate. As expected, the reduced torsional rigidity terms of the delaminated laminate has over-estimated the drop in frequency, and have greatly affected the torsional mode-shapes. This, together with the stiffening effect of the out of plane deformation of the experimental beams, which causes the DSM to under-estimate the undelaminated frequencies, means that the values of delaminated torsional frequencies are very much under-estimated.

As described in Chapter 2, the some of the underestimation of the torsional rigidity is probably due to the fact that no consideration has been made for the misalignment of the end-faces due to twist. This causes the torsional rigidity of the undelaminated section to be underestimated, and therefore causes the DSM to predict the very low torsional frequencies and highly-altered mode-shapes. The effect is also more pronounced for the $[0°,\pm 45°,0°]_s$ laminate than for other laminates. This is because when delaminated, the ±45° layers are close to the neutral axis and therefore do not contribute as much to the torsional rigidity of the sub-laminates than they would if they were at the top and bottom surfaces. The simple sum of the sub-laminate torsional rigidities, as given in equation (2.3.29), is therefore very low. However, the ±45° plies still contribute a significant amount to the transverse shear rigidity, which would be the factor that affects the amount of force necessary to ensure end-face compatibility. As described in section 2.3.2.1, this would increase the torsional rigidity of the delaminated section.

For both experimental laminates, however, the material bending-torsion coupling constants for the whole laminate are very small, so that the over-estimated effect on torsional modes does not affect the bending modes. This fact means that the optimisation process used for damage detection is still valid if only the bending frequencies and modes are used. With a highly coupled laminate, however, a more accurate method for determining the effective torsional stiffness of the delaminated beams, that includes the end-face compatibility, must be incorporated.

6.2.2 Beams with Low-Velocity Impact Damage

For the beams with low-velocity impact damage, the experimental results did not show a significant reduction in frequency for the damaged beams. Therefore the DSM is compared only with the experimental results for the undamaged beams. This gives an indication of using the DSM to model beams with low aspect ratios, which can show significant plate-like behaviour.

Tables 6.2.5 to 6.2.9 compare the frequencies and mode-shapes of the experimental beams without delaminations, with the equivalent results calculated by the DSM. In all cases the DSM agrees reasonably well with the experimental results, with the possible exception of the mode-shape comparison for case 4. However, on inspection of the experimental mode-shapes, it was evident that there was considerable experimental error, and the low MAC values can be taken as a measure of error, not of incorrect numerical results. Unlike the results for the beams manufactured in-house, the DSM also agrees well the experimental frequency of the torsional modes. Even though some out of plane deformation is evident when inspecting the mode shapes (Mode 7 in figure 6.1.8 for example), the high torsional rigidity has reduced the effect so that it does not increase the frequency noticeably.

This is a significant result for the DSM. Although the application of the DSM used in this thesis is based on beam theory, it appears that, as long as the laminates have a large thickness, the DSM can be applied to structures that show significant plate-like behaviour with some confidence of the accuracy of the results. Therefore damage detection using the methods described in Chapter 3 should be possible. Assuming this is true for beams with different boundary conditions, this means that the methods can be used on structures which are more like the ones seen in the aviation industry, such as the aircraft wing panels. This is a possible avenue for further work.

Mode	Experimental Frequency	DSM Frequency	% Difference	MAC
1B	31.54	28.50	-9.64	1.00
2B	192.85	176.30	-8.58	0.95
1T	107.19	89.56	-16.45	0.98
2T	357.14	268.73	-24.75	0.98

Table 6.2.5 - Comparison of experimental results with DSM results for $[(+45°,-45°,0°,90°)_2]_s$ undelaminated beam (Case 9)

Mode	Experimental Frequency	DSM Frequency	% Difference	MAC
1B	62.41	62.19	-0.35	1.00
2B	384.75	368.33	-4.27	0.89
1T	204.53	171.99	-15.91	0.88
2T	516.80	516.00	-0.15	0.86

Table 6.2.6 - Comparison of experimental results with DSM results for $[(+45°,-45°,0°,90°)_4]_s$ undelaminated beam (Case 10)

Mode	Experimental Frequency	DSM Frequency	% Difference	MAC
1B	56.76	50.82	-10.47	1.00
2B	340.59	301.28	-11.54	0.99
1T	222.53	197.15	-11.41	0.98
2T	445.86	590.63	32.47	0.92

Table 6.2.7 - Comparison of experimental results with DSM results for $(+45°_4,-45°_4,0°_4,90°_4)_s$ undelaminated beam (Case 11)

Mode	Experimental Frequency	DSM Frequency	% Difference	MAC
1B	12.32	10.02	-18.67	0.94
2B	75.76	62.69	-17.25	0.85
3B	208.24	169.32	-18.69	0.70
1T	51.06	47.63	-6.72	0.82
2T	166.30	142.86	-14.10	0.88
1M*	239.19	238.14	-0.44	-
2M*	320.65	310.36	-3.21	-
3M*	431.00	333.66	-22.58	-

Table 6.2.9 - Comparison of experimental results with DSM results for $[(+45°,-45°,0°)_s]_2$ undelaminated beam (Case 12)

*** - Neither bending nor torsional motion dominant. No MAC possible**

Mode	Experimental Frequency	DSM Frequency	% Difference	MAC
1B	26.43	23.69	-10.37	0.89
2B	163.19	147.11	-9.85	0.97
1T	103.32	101.86	-1.41	0.87

Table 6.2.8 - Comparison of experimental results with DSM results for $[(+45°,-45°,0°)_s]_4$ undelaminated beam (Case 13)

7. Detection of Delaminations using Numerical Optimisation

In this chapter, the static beam model and the DSM are used to investigate damage detection and location using the optimisation techniques outlined in Chapter 3. The relative merits of the two optimisation techniques are investigated via a numerical investigation, which shows the sensitivity of the process to small errors.

Finally, the optimisation methods are applied to experimental results for delaminated beams, to assess the extent of the experimental damage and to locate it within the beams.

7.1 Numerical Investigation of Damage Detection

In order to fully understand the merits of the optimisation methods when detecting delaminations, it is necessary to determine whether the errors in final design variable solutions occur because of errors in the natural frequencies and mode-shapes obtained by experiment, or due to mechanisms inherent in the optimisation procedures. It is therefore necessary to remove the errors inherent in experiments from the input data. This was achieved by calculating natural frequencies and mode-shapes of undamaged and damaged beams using the analytical method, and using these results as input data for the optimisation process.

The laminate chosen for the numerical investigation was similar to the experimental laminates, being 8-layers of carbon-fibre epoxy material, but had a laminate geometry of $[-45°,+45°,90°,0°]_s$. This was chosen to be representative of thin laminates used in the aviation industry, such as wing and rotor-blade skins, with the 45° layers used to increase impact tolerance and torsional rigidity, and the 0° and 90° layers used to increase bending and axial stiffness in the in-plane directions. The material properties of the carbon-fibre/epoxy laminate were obtained from Smith (1972), and are shown in table 7.1.1.

Each beam had a length of 1m and a width of 0.075m, and had a thickness of 1mm.

Three damage cases were used, each containing a full-width delamination at one ply location. Table 7.1.2 summarises the test cases used.

$E_1 = 144.0\times10^9$ Pa	$\nu_{12} = 0.48$	$G_{12} = 6.2\times10^9$ Pa
$E_2 = 11.2\times10^9$ Pa	$\nu_{23} = 0.46$	$G_{13} = 6.2\times10^9$ Pa
$E_3 = 10.5\times10^9$ Pa	$\nu_{31} = 0.038$	$G_{23} = 3.5\times10^9$ Pa
$\rho = 1550$ kg/m^3 *	$t_{ply} = 0.125$ mm *	

* - Assumed value

Table 7.1.1 – Carbon-fibre/epoxy material properties

Test Case Number	Lay-Up	$\frac{l_a}{l}$	$\frac{l_d}{l}$	$\frac{l_b}{d}$
1	$[-45°,45°,90°,0°]_s$	0.45	0.1	0.25
2	$[-45°,45°,90°,0°]_s$	0.25	0.1	0.25
3	$[-45°,45°,90°,0°]_s$	0.75	0.2	0.25

Table 7.1.2 - Laminate geometry and position of delamination for the beams with analytical delaminations

It is often useful to visualise the design space of the problem, and a 2-D representation is only possible if the problem is restricted to two design variables. If the starting Z position of the delamination is specified at the beginning of the optimisation (i.e. restricting X_3 to 0.25), the problem remains relatively simple, and can be shown graphically.

This was achieved by calculating the objective function for all combinations of delamination size and horizontal location in steps of 0.01. Linear interpolation was then used to determine the values of X_1 and X_2 that produced constant values of objective function. A contour diagram of the objective function can then be produced, which shows lines along which the objective function $O(X)$ takes specific constant values. Figure 7.1.1 shows such a contour diagram for Case 1 of the analytically produced problem, using the first ten frequencies and mode-shapes. The objective function, given in equation 3.3.1, was formulated with α=1.0, and β=15.0, which ensured that

the frequency part and the mode-shape part of the objective function were of the same order at convergence. Also, the mode-shapes were quantified at five points along the beam length, these being at 10%, 50%, 60%, 90% and 100% of the beam length.

Figure 7.1.1 shows iso-values of objective function for values of X_1 from 0-1 (i.e. its lower and upper bounds), and X_2 from 0-0.5. The unfeasible regions created by combinations of X_1 and X_2 that do not satisfy equations (3.3.17a) and (3.3.17b), are also shown.

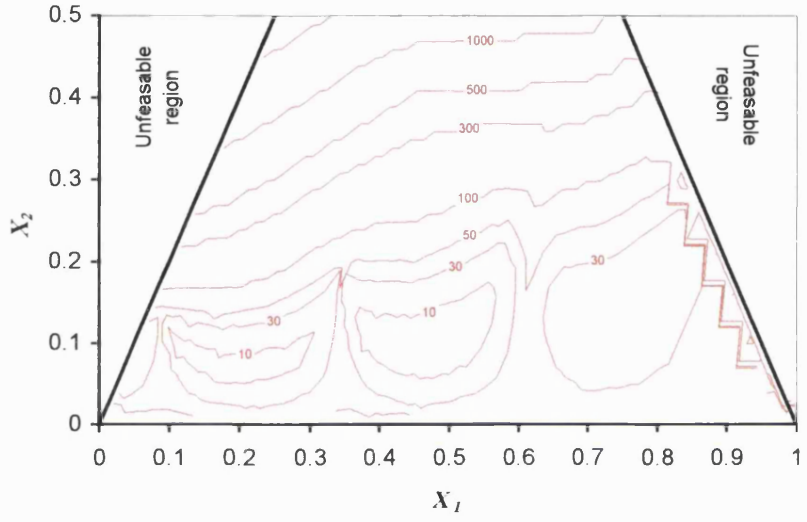

Figure 7.1.1 – 2-Dimensional design space created by a single delamination (Case 1)

Three regions where the objective function is at a local minimum can be identified in figure 7.1.1. The centre region contains the point where the objective function has a value of 0.0. Having three local minimum solutions causes a problem for the gradient-based optimisation method, which can find a local minimum solution. It is therefore necessary to choose various starting positions for the optimisation, and relatively large initial step sizes so that a wide range of the design space is sampled. This has the effect of reducing the efficiency of the optimisation method. It can also be seen from this figure that, as expected, the size of the delamination has a greater effect on the objective function that its location. The irregularity of the design space towards the right of the design space arises from the way the size of the beam is quantified when equation (3.3.17b) is not satisfied. In this case, to provide a solution from the analytical model so that the optimisation

process does not fail, the length of the beam is simply extended to $\frac{X_1}{2} + X_2$, which sharply reduces the natural frequencies of the beam. This fact, combined with the linear interpolation between points, causes the irregularity on the graph.

Table 7.1.3 shows the best solutions for the three cases, using the gradient-based optimisation method, and the genetic algorithm. The best solution for the third design variable, X_3, was found for the gradient-based method by performing one optimisation process for each layer, and locating the layer that had the lowest objective function. To ensure a local minimum solution was not located using the gradient-based method, three starting positions were chosen.

It can be seen that, as would be expected, both optimisation methods have located the delaminations successfully, although the gradient-based procedure has not located the delamination within the beam very well for case 2. Also, even though three starting positions, and a large initial step size was used in the gradient-based method, which has the effect of reducing its efficiency, the number of function calls remains lower than for the GA for this simple problem.

Test Case Number	Method	X_1	X_2	X_3	Number of evaluations
1	Gradient	0.502	0.038	0.25	784
	GA	0.499	0.099	0.25	1605
2	Gradient	0.127	0.087	0.25	888
	GA	0.249	0.101	0.25	1565
3	Gradient	0.748	0.200	0.25	928
	GA	0.749	0.202	0.25	1044

Table 7.1.3 - Final optimiser solution of delamination location and size for the beams with analytical delaminations

When the complexity of the problem is increased, by introducing a larger number of design variables to allow for more delaminations in either the Y or Z axis, the efficiency of the gradient-based method is reduced when compared to the GA. If it is known that the delaminations occurred

at one location (For example, one impact was recorded), the number of possible combinations of delamination positions, and hence the number of optimiser runs necessary, is:

$$n_{combinations} = (n_{plies} - 1)n_{delams} - \sum_{i=1}^{n_{plies}-1} i$$

where n_{plies} is the number of plies, and n_{delams} is the total number of delaminations allowed for. If multiple impact positions are allowed for, the number of possible combinations increases to:

$$n_{combinations} = (n_{plies} - 1)n_{delams}$$

Reducing the allowable number of delaminations to one, therefore, reduces the time necessary for optimisation, which would obviously soon become prohibitively time consuming.

The potential effect of experimental error was also assessed using the analytical design cases, by introducing a random error on each of the frequencies and mode-shapes, such as may be made by experimental sampling errors. Random errors of up to 5%, 10% and 20% were introduced to the input data of the three cases, each with ten error cases. A similar procedure was carried out by Williams *et al.* (1997), who seeded a set of frequencies with random errors to assess the impact of the number of modes on their damage detection procedure.

Figure 7.1.2 shows the converged solutions for X_1 and X_2 for Case 1, using the GA. It can be seen that, as expected, as the error in the input data increases, the final solution becomes more inaccurate. With only a 5% error added to the input data, the solution remains reasonably acceptable, but with greater experimental errors the solution becomes very inaccurate. It can also be seen that the position of the delamination is much more sensitive to errors than the size, due to the fact that the delamination size has much more of an effect on the frequencies and mode-shapes than its position. Although not shown on figure 7.1.2, the position of the delamination through the thickness of the delamination was also seen to be tolerant of experimental error. The ply location of the delamination was successfully located for all ten cases when a 5% error was introduced, and all but two for a 10% starting error. It was not until a 20% error was introduced that the accuracy of the solution for X_3 reduced significantly.

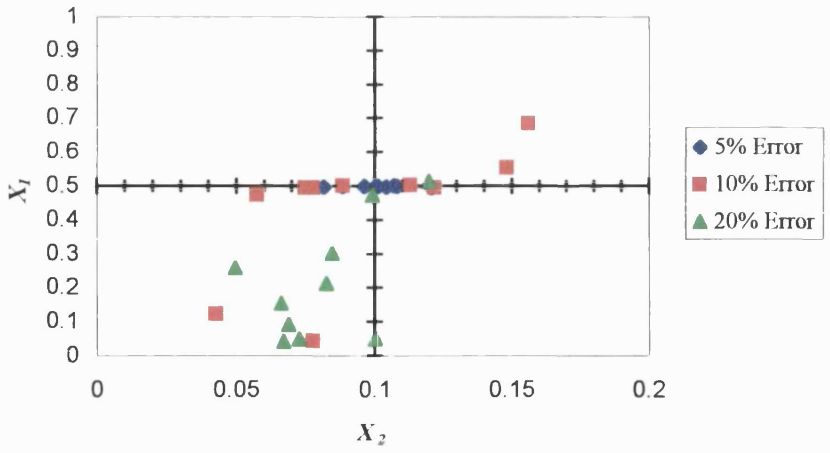

Figure 7.1.2 – Converged solutions for case 1 with random errors added to the input data

The 5% error added to the natural frequencies is representative of the experimental error seen during testing. The experimental measurements of natural frequency obtained for this research can be said with reasonable confidence to be accurate. The measured values of frequency given in Appendix C show that an error of less than 5% was obtainable in most cases. However, from inspection of the mode shapes in figure 6.1.2 it can be seen that errors in each individual mode shape point can be significantly higher, due to human factors in using impact testing. In extreme cases, variations of over 60% were observed at points in the experimental mode-shapes. Therefore, the 20% error used for this investigation is more representative of the error in mode-shapes.

7.2 Detection and Location of Experimental Damage

In this section, the results obtained by experiment for the composite beams with "simulated" delaminations are used to detect damage. A series of beams were tested, and for convenience table 7.2.1 shows laminate geometry and the normalised size and location of the delaminations, which are shown un-normalised in table 5.1.2. The definitions of the variables can be obtained from figure 3.3.2.

As explained in Chapter 2, this is a two-stage process, consisting of the characterisation stage, and the damage detection stage.

Test Case Number	Lay-Up	$\frac{l_a}{l}$	$\frac{l_d}{l}$	$\frac{l_b}{d}$
1	$[0°,90°]_{2,s}$	-	-	-
2	$[0°,90°]_{2,s}$	0.49	0.167	0.5
3	$[0°,90°]_{2,s}$	0.62	0.167	0.5
4	$[0°,\pm45°,0°]_s$	-	-	-
5	$[0°,\pm45°,0°]_s$	0.49	0.167	0.5
6	$[0°,\pm45°,0°]_s$	0.62	0.167	0.5
7	$[0°,\pm45°,0°]_s$	0.117	0.167	0.5
8	$[0°,\pm45°,0°]_s$	0.117	0.167	0.25

Table 7.2.1 - Laminate geometry and position of delamination for the beams with simulated delaminations

7.2.1 Experimental Beam Characterisation

In the structural characterisation stage, experimental frequencies and mode-shapes for the undamaged beams are used to quantify the material properties and boundary conditions. It was envisaged for this stage, that the structure would remain fixed to its support during its life, and that any damage would occur in-situ. However, because the delaminations were produced artificially, it was necessary to produce undamaged beams, and different damaged beams. The boundary conditions change for each beam, and, therefore, for the undamaged and damaged cases. Therefore, the structural characterisation was carried out only for case 1 in table 7.2.1, and it was assumed that the material properties and support stiffnesses remained similar throughout the remainder of the experimental tests.

The objective function was formulated with α =1.0, and β =50.0, and the mode-shapes were quantified at points which were 20%, 40%, 60%, 80% and 100% along the length of the beam. Because of the uncertainty of the accuracy of mode 1, a weighting factor of 0.8 was used on this mode. Also, an initial step size of 0.01 was specified.

As the experimental beams seemed to show a large increase in torsional stiffness due to out-of plane motion, and it was known that the model used to obtain the torsional rigidity of the

delaminated section was inaccurate, the torsional modes were not used in the characterisation or damage detection stages. Only the first four undamaged bending modes were therefore used.

Figure 7.2.1 shows how the objective function and design variables varied throughout the optimisation. The initial material properties were as in table 5.1.1, and the clamp support stiffnesses were 1×10^5 N/m, 1×10^5 Nm/rad, and 1×10^5 Nm/rad for k_h, k_θ and k_ψ, respectively. The initial value of the objective function, as defined in equation (3.3.1), based on the first four bending frequencies and mode-shapes, was 305.5. After 11 iterations, the value of the objective function had reduced to 69.3, when the termination criteria had been reached. The initial and final bending frequencies produced by the optimised material properties and support stiffnesses, as well as the experimental frequencies, are shown in table 7.2.2.

Mode	Initial DSM Frequency [Hz]	Final DSM Frequency [Hz]	Experimental Frequency [Hz]
1	14.00	14.33	14.45
2	86.86	89.22	91.28
3	231.92	239.64	250.79
4	419.67	437.24	486.03

Table 7.2.2 – Initial and final optimiser frequencies and experimental frequencies for the $[0°,90°]_{2,s}$ beam (Case 1)

a)

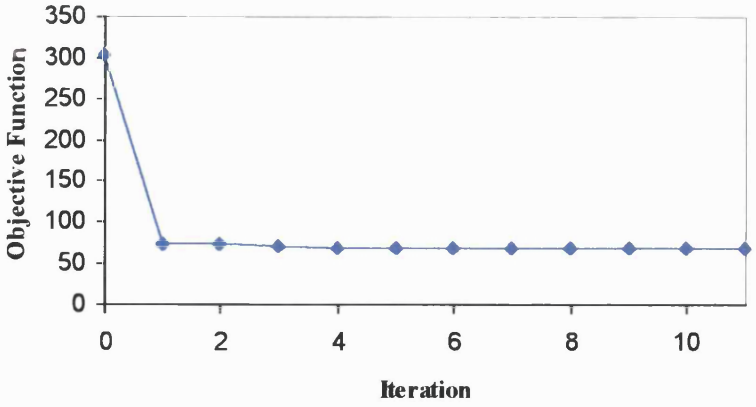

b)

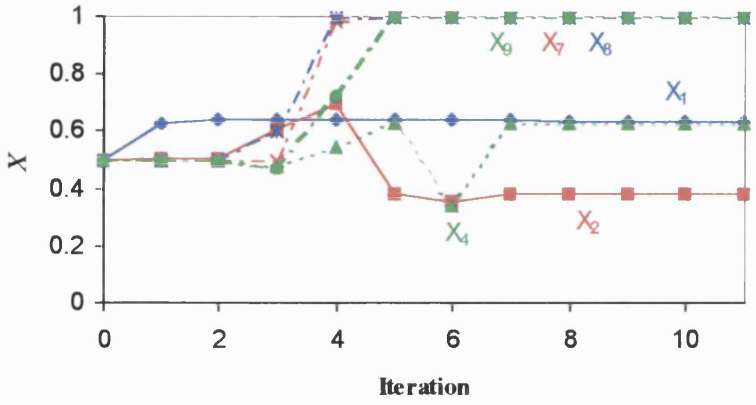

c)

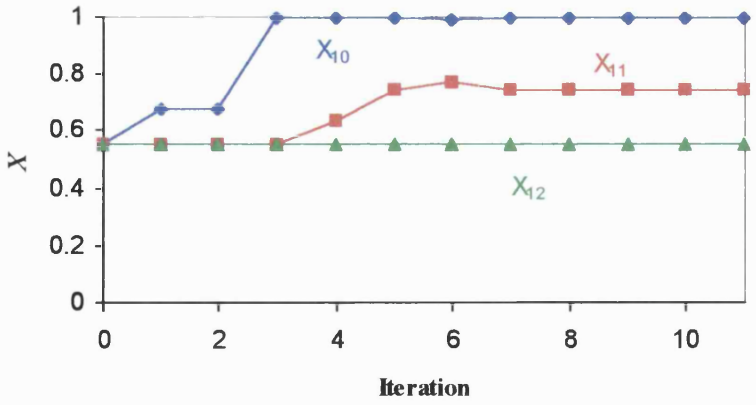

Figure 7.2.1 – Objective function and design variable history for structural characterisation of the undamaged beam

a) Objective function

b) Design variables $X_1 - X_9$ (Not including X_3,X_5 and X_6)

c) Design variables $X_{10} - X_{12}$

To increase the frequencies closer to the experimental values, the Young's modulus in the fibre direction (X_1) had increased, as well the two spring constants in the bending direction, k_h and k_θ (X_{10} and X_{11}). The shear moduli G_{13} and G_{23} (X_8 and X_9), also increased to their upper bounds, increasing the shear rigidity of the 0° and 90° layers. The major Poisson's ratio also increased, increasing stiffness of the laminate, although this effect is small. As there is no bending-torsion coupling for this laminate, it is unclear why G_{12} (X_7) increased. E_3, ν_{23} and ν_{31} (X_3, X_5 and X_6) were unchanged by the optimiser, and are therefore not shown in figure 7.2.1.

Because the experimental torsion modes were not included in the objective function, the torsional spring constant remained unchanged throughout the optimisation. The two springs stiffnesses in the bending directions, however, increased, showing that the clamping arrangement stiffness was sufficient to justify the cantilever beam assumptions. It was therefore decided to use spring constant values of 1×10^9 N/m, 1×10^9 Nm/rad, and 1×10^9 Nm/rad for k_h, k_θ and k_ψ, respectively (effectively cantilever boundary conditions), and carry out the characterisation process again with the spring stiffness values constant.

The initial and final frequencies with the boundary conditions constant are shown in table 7.2.3, showing a better correlation with the experimental frequencies. The final material properties, which were then used in the damage detection phases, are shown in table 7.2.4.

Mode	Initial DSM Frequency [Hz]	Final DSM Frequency [Hz]
1	14.01	14.92
2	87.46	93.16
3	235.86	251.15
4	432.36	460.24

Table 7.2.3 – Initial and final optimiser frequencies and experimental frequencies for the $[0°,90°]_{2,s}$ beam (case 1)

$E_1 = 157.3\times10^9$ Pa	$\nu_{12} = 0.2634$	$G_{12} = 1.071\times10^9$ Pa
$E_2 = 9.694\times10^9$ Pa	$\nu_{23} = 0.263$	$G_{13} = 1.072\times10^9$ Pa
$E_3 = 9.65\times10^9$ Pa	$\nu_{31} = 0.018$	$G_{23} = 5.356\times10^8$ Pa

Table 7.2.4 – Post-characterised material properties for T300/913C Carbon-fibre/epoxy

7.2.2 Damage Detection and Location – Gradient Based Optimisation

Using the characterised material properties, the frequencies and mode-shapes were then used to locate the delaminations using the gradient-based optimisation procedure. Because locating a delamination is a discrete optimisation problem, an optimisation run must be carried out for every ply location, and the minimum objective function used to denote the correct location. To simplify this process, it was decided that the number of possible delaminations would be restricted to one. For the 8-ply laminates used, restricting the number of possible delaminations to one means that the optimiser must be run seven times.

For cases 2 and 3, it was observed that the low number of points used to measure the mode-shapes had caused the mode-shapes to be inaccurate. To ensure that the trend in the mode-shapes due to the delaminations (the increased gradient at the delamination location), was recorded, without incorporating the significant experimental error in the input data, a 4^{th} order polynomial curve-fit was applied to the points. Figure 7.2.2 shows the experimental first bending mode shape for case 2, together with the curve used to smooth the data points. The curve, normalised so that the maximum deflection again equalled 1, was then used to obtain the five input data points, which describe the mode. Cases 5 to 8 had more experimental points, and it was decided that these gave enough resolution that a curve fit was not necessary.

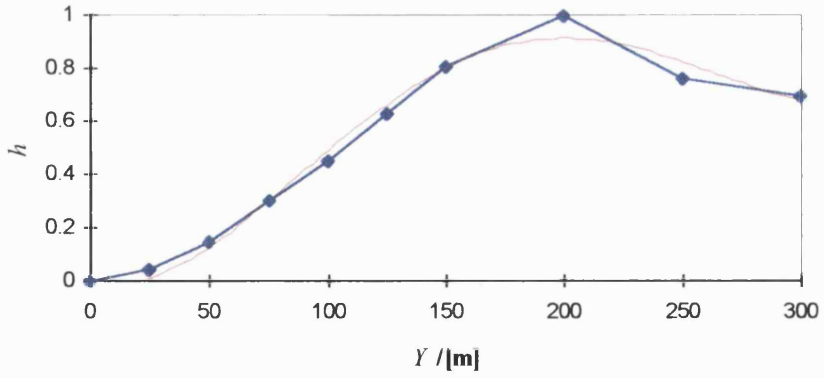

Figure 7.2.2 – Experimental first bending mode and the curve-fit used to describe it

For cases 2,3 and 5-8, and using the new material properties given in table 7.2.4, the gradient-based optimisation method was applied to each layer. To ensure that a global minimum was found for each case, three starting positions were used. These were X_1=0.25, X_2=0.3, X_1=0.5, X_2 =0.3 and X_1=0.75, X_2=0.3. The optimiser control parameters and constants used to derive the objective function were identical to those used for the characterisation stage.

It should be noted that in some cases the gradient-based optimiser procedure had converged to a local minimum, which gave a poor solution to the damage location. For example, figure 7.2.3 shows the two-dimensional design space for Case 2 created by restricting X_3 to 0.5, and the optimiser solutions from the three starting positions. From the three starting positions used, only two have located the global minimum solution.

It is interesting to note that, although only four bending modes were used to create figure 7.2.3, the contour diagram shows the same features as figure 7.1.1, which used the first ten mode shapes. It can be concluded, therefore, that reducing the number of modes has not caused a significant detrimental effect on the optimisation process.

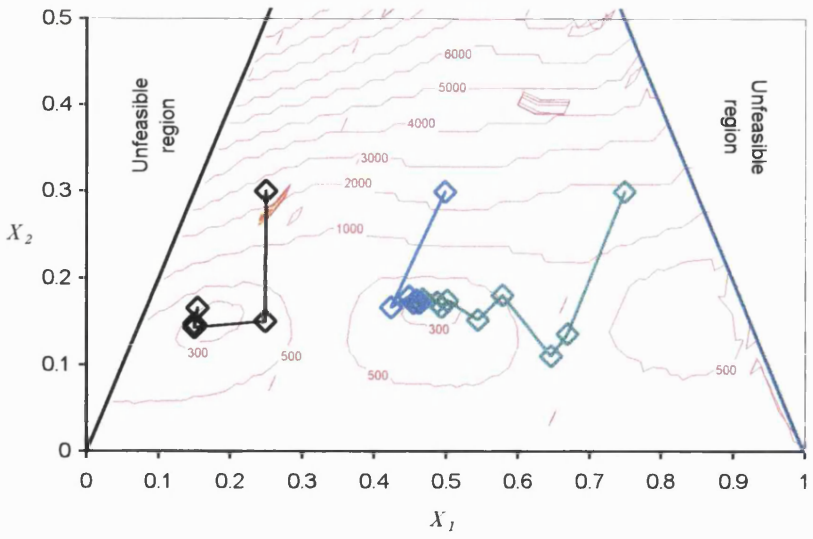

Figure 7.2.3 – 2-Dimensional design space created by a single delamination (Case 2)

Figure 7.2.4 shows the final objective function for optimiser runs at different ply locations for Case 2. The lowest objective function gives the best solution for the damage location, which, for this case has been located correctly at ply location 4 or X_3 =0.5. Figure 7.2.5 shows the history of the design variables and objective function for this solution, which is typical of the results of the gradient-based optimiser. 11 iterations were taken to produce this solution.

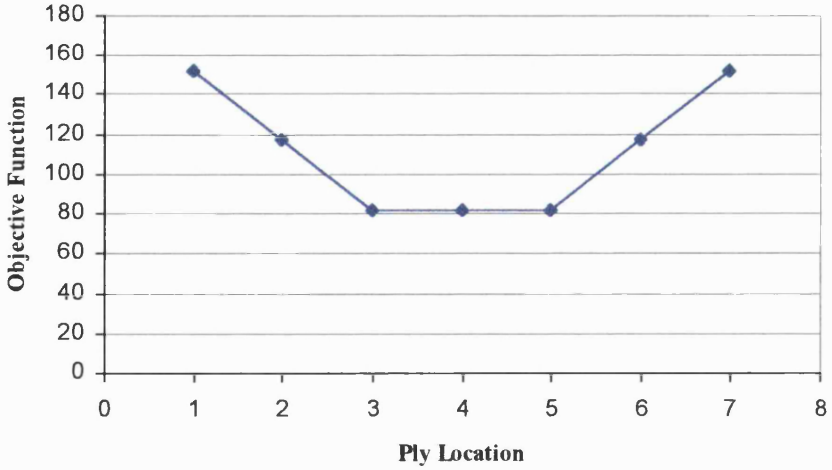

Figure 7.2.4 – Objective function of final optimiser solution for different starting ply positions for Case 2

a)

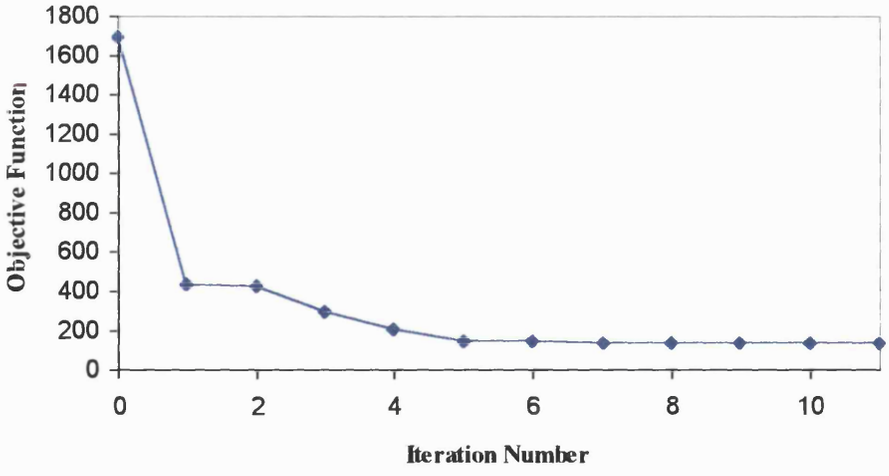

b)

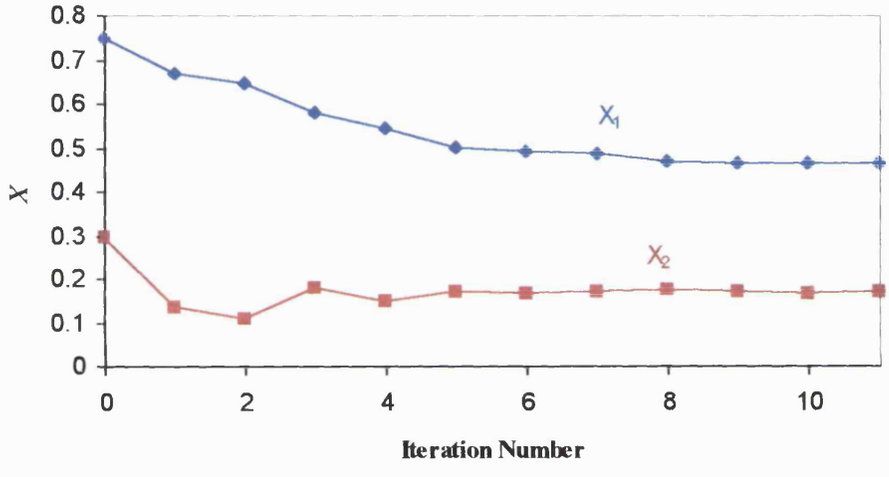

Figure 7.2.5 – Objective function and design variable history for Case 2

a) Objective function

b) Design variables X_1 and X_2

Table 7.2.5 shows the best final solution for each test case, compared to the actual delamination positions. It can be seen that the gradient-based optimiser has performed reasonably well in location the delaminations. Overall, the errors the horizontal location and delamination size remained reasonably low, but the vertical location was not located well. The delamination size was consistently under-estimated for cases 5 to 7, as expected from the relatively lower experimental frequency reductions than for cases 2 and 3. The greater reduction in frequency for

case 8 when compared to case 7, seen in table 6.1.2, has resulted in a larger delamination size being predicted for the former case.

Test Case Number	$\frac{l_a}{l}$	Error /[%]	$\frac{l_d}{l}$	Error /[%]	$\frac{l_b}{d}$	Error /[%]
2	0.465	-5.1	0.173	3.5	0.5	0.0
3	0.693	7.3	0.166	-0.7	0.5	0.0
5	0.405	-17.3	0.113	-32.3	0.125	-75.0
6	0.684	10.3	0.117	-29.9	0.25	-50.0
7	0.144	23.1	0.137	-18.0	0.375	-25.0
8	0.203	73.5	0.230	37.7	0.125	-50.0

Table 7.2.5 – Final optimiser solution of delamination location and size, created by the gradient-based optimiser method

7.2.3 Damage Detection and Location – Genetic Algorithm

Table 7.2.6 shows the best solution of delamination size and location for the experimental damaged beams, produced by the GA. To produce these solutions, a gene containing the three design variables encoded to four decimal places was used, giving a gene of 23 bits in length. The control parameters were; $n_{pop} = 40$, $p_m = 0.001$, and $p_c = 0.8$, and the scaling window was the preceding 5 generations.

It can be seen that in the most cases the GA has resulted in delaminations being located with better accuracy than the gradient-based method. However, it is interesting to note that for cases 3 and 5 the GA has converged to a worse solution than did the gradient-based method. In these cases the gradient-based optimiser had benefited from a local minimum caused by starting very close to its final position. However, the objective function values produced by the GA are lower than those produced by the gradient method, showing that, in fact, the GA solutions are the global ones. For these cases, the optimisation was also run without the mode-shapes influencing the objective function. Much better solutions were found (also shown in table 7.2.6), showing that the errors in the solution were caused by the significant errors inherent in measuring experimental mode shapes.

By sampling the population of designs at each generation, it is possible to record the optimisation as it progresses. Figure 7.2.6 shows the history of the optimisation for Case 2, shown in the form of the best solution, the worst solution, and the average of all the solutions for each generation. Figure 7.2.6 shows that the problem shows fast convergence, with the first occurrence of the best solution seen at the 17th generation. After 40 generations both the best solution and average solution for each generation has converged, with only the maximum value of the objective function varying significantly owing to the mutated genes.

Test Case Number	$\frac{l_a}{l}$	Error /[%]	$\frac{l_d}{l}$	Error /[%]	$\frac{l_b}{d}$	Error /[%]
2	0.466	-4.9	0.173	3.6	0.5	0.0
3	0.649 (0.628)	4.6 (1.3)	0.221 (0.157)	32.3 (-6.0)	0.125 (0.5)	-75.0 (0.0)
5	0.853 (0.391)	74.1 (20.2)	0.111 (0.093)	-33.5 (44.3)	0.375 (0.25)	-25.0 (-50.0)
6	0.777	25.3	0.190	13.8	0.125	-75.0
7	0.120	2.6	0.173	3.6	0.5	0.0
8	0.285	143.6	0.215	28.7	0.125	-50.0

Table 7.2.6 – Final optimiser solution of delamination location and size, created by the GA (Brackets indicate that no mode-shapes were used in the optimisation)

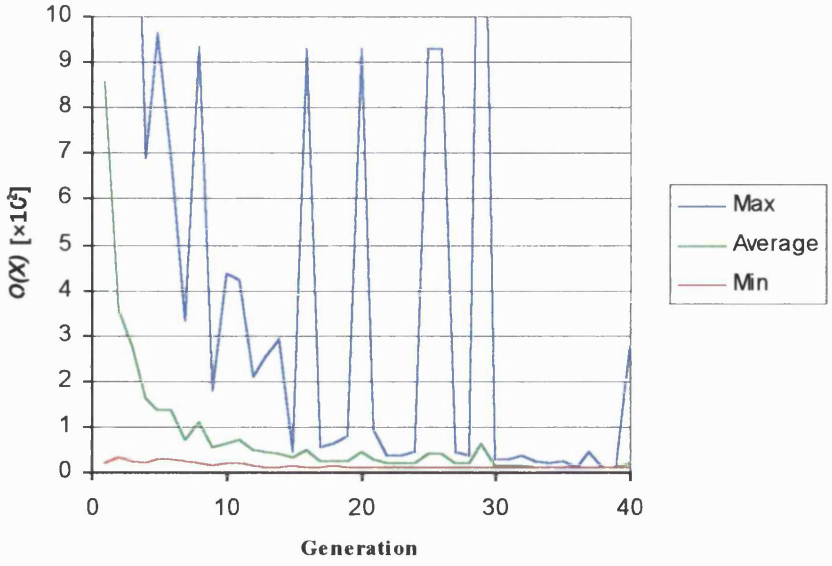

Figure 7.2.6 – Objective function and design variable history for Case 2 produced by the GA

8. Conclusions and Recommendations for Future Work

This chapter summarises the main conclusions of the research, and gives some recommendations for future work that have arisen.

8.1 Conclusions

8.1.1 Validation of the DSM

A series of experiments were carried out to determine the natural frequencies and mode-shapes of composite beams and plates. The results for the undamaged laminates were used as an initial validation, to ensure that the DSM was accurate for the beams used in this thesis.

When the results from the DSM were compared with FE and experimental results for the beams manufactured 'in house', in the most cases, the DSM proved to be accurate. Discounting the modes where known experimental inaccuracies existed, the bending frequencies of the composite beams calculated by the DSM agreed to within 15% of the experimental results. Likewise the MACs showed that the mode-shapes predicted by the DSM agreed well with experiment.

However, the results obtained by the DSM did not agree well for the torsional modes of the beams. Underestimates of up to 73% were seen. This was due to the fact that the beams were very thin in relation to their other dimensions. This caused significant out-of plane strain in the torsional modes, which increased their effective torsional rigidities and therefore their torsional frequencies.

Thicker plates, manufactured by British Aerospace Airbus Ltd., were also tested experimentally. The bending frequencies and mode-shapes also agreed well with those produced by the DSM, but with larger differences between the DSM and experiment due to anti-clastic bending of the experimental plates. The torsional frequencies and mode-shapes also showed good agreement between the DSM and experiment, as the thicker laminates did not display such significant effects of out-of-plane deformation in the torsion modes. The accuracy of the DSM was also unaffected by the different laminate construction of some of the plates.

8.1.2 Validation of the Model of a Delaminated Beam

A simple static model of a delaminated model was developed, which calculated the reduced shear and torsional rigidity of a delaminated beam section. These reduced rigidity terms were used within the DSM to calculated the vibrational behaviour of delaminated beams. This approach was validated with the aid of FE models, and by experiment.

The static beam model was assessed by modelling a delaminated cantilever beam with a tip load using finite elements, and comparing the deflected shape with that produced by the analytical beam model. The FE model of a delaminated beam section agreed well with the static beam model for delaminations causing symmetric sub-laminates to be created. With increasing sub-laminate asymmetry however, the accuracy of the static model reduced.

Vibration results for delaminated beams, calculated by the DSM, showed good agreement with FE models for bending modes. Both showed that a delamination has greatest effect on frequency as it enters a region of high shear stress within a particular mode. It was considered that the approximation of constant shear force along the length of the delamination was satisfactory for small delaminations, although it was recognised that for some locations where for a particular mode-shape the shear force distribution was not constant, and for large delaminations, the reduction in shear rigidity would be inaccurate. The accuracy of the model was seen to reduce with increasing delamination sizes, but remained good for delamination sizes that could be classed as BVID. The model also agreed well with experimental evidence, which was created by inserting thin strips of Teflon during the manufacturing process to create "simulated" delaminations.

The drop in torsional frequency predicted by the model was seen to be too great when compared to FE models. One possible reason was that the model of the torsional deflection of a delaminated beam did not account for the misalignment of the edges of the ends of the sub-laminates when they were twisted. It was thought that including an end-face compatibility condition to remedy this would increase the accuracy of the model.

It was seen that both the size and location of delaminations, in both the Y and Z axes, could potentially be identified by unique reductions in frequency and mode-shape characteristics. The delamination size was the dominant factor in frequency reductions and changes in mode-shapes.

8.1.3 Detection and Location of Delaminations

The dynamic model of a delaminated beam was incorporated into a numerical optimiser to locate the damage. The objective function quantified the difference between the analytically-produced frequencies and mode-shapes, and those obtained by experiment. A two stage process was used. Firstly, the errors in the analytical model were reduced by altering the material properties and boundary conditions of the undelaminated beam model. When this had been achieved, the damage was located using experimental results of damaged beams. Design variables of the number, the size and the location of delaminations could be used. Because of the problems with the model of the torsional behaviour of the beams, only the bending modes of vibration were used to detect the damage. Damage was however successfully located using both a gradient-based optimiser and a GA.

The effectiveness of the NDT procedures was assessed using both analytically-produced input data, and data produced by experiment. The sensitivity of the procedures to experimental errors was assessed by producing a set of input data with a random percentage variation. It was found that the location of the delaminations was more susceptible to error than its size, but that both were tolerant of small errors in frequency and mode-shape measurements.

The gradient-based optimiser successfully located the delaminations produced by experiment but was susceptible to producing locally-minimum solutions. In all damage cases assessed, the gradient-based optimisation method was significantly faster than the GA, although for multiple delaminations the efficiency of the procedure reduces. Therefore, it can be said that the choice of using a gradient-based method or a GA is a trade-off between accuracy and time.

Using either optimiser method, it was found that it is desirable to include as many input frequencies and mode-shapes as possible. However, damage was successfully located using as little as four bending mode frequencies, and the design space is not significantly altered by only using the four modes.

8.2 Recommendations for Further Work

8.2.1 Dynamic Model of a Delaminated Beam

It has been shown that the DSM offers an attractive method of NDT when coupled with an optimising technique, because of its ease of use and relative computational efficiency compared to FE models. The full potential of the DSM has not been realised in this thesis, however, as the reduction of torsional rigidity due to a delamination was not accurately predicted. Further work to correctly model reductions in torsional rigidity, for application in the DSM, would prove beneficial. It is suggested that including an end-face compatibility condition would significantly increase the accuracy of the torsional rigidity prediction.

A further suggestion would be to model a delamination explicitly within the DSM, by offsetting two beams so that they were stacked on top of each other, and were connected to the undelaminated section of the beam at their ends. Ideally, this would use a version of the DSM that included extensional displacement, which would allow bending-extension coupling. This would offer a greatly increased accuracy over the reduced shear and torsional rigidity approximation used in this research.

8.2.2 Optimisation

During investigation of the optimisation methods, it was found that the gradient-based optimiser located delaminations significantly faster than the GA. However, because the design space was relatively complex, a local minimum could be found is if the optimisation was started at a location far from the global optimum. This suggests a combined optimisation technique. Using a small number of generations, the GA could be used to find a starting position that was close to the global optimum. Then, because the design space is locally smooth, the gradient-based method could be used to converge to the global solution using this starting position. This would ensure a global solution without expending too much computer time.

8.2.3 Applications

The research presented herein has been an initial investigation into non-destructive testing using the DSM, and encouraging results have been obtained in terms of computer efficiency compared to FE models. For this to become a useful application, the structural model should be developed to be more representative of structures used in industrial applications.

Modelling a wing or rotor blade as a whole, work has already been carried out using the DSM to represent wing box structures. The static model could be further developed to include the reduction in effective bending rigidity due to the drop in axial stiffness of the top or bottom wing surface. Together with the reduction in shear rigidity due to the delamination, the effect on frequencies and mode-shapes could be predicted.

Much of the outer structure of an aircraft can be thought of as a number of inter-connected plate-like structures. An example is the wing skin of an aircraft, which is divided into plate-like sections by the wing ribs along its length, and the wing spars along its chord.

A small step to modelling delaminations in plates would be to model delaminations that did not extend the whole width of the beam, as delaminations in plates rarely extend to either edge unless their dimensions are small, and would be in any case relatively easy to detect manually. It may be possible to model the effect of non full-width delaminations with a simple rule-of-mixtures type approach using the values calculated in this thesis, but further investigation would be necessary to confirm this.

Work has already been carried out to model plates with the DSM. The work in this thesis could be further extended to model stiffness reductions due to delaminations in composite plates, and incorporate them into the plate DSM. The reductions in stiffness would be smaller than those obtained in this research, due to the fact that the delaminations could not be assumed to be full-width, and this has been verified by experiment in this research. However, if the reductions in frequency were enough to be detectable, significant accuracy may be obtained when modelling the individual wing panels rather than the wing as a whole.

References

Abarcar, R.B., Cunniff, P.F., "The Vibration of Cantilever Beams of Fiber Reinforced Material", *Journal of Composite Materials*, Vol. 6, 1972, pp. 504-516

Araujó, A.L., Mota Soares, C.M., Moreira de Freitas, M.J., "Characterization of Material Parameters of Composite Plate Specimens Using Optimization and Experimental Vibrational Data", *Composites: Part B,* Vol. 27B, 1996, pp. 185-191

Adams, R.D., Brownjohn, J.M.W., Cawley, P., "The Detection of Defects in GRP Lattice Structures by Vibration Measurements", *NDT&E Inernational*, Vol. 24, No. 3, 1991, pp. 123-133

Almond, D.P., Delpech, P., Beheshtey, M.H., Peng, W., "Quantitative Determination of Impact Damage and Other Defects in Carbon Fiber Composites by Transient Thermography", *SIPE*, Vol. 2944, 1996, pp. 256-264

Ashley, H., "On Making Things Best – Aeronautical Uses of Optimisation", *Journal of Aircraft*, Vol. 19, No. 1, 1982, pp. 5-25

Averill, R.C., "Static and Dynamic Response of Moderately Thick Laminated Beams with Damage", *Composites Engineering*, Vol. 4, No. 4, 1994, pp. 381-395

Ball, R.J., Almond, D.P., "The Detection and Measurement of Impact Damage in Thick Carbon Fibre Reinforced Laminates by Transient Thermography", *NDT&E International*, Vol. 31, No. 3, 1998, pp. 165-173

Banerjee, J.R., "Coupled Bending-Torsional Dynamic Stiffness Matrix for Beam Elements", *International Journal for Numerical Methods in Engineering*, Vol. 28, 1989, pp. 1283-1298

Banerjee, J.R., Guo, S., Howson, W.P., "Exact Dynamic Stiffness Matrix of a Bending-Torsion Coupled Beam Including Warping", *Computers and Structures,* Vol. 59, No. 4, 1996, pp. 613-621

Banerjee, J.R., Williams, F.W., "Free Vibration of Composite Beams - an Exact Method Using Symbolic Computation", *Journal of Aircraft*, Vol. 32, No. 3, 1995, pp. 636-642

Banerjee, J.R., Williams, F.W., "Exact Dynamic Stiffness Matrix for Composite Timoshenko Beams with Applications", *Journal of Sound and Vibration*, Vol. 194, No. 4, 1996, pp. 573-585

Banks, H.T., Inman, D.J., Leo, D.J., Wang, Y., "An Experimentally Validated Damage Detection Theory in Smart Structures", *Journal of Sound and Vibration*, Vol. 191, No. 5, 1996, pp. 859-880

Bartkowicz, T.J., Kim, H.M., Zimmerman, D.C., Weaver Smith, S., "Autonomous Structural Health Monitoring System: A Demonstration", *37th AIAA Conference*, Salt Lake City, Utah, USA, 1996

Baruh, H., Ratan, S., "Damage Detection in Flexible Structures", *Journal of Sound and Vibration*, Vol. 166, No., 1 1993, pp. 21-30

Boller, C., "Parameters and Techniques Based on Piezoelectric Sensing for Monitoring the Integrity of Composite Structures", *5th International Conference on Adaptive Structures*, Sendal, Japan, 1994

Boller, C., Meinel, H.H., Brand, W., "Smart Structures and Materials – A Selection of DASA Views", *NATO Workshop on Smart EM Antenna Structures*, Brussels, Belgium, 1996

Braggiotti, A., Marinetti, S., Mazzoldi, A., "D2D: A Robust Transient Thermography NDT Technique for Real Time In-Field Measurements", *SPIE*, Vol. 3397, 1998, pp. 149-154

Butler, R., "The Optimisation of Wing Structures – Theory or Practice?", *Aircraft Engineering and Aerospace Technology*, Vol. 70, No. 1, 1998, pp. 4-8

Butler, R., Banerjee, J.R., "Optimum Design of Bending-Torsion Coupled Beams with Frequency or Aeroelastic Constraints", *Computers and Structures*, Vol. 60, No. 5, 1996, pp. 715-724

Butler, R., Lillico, M., Banerjee, J.R., Guo, S., "Optimum Design of High Aspect Ratio Wings Subject to Aeroelastic Constraints", *36th AIAA/ASME/ASCE/AHS/ASC Structures, Structural Dynamics And Materials Conference*, New Orleans, L.A., 1995, pp. 558-566

Casas, J.R., Aparicio, A.C., "Structural Damage Identification from Dynamic-Test Data", *Journal of Structural Engineering,* Vol. 120, No. 8, 1994, pp. 2437-2450

Cawley, P., Adams, R.D., "A Vibration Technique for Non-Destructive Testing of Fibre Composite Structures", *Journal of Composite Materials*, Vol. 13, 1979, pp. 161-175

Chai, G.B., Chin, S.S., Lim, T.M., Hoon, K.H., "Vibration Analysis of Laminated Composite Plates: TV-Holography and Finite Element Method", *Composite Structures*, Vol. 23, 1993, pp. 273-283

Chan, W.S., Chou, C.J., "Effects of Delamination and Ply Fiber Waviness on Effective Axial and Bending Stiffness in Composite Laminates", *Composite Structures*, Vol. 30, 1995, pp. 299-306

Christensen, R.M., "Mechanics of Composite Materials", *John Wiley & Sons Inc.,* New York, USA, 1979

Cobb, R.G., Liebst, B.S., "Structural Damage Identification Using Assigned Partial Eigenstructure", *AIAA Journal*, Vol. 35, No. 1, 1997, pp. 152-158

Crawley, E.F., "Intelligent Structures for Aerospace: A Technology Overview and Assessment", *AIAA Journal*, Vol. 32. No. 8, 1994, pp. 1689-1698

Cox, R.P., "Experimental Assessment of Impact Damage to Composite Structures", University of Bath Internal Report, 1999

Data Physics Corporation, "Making Measurements with SignalCalc Ace", San Jose, CA,USA, 1999

Davies, G.A.O., "Aircraft Structures", *Aeronautical Journal,* Vol. 100, No. 1000, 1995, pp. 523-530

Davies, G.A.O., Hitchings, D., Zhou, G., "Impact Damage and Residual Strengths of Woven Fabric Glass/Polyester Laminates", *Composites Part A*, Vol. 27A, 1996, pp. 1147-1156

Delmonte, J., "Technology of Carbon and Graphite Fiber Composites", *Litton Educational Publishing, Inc.*, New York, USA, 1981

Donne, M.S., Tilley, D.G., Richards, W., "The Use of Multi-Objective Parallel Genetic Algorithms to Aid Fluid Power System Design", *Proceedings of the Institute of Mechanical Engineers Part 1: Journal of Systems and Control Engineering*, Vol. 209, 1995, pp. 53-61

Ewins, D.J., "Modal Testing: Theory and Practice", *Research Studies Press Ltd.*, Taunton, UK, 1984

Farag, N.H., Pan, J., "Free and Forced In-Plane Vibration of Rectangular Plates", *Journal of the Acoustical Society of America,* Vol. 103, No. 1, 1998, pp. 408-413

Findeis, D., Gryzagoridis, J., "Non Destructive Testing of Composites Using Portable Laser Based Methods", *Sixth International Conference on Composites Engineering*, Orlando, USA, 1999, pp. 221-222

Forsyth, D.S., Komorowski, J.P., Gould, R.W., "The Use of Solid Film Highlighter in Automation of D Sight Image Interpretation", *SPIE*, Vol. 3397, 1998, pp. 50-56

Friswell, M.I., Inman, D.J., Pilkey, D.F., "Direct Updating of Damping and Stiffness Matrices", *AIAA Journal*, Vol. 36, No. 3, 1997, pp. 491-493

Gandelrab, R.M., "The Effect of Delamination on the Natural Frequencies of a Laminated Composite Beam", *Journal of Sound and Vibration*, Vol. 197, No. 3, 1996, pp. 283-292

Garrett, R., "Effect of Manufacturing Defects and Service-Induced Damage on the Strength of Aircraft Composite Structures", *Composite Materials: Testing and Design (Seventh Conference),* Philadelphia, USA, 1986, pp. 5-33

Gere, G.M., Timoshenko, S.P, "Mechanics of Materials", *PWS-Kent Publishing Co.,* Boston, USA, 1984

Ghostal, A., Sundaresan, M.J., Schulz, M.J., Frank Pai, P., "Damage Detection in Composite Structures Using Vibration Measurements", *Sixth International Conference on Composites Engineering*, Orlando, USA, 1999, pp. 245-246

Goldberg, D.E., "Genetic Algorithms in Search, Optimization and Machine Learning", *Addison Wesley Longman, Inc.,* Reading, USA, 1989

Goto, A., Yokoyama, A., "Applications of Genetic Algorithm on Laminated Constitutions of Hybrid Composites with Vibration Damping Properties", *Sixth International Conference on Composites Engineering*, Orlando, USA, 1999, pp. 263-264

Grefenstette, J.J., "A User's Guide to GENESIS", 1990

Gundtoft, H.E., Borum, K.K., "Characterization of Composites by Ultrasonic-Scanning. Examples and Experience from Participation in European and National Projects", *Sixth International Conference on Composites Engineering*, Orlando, USA, 1999, pp. 273-274

Hajela, P., Soeiro, F.J., "Structural Damage Detection Based on Static and Modal Analysis", *AIAA Journal*, Vol. 28, No. 6, 1990, pp. 1110-1115

Harrison, C., Butler, R., "The Modelling of Delaminations in Vibrating Composite Beams", *Sixth International Conference on Composites Engineering*, Orlando, USA, 1999, pp. 299-300

Harrison, C., Butler, R., "Locating Delaminations in Composite Beams Using Gradient Techniques and a Genetic Algorithm", *To appear in Proceedings of 8th AIAA/USAF/NASA/ISSMO Symposium on Multidisciplinary Analysis and Optimization*, Long Beach, USA, 2000 (and to be submitted to AIAA Journal)

Hassiotis, S., Jeong, G.D., "Assessment of Structural Damage from Natural Frequency Measurements", *Computers and Structures*, Vol. 49, No. 4, 1993, pp. 679-691

Hassiotis, S., Jeong, G.D., "Identification of Stiffness Reductions Using Natural Frequencies", *Journal of Engineering Mechanics*, Vol. 121, No. 10, 1995, pp. 1106-1113

Hull, D., Shi, Y.B., "Damage Mechanism Characterization in Composite Damage Tolerance Investigations", *Composite Structures*, Vol. 23, 1993, pp. 99-120

Ip, K-H., Tse, P-C., "Accuracy of the Characterized Young's and Shear Moduli of Composite Beams using Flexural Vibration Frequencies", *Sixth International Conference on Composites Engineering*, Orlando, USA, 1999, pp. 355-356

Kapania, R.K., Lovejoy, A.E., "Free Vibration of Thick Generally Laminated Cantilever Quadrilateral Plates", *AIAA Journal*, Vol. 34, No. 7, 1996, pp. 1474-1486

Kelly, A., "Concise Encylopedia of Composite Materials", *Elsevier Science Ltd.*, Kidlington, UK, 1994

Krawcruk, M., Ostachowicz, W., "Dynamics of Cracked Composite Material Structures", *Computational Mechanics*, Vol. 20, 1997, pp. 79-83

Lou, H., Hanagud, S., "Dynamic Learning Rate Neural Network Training and Composite Structural Damage Detection", *AIAA Journal*, Vol. 35, No. 9, 1997, pp. 1522-1527

Larsson, P.O., "Determination of Young's and Shear Moduli from Flexural Vibrations of Beams", *Journal of Sound and Vibration*, Vol. 146, No. 1, 1991, pp. 111-123

Lestari, W., Lu, X., Hanagud, S., "Dynamics of a Delaminated Beam: Effects of Nonlinearity", *41st AIAA/ASME/ASCE/AHS/ASC Structures, Structural Dynamics, and Materials Conference*, Atlanta, Georgia, USA, 2000

Lillico, M., Butler, R., Banerjee, J.R., Guo, S., "Aeroelastic Optimization of High Aspect Ratio Wings Using an Exact Dynamic Stiffness Matrix Method", *The Aeronautical Journal*, Vol. 101, No. 1002, 1997, pp 77-86

Lou, H., Hanagud, S., "Delaminated Beam Nonlinear Dynamic Response Calculation and Visualization", *28th AIAA/ASME/ASCE/AHS/ASC Structures, Structural Dynamics and Materials Conference*, Kissimmee, Florida, USA, 1997, pp. 490-499

McIntyre, M.E., Woodhouse, J., "On Measuring the Elastic and Damping Constants of Orthotropic Sheet Materials", *Acta Metallica*, Vol. 36, No. 6, 1988, pp. 1397-1416

Mouritz, A.P., Leong, K.H., Herszberg, I., "A Review of the Effects of Stiching on the In-plane Mechanical Properties of Fibre-Reinforced Polymer Composites", *Composites Part A*, Vol. 28A, pp. 979-991, 1997

Mujumdar, P.M., Suryanarayan, S., "Flexural Vibrations of Beams with Delaminations", *Journal of Sound and Vibration*, Vol. 125, No. 3, 1988, pp. 441-461

O'Brien, T.K., "Analysis of Local Delaminations and Their Influence on Composite Laminate Behaviour", Delamination and Debonding of Materials, *American Society for Testing and Materials*, Philadelphia, 1985, pp. 282-297

O'Brien, T.K., Reifsnider, K.L., "Fatigue Damage: Stiffness/Strength Comparisons for Composite Materials", *Journal of Testing and Evaluation*, Vol. 5, No. 5, 1977, pp. 384-393

Okafor, A.C., Chandrashekhara, K., Jiang, Y.P., "Damage Detection in Composite Laminates with Built-in Piezoelectric Devices using Modal Analysis and Neural Network", *SPIE*, Vol. 2444, 1995, pp. 314-325

Pandey, A.K., Biswas, M., Samman, M.M., "Damage Detection from Changes in Curvature Mode Shapes", *Journal of Sound and Vibration*, Vol. 145, No. 2, 1991, pp. 321-332

Quagliarella, D., Della Cioppa, A., "Genetic Algorithms Applied to the Aerodynamic Design of Transonic Airfoils", *Journal of Aircraft*, Vol. 32., No. 4, 1999, pp. 889-891

Ramkumar, R.L., Kulkarni, S.V., Pipes, R.B., "Free Vibration Frequencies of a Delaminated Beam", *34th Annual Technical Conference, The Society of the Plastics Industry*, Sect. 22E, 1979 pp. 1-5

Ratcliffe, C.P., "Damage Detection Uaing a Modified Laplacian Operator on Mode Shape Data", *Journal of Sound and Vibration,* Vol. 204, No. 3, 1997, pp. 505-517

Ratcliffe, C.P., Bagaria, W.J., "Vibration Technique for Locating Delamination in a Composite Beam", *AIAA Journal,* Vol. 36, No. 6, 1994, pp. 1074-1077

Ruotolo, R., Surace, C., "Damage Assessment for a Beam with Multiple Cracks", *19th International Seminar on Modal Analysis,* Leuven, 1996

Ruotolo, R., Surace, C., "Damage Assessment of Multiple Cracked Beams: Numerical Results and Experimental Validation", *Journal of Sound and Vibration,* Vol. 206, No. 4, 1997, pp. 567

Ryder, G.H., "Strength of Materials", *Macmillan and Co. Ltd.,* London, England, 1969

Saravanos, D.A., Birman, V.B., Hopkins, D.A., "Detection of Delaminations in Composite Beams Using Piezoelectric Sensors", *AIAA Journal,* 199, pp. 181-191

Sensburg, O., "Damage Detection of Aircraft Structures Using Dynamic Analysis and Testing Methods", PhD, *University of Manchester,* 1993

Shelby, M.D., Tai, H.J., Jang, B.Z., "Vibration Based Non-Destructive Evaluation of Polymer Composites", *Polymer Engineering and Science,* Vol. 31, No. 1, 1991, pp. 47-55

Shen, M-H.H., Grady, J.E., "Free Vibrations of Delaminated Beams", *AIAA Journal,* Vol. 30, No. 5, 1992, pp. 1361-1370

Shen, J.Y, Sharpe Jr., L., Jankovsky, A.L., "An Overview of Vibrational-Based Nondestructive Evaluation Techniques", *SPIE,* Vol. 3397, 1998, pp. 117-127

Shi, Y.B., Hull, D., "Fracture of Delaminated Unidirectional Composite Beams", *Journal of Composite Materials,* Vol. 26, No. 15, 1992, pp. 2172-2195

Shim, P.Y., Manoochehri, S., "Generating Optimal Configurations in Structural Design Using Simulated Annealing", *International Journal for Numerical Methods in Engineering,* Vol. 40, 1997, pp. 1053-1069

Smith, R.E., "Ultrasonic Elastic Constants of Carbon Fibers and Their Composites", *Journal of Applied Physics*, Vol. 43, No. 6, 1972, pp. 2555-2560

Soutis, C., Curtis, P.T., "Prediction of the Post-Impact Compressive Strength of CFRP Laminated Composites", *Composites Science and Technology*, Vol. 56, 1996, pp. 677-684

Spectral Dynamics Inc., "STAR System Users Guide", San Jose, CA, USA, 1994

Swanson Analysis Systems Inc., "ANSYS User Manual", Version 5, Houston, USA, 1992

Takahashi, S., Obayashi, S., Nakahashi, K., "Inverse Design Optimization of Transonic Wings Based on Multi-Objective Genetic Algorithms", *AIAA Journal*, Vol. 37, No. 12, 1999, pp. 1656-1662

Taylor, J.M., "Optimisation and Validation of Frequency Constrained Composite Wings", PhD, *University of Bath*, 1998

Taylor, J.M., Butler, R., "Optimum Design and Validation of Flat Composite Beams Subject to Frequency Constraints", *AIAA Journal*, Vol. 35, No. 3, 1997, pp. 540-545

Taylor, J.M., Butler, R., Harrison, C., "Optimisation of Composite Wind-Tunnel Wing Models for Frequency, Flutter and Divergence", The Aeronautical Journal, Vol. 103, No. 1020, 1999, pp. 105-111

Teh, K.K., Huang, C.C., "The Effects of Fibre Orientation on Free Vibrations of Composite Beams", *Journal of Sound and Vibration*, Vol. 69, No. 2, 1980, pp. 327-337

Tenek, L.H., Henneke II, E.G., Gunzburger, M.D., "Vibration of Delaminated Composite Plates and Some Applications to Non-Destructive Testing", *Composite Structures*, Vol. 23, 1993, pp.253-262

Teoh, L.S., Huang, C.C., "The Vibration of Fibre Reinforced Material", *Journal of Sound and Vibration*, Vol. 51, No. 4, 1977, pp. 467-473

Ting, T., Chen, T.L.C., Twomey, W., "Correlating Mode Shapes Based on the Modal Assurance Criterion", *Finite Elements in Analysis and Design*, Vol. 14, 1993, pp. 353-360

Tracy, J.J., Dimas, D.J., Pardoen, G.C., "The Effect of Impact Damage on the Dynamic Properties of Laminate Composite Plates", *Fifth International Conference on Composite Materials,* San Diego, CA, USA, 1985

Tracy, J.J., Pardoen, G.C., "Effect of Delamination on the Natural Frequencies of Composite Laminates", *Journal of Composite Materials,* Vol. 29, 1989, pp. 1200-1215

Tsai, W., Hahn, H.T., "Introduction to Composite Materials", *Technomic Publishing Co. Inc.*, Westport, USA, 1980

Vanderplaats Research & Development, Inc., "DOT Users Manual", Version 4.2, Colorado Springs, USA, 1995

Vantomme, J., "Evaluation of Structural Joints in Composites with Modal Parameters", *Composite Structures*, Vol. 22, 1992, pp. 201-205

Wang, J.T.S., Liu, Y.Y., Gibby, J.A., "Vibrations of Split Beams", *Journal of Sound and Vibration*, Vol. 84, No. 4, 1982, pp. 491-502

Weisshaar, T.A., Foist, B.L., "Vibration Tailoring of Advanced Composite Lifting Surfaces", *Journal of Aircraft*, Vol. 22, No. 2, 1985, pp. 141-147

Williams, E.J., Messina, A., Payne, B.S., "A Frequency-Change Correlation Approach to Damage Detection", *15th International Modal Analysis Conference IMAC*, Vol. 1, Orlando, USA, 1997, pp. 652-657

Williams, F.W., Kennedy, D., Butler, R., Anderson, M.S., "VICONOPT: Program for Exact Vibration and Buckling Analysis or Design of Prismatic Plate Assemblies", *AIAA Journal*, Vol. 29, No. 11, 1991, pp. 1927-1928

Williams, F.W., Wittrick, W.H., "Exact Buckling and Frequency Calculations Surveyed", *Journal of Structural Engineering, American Society of Civil Engineers*, Vol. 109, 1983, pp. 169-183

Wittrick, W.H, Williams, F.W., "A General Algorithm for Computing Natural Frequencies of Elastic Structures", *Quarterly Journal of Mechanics and Applied Mathematics*, Vol. 24, Part 3, 1971, pp. 263-284

Yin, W.L., Jane, K.C., "Vibration of a Delaminated Beam-Plate Relative to Buckled States", *Journal of Sound and Vibration,* Vol. 156, No. 1, 1992, pp. 125-140

Zak, A., Krawczuk, M., Ostachowicz, "Modal Analysis of a Delaminated Composite Plate with Opening and Closing Effects", *Sixth International Conference on Composites Engineering*, Orlando, USA, 1999, 937-938

Zaslavsky, A., "On the Limitations of the Shearing Stress Formula", *IJMEE*, Vol. 8, No. 1, 1980, pp 13-19

Zhou, G., Davies, G.A.O, "Characterization of Thick Glass Woven Roving/Polyester Laminates: 1. Tension, Compression and Shear", *Composites*, Vol. 26, 1995, pp. 579-586

Zhou, G., Davies, G.A.O, "Characterization of Thick Glass Woven Roving/Polyester Laminates: 2. Flexure and Statistical Considerations", *Composites*, Vol. 26, 1995, pp. 587-596

Ziehl, P.H., Fowler, T.J., "Use of Accoustic Emission to Determine Damage Initiation of Fiber Reinforced Polymers", *Sixth International Conference on Composites Engineering*, Orlando, USA, 1999, pp. 957-958

Appendix A - Static Beam Model of a Delaminated Beam Section with Multiple Delaminations: Shear Rigidity

In chapter 2, the method for determining a value for the effective shear rigidity of a beam with a single delamination was presented. This appendix extends the analysis for n-1 delaminations, giving n sub-laminates. The analysis takes the same form as outlined in chapter 2, but as well as a general solution for the ith laminate being obtained, a more rigorous proof is applied to justify some of the assumptions made.

Equilibrium

Figure A2 shows the free body diagram for the delaminated cantilever beam in figure 2.3.1, but with n-1 delaminations. Resolving horizontally at point 2, and assuming $P_2 = 0$, gives:

$$\sum_{i=1}^{n} P_{i_2} = 0 \qquad \text{... (A1)}$$

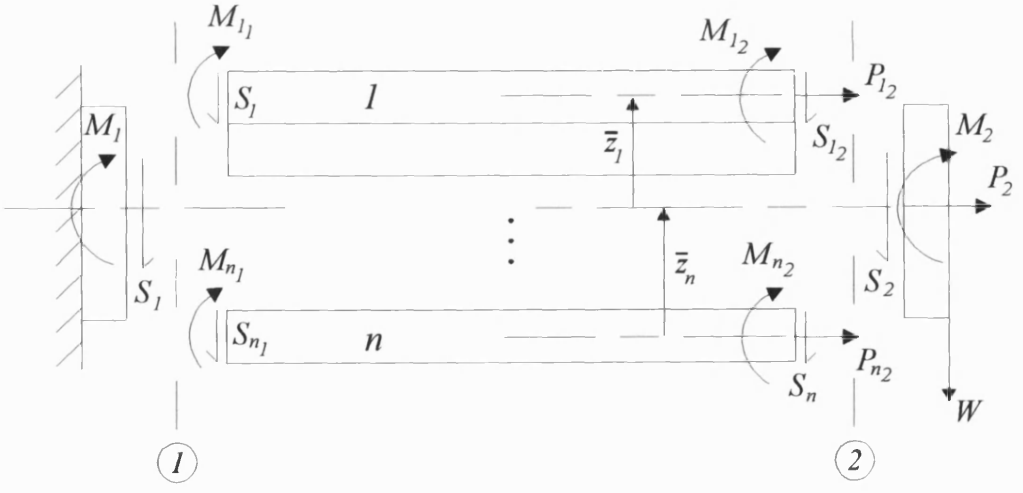

Figure A1 - Free body diagram of the delaminated beam showing forces and moments acting on each sub-laminate.

Taking moments about the neutral axis of the undelaminated laminate for points 1 and 2, with the knowledge that the bending moment varies linearly with y, gives:

$$\sum_{i=1}^{n} M_{i_1} + \sum_{i=1}^{n} P_{i_2} \bar{z}_i = M_1 \qquad \ldots \text{(A2)}$$

$$\sum_{i=1}^{n} M_{i_1} - \sum_{i=1}^{n} S_i l_d + \sum_{i=1}^{n} P_{i_2} \bar{z}_i = M_1 - S l_d \qquad \ldots \text{(A3)}$$

Deflection and Gradient Compatability

Using simple bending theory, the deflection and gradient of each sub-laminate is:

$$v'_{i_{y=l_d}} = -\frac{M_{i_1} l_d}{(EI)_i} + \frac{S_i l_d^2}{2(EI)_i} + K_{BA_i} P_{i_2} l_d \qquad \ldots \text{(A4)}$$

$$v_{i_{y=l_d}} = -\frac{M_{i_1} l_d^2}{2(EI)_i} + \frac{S_i l_d^3}{6(EI)_i} + \frac{K_{BA_i} P_{i_2} l_d^2}{2} \qquad \ldots \text{(A5)}$$

$$i = 1 \ldots n$$

Equating the gradients of each sub-laminate at $y=l_d$ gives:

$$-\frac{M_{i_1}}{(EI)_i} + \frac{S_i l_d}{2(EI)_i} + K_{BA_i} P_{i_2} = -\frac{M_{j_1}}{(EI)_j} + \frac{S_j l_d}{2(EI)_j} + K_{BA_j} P_{j_2} \qquad \ldots \text{(A6)}$$

$$i = 1 \ldots n, j = 1 \ldots n$$

And similarly equating the deflections and the end of each sub-laminate:

$$-\frac{M_{i_1}}{(EI)_i} + \frac{S_i l_d}{3(EI)_i} + K_{BA_i} P_{i_2} = -\frac{M_{j_1}}{(EI)_j} + \frac{S_j l_d}{3(EI)_j} + K_{BA_j} P_{j_2} \qquad \ldots \text{(A7)}$$

$$i = 1 \ldots n, j = 1 \ldots n$$

Therefore, using equations (A6) and (A7), the relationships between S_i and S_j, and M_i and M_j ($i=1 \ldots n$, $j=1 \ldots n$), can be derived:

$$M_{i1} = (EI)_i \left[\frac{M_{j_1}}{(EI)_j} + K_{BA_i} P_{i2} - K_{BA_j} P_{j_2} \right] \qquad \ldots \text{(A8)}$$

$$i = 1 \ldots n, j = 1 \ldots n$$

$$S_i = \frac{(EI)_i}{(EI)_j} S_j \qquad i = 1...n, j = 1...n \qquad \text{... (A9)}$$

Using equations (A2), (A3) and (A9), an equation for the shear force acting on any sub-laminate can be found:

$$S_j = \frac{(EI)_j S}{\sum_{i=1}^{n} (EI)_i} \qquad j = 1...n \qquad \text{... (A10)}$$

Sub-Laminate End Face Compatibility

Figure A2 shows the end-faces of any two neighbouring sub-laminates within the beam. At the end of the delaminated beam, the faces of each sub-laminate must be aligned. As in equations (2.3.15) and (2.3.16), the distance each sub-laminate must strain is dependent upon the gradient at their ends, giving:

$$\frac{P_{i+1_2} l_d}{(EA)_{i+1}} = \frac{P_{i_2} l_d}{(EA)_i} + \left(\bar{z}_i - \bar{z}_{i+1}\right) v'_{i_{y=l_d}} \qquad i = 1...n \qquad \text{... (A11)}$$

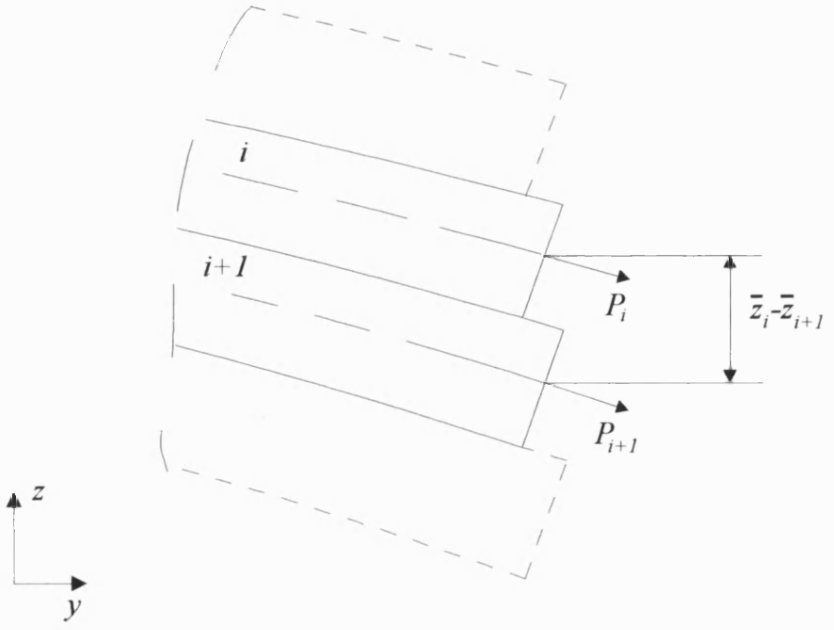

Figure A2 - End faces of two sub-laminates *i* and *i*+1, showing difference in lengths due to gradient

Therefore, from equations (A11) and (A4):

$$\frac{P_{i+1_2}}{(EA)_{i+1}} = \frac{P_{i_2}}{(EA)_i} + (\bar{z}_i - \bar{z}_{i+1})\left[-\frac{M_{i_1}}{(EI)_i} + \frac{S_i l_d}{2(EI)_i} + K_{BA_i} P_{i_2}\right] \quad \text{... (A12)}$$

$$i = 1 \ldots n$$

By inspection of equation (A12), is it assumed that:

$$\frac{P_{i_2}}{(EA)_i} = \frac{P_{j_2}}{(EA)_j} + (\bar{z}_j - \bar{z}_i)\left[-\frac{M_{j_1}}{(EI)_j} + \frac{S_j l_d}{2(EI)_j} + K_{BA_j} P_{j_2}\right] \quad \text{... (A13)}$$

$$i = 1 \ldots n, j = 1 \ldots n$$

This assumption is proven by the method of induction.

Equation (A13) can be re-written as:

$$\frac{P_{i_2}}{(EA)_i} = \frac{P_{i-j_2}}{(EA)_{i-j}} + (\bar{z}_{i-j} - \bar{z}_i)\left[-\frac{M_{i-j_1}}{(EI)_j} + \frac{S_{i-j} l_d}{2(EI)_{i-j}} + K_{BA_{i-j}} P_{i-j_2}\right] \quad \text{... (A14)}$$

$$i = 1 \ldots n, j = 1 \ldots n$$

When j=1, equation (A14) becomes:

$$\frac{P_{i_2}}{(EA)_i} = \frac{P_{i-1_2}}{(EA)_{i-1}} + (\bar{z}_{i-1} - \bar{z}_i)\left[-\frac{M_{i-1_1}}{(EI)_{i-1}} + \frac{S_{i-1} l_d}{2(EI)_{i-1}} + K_{BA_{i-1}} P_{i-1_2}\right]$$

$$i = 1 \ldots n$$

which is equivalent to equation (A12). Assuming (A14) is true for j=a, or:

$$\frac{P_{i_2}}{(EA)_i} = \frac{P_{i-a_2}}{(EA)_{i-a}} + (\bar{z}_{i-a} - \bar{z}_i)\left[-\frac{M_{i-a_1}}{(EI)_{i-a}} + \frac{S_{i-a} l_d}{2(EI)_{i-a}} + K_{BA_{i-a}} P_{i-a_2}\right] \quad \text{... (A15)}$$

$$i = 1 \ldots n$$

From equation (A12):

$$\frac{P_{(i-a)_2}}{(EA)_{(i-a)}} = \frac{P_{(i-a)-1_2}}{(EA)_{(i-a)-1}} + \left(\bar{z}_{(i-a)-1} - \bar{z}_i\right)\left[-\frac{M_{(i-a)-1_1}}{(EI)_{(i-a)-1}} + \frac{S_{(i-a)-1}l_d}{2(EI)_{(i-a)-1}} + K_{BA(i-a)-1}P_{(i-a)-1_2}\right]$$

$$i = 1...n$$

If this is substituted into equation (A15), and using equation (A7), this gives:

$$\frac{P_{i_2}}{(EA)_i} = \frac{P_{i-(a+1)_2}}{(EA)_{i-(a+1)}} + \left(\bar{z}_{i-(a+1)} - \bar{z}_i\right)\left[-\frac{M_{i-(a+1)_1}}{(EI)_{i-(a+1)}} + \frac{S_{i-(a+1)}l_d}{2(EI)_{i-(a+1)}} + K_{BA_{i-(a+1)}}P_{i-(a+1)_2}\right]$$

$$i = 1...n$$

Therefore equation (A15) is also true for $j=a+1$. Also from equation (A12):

$$\frac{P_{(i-a)_2}}{(EA)_{(i-a)}} = \frac{P_{(i-a)+1_2}}{(EA)_{(i-a)+1}} + \left(\bar{z}_{(i-a)+1} - \bar{z}_i\right)\left[-\frac{M_{(i-a)_1}}{(EI)_{(i-a)}} + \frac{S_{(i-a)}l_d}{2(EI)_{(i-a)}} + K_{BA(i-a)}P_{(i-a)_2}\right]$$

Which is substituted into equation (A15) to give:

$$\frac{P_{i_2}}{(EA)_i} = \frac{P_{i-(a-1)_2}}{(EA)_{i-(a-1)}} + \left(\bar{z}_{i-(a-1)} - \bar{z}_i\right)\left[-\frac{M_{i-(a-1)_1}}{(EI)_{i-(a-1)}} + \frac{S_{i-(a-1)}l_d}{2(EI)_{i-(a-1)}} + K_{BA_{i-(a-1)}}P_{i-(a+1)_2}\right]$$

Therefore equation (A15) is true for $j=1$, and if equation (A15) holds for $j=a$, it also holds for $j=a+1$ and $j=a-1$. Hence equation (A13) is true for all j.

Calculation of Axial Force

Rewriting equation (A1) gives:

$$P_{i_2} = -\sum_{j=1}^{i-1} P_{j_2} - \sum_{j=i+1}^{n} P_{j_2} \qquad i = 1...n \qquad \text{... (A16)}$$

and, from equation (A13):

$$P_{j_2} = \frac{(EA)_j}{(EA)_i}P_{i_2} + (EA)_j\left(\bar{z}_i - \bar{z}_j\right)\left[-\frac{M_{i_1}}{(EI)_i} + \frac{S_i l_d}{2(EI)_i} + K_{BA_i}P_{i_2}\right] \qquad \text{... (A17)}$$

$$i = 1...n, j = 1...n$$

Therefore, substituting equation (A17) into (A16) gives:

$$P_{i2} = -\left[\sum_{j=1}^{i-1}(EA)_j\left(\bar{z}_i - \bar{z}_j\right)\left(-\frac{M_{i1}}{(EI)_i} + \frac{S_i l_d}{2(EI)_i}\right) + \sum_{j=i+1}^{n}(EA)_j\left(\bar{z}_i - \bar{z}_j\right)\left(-\frac{M_{i1}}{(EI)_i} + \frac{S_i l_d}{2(EI)_i}\right)\right]$$
$$-\left[\sum_{j=1}^{i-1}\left(\frac{(EA)_j}{(EA)_i} + (EA)_j\left(\bar{z}_i - \bar{z}_j\right)K_{BAi}\right)P_{i2} + \sum_{j=i+1}^{n}\left(\frac{(EA)_j}{(EA)_i} + (EA)_j\left(\bar{z}_i - \bar{z}_j\right)K_{BAi}\right)P_{i2}\right]$$
$$i = 1\ldots n, j = 1\ldots n$$

Therefore:

$$P_{i2} = \frac{-\sum_{j=1}^{n}(EA)_j\left(\bar{z}_i - \bar{z}_j\right)\left(-\frac{M_{i1}}{(EI)_i} + \frac{S_i l_d}{2(EI)_i}\right)}{\sum_{j=1}^{n}\left(\frac{(EA)_j}{(EA)_i} + (EA)_j\left(\bar{z}_i - \bar{z}_j\right)K_{BAi}\right)} \qquad \ldots \text{(A18)}$$
$$i = 1\ldots n, j = 1\ldots n$$

If n=2, and sub-laminates 1 and 2 are designated A and B, equation (A18) can be used to obtain equation (2.3.17).

Calculation of Bending Moment

Re-writing equation (A2) gives:

$$M_{i1} + P_{i2}z_i = M_1 - \sum_{j=1}^{i-1}M_{j1} - \sum_{j=i+1}^{n}M_{j1} - \sum_{j=1}^{i-1}P_{j2}\bar{z}_j - \sum_{j=1}^{i-1}P_{j2}\bar{z}_j \qquad \ldots \text{(A19)}$$
$$i = 1\ldots n$$

and, from equation (A8):

$$M_{j1} = (EI)_j\left[\frac{M_{i1}}{(EI)_i} + K_{BAj}P_{j2} - K_{BAi}P_{i2}\right] \qquad \ldots \text{(A20)}$$
$$i = 1\ldots n, j = 1\ldots n$$

Substituting equation (A20) and (A13) into (A19) gives:

$$M_{i1} + P_{i2}\bar{z}_i = M_1 - \sum_{j=1}^{i-1}(EI)_j\left[\frac{M_{i1}}{(EI)_i} + K_{BAj}P_{j2} - K_{BAi}P_{i2}\right]$$
$$- \sum_{j=1+1}^{n}(EI)_j\left[\frac{M_{i1}}{(EI)_i} + K_{BAj}P_{j2} - K_{BAi}P_{i2}\right]$$
$$- \sum_{j=1}^{i-1}\left(\frac{(EA)_j}{(EA)_i}P_{i2} + (EA)_j(\bar{z}_i - \bar{z}_j)\left[-\frac{M_{i1}}{(EI)_i} + \frac{S_i l_d}{2(EI)_i} + K_{BAi}P_{i2}\right]\right)\bar{z}_j$$
$$- \sum_{j=i+1}^{n}\left(\frac{(EA)_j}{(EA)_i}P_{i2} + (EA)_j(\bar{z}_i - \bar{z}_j)\left[-\frac{M_{i1}}{(EI)_i} + \frac{S_i l_d}{2(EI)_i} + K_{BAi}P_{i2}\right]\right)\bar{z}_j$$
$$i = 1...n$$

which, after some manipulation, gives:

$$M_{i1}\left[\sum_{j=1}^{n}\left(\frac{(EI)_j}{(EI)_i} - \frac{(EA)_j}{(EI)_j}(\bar{z}_i - \bar{z}_j)\bar{z}_j\right)\right]$$
$$+ P_{i2}\left[\sum_{j=1}^{n}\left(\left(\frac{(EA)_j}{(EA)_i} + (EA)_j(\bar{z}_i - \bar{z}_j)K_{BAi}\right)\bar{z}_j - (EI)_j K_{BAi}\right)\right]$$
$$= M_1 - \sum_{j=1}^{n}\left((EI)_j K_{BAj}P_j + (EA)_j(\bar{z}_i - \bar{z}_j)\frac{S_i l_d}{2(EI)_i}\bar{z}_j\right)$$
$$i = 1...n \qquad \text{... (A21)}$$

Substituting equation (A17) into (A21) gives:

$$M_{i1}\left[\sum_{j=1}^{n}\left(\frac{(EI)_j}{(EI)_i} - \frac{(EA)_j}{(EI)_i}(\bar{z}_i - \bar{z}_j)\bar{z}_j - \frac{(EI)_j}{(EI)_i}K_{BAj}(EA)_j(\bar{z}_i - \bar{z}_j)\right)\right]$$
$$+ P_{i2}\left[\sum_{j=1}^{n}\left(\begin{array}{l}\left(\frac{(EA)_j}{(EA)_i} + (EA)_j(\bar{z}_i - \bar{z}_j)K_{BAi}\right)\bar{z}_j \\ -(EI)_j K_{BAi} + (EI)_j K_{BAj}\left(K_{BAi}(EA)_j(\bar{z}_i - \bar{z}_j) + \frac{(EA)_j}{(EA)_i}\right)\end{array}\right)\right]$$
$$= M_1 - \sum_{j=1}^{n}\left((EI)_j K_{BAj}(EA)_j(\bar{z}_i - \bar{z}_j)\frac{S_i l_d}{2(EI)_i} + (EA)_j(\bar{z}_i - \bar{z}_j)\frac{S_i l_d}{2(EI)_i}\bar{z}_j\right)$$
$$i = 1...n \qquad \text{... (A22)}$$

Substituting equation (A18) into (A22), and simplifying, gives:

$$M_{i1} = \frac{M_1 + \frac{S_i l_d}{2(EI)_i}\left[\frac{A_i B_i}{C_i} - D_i\right]}{\frac{1}{(EI)_i}\left[\frac{A_i B_i}{C_i} + E_i\right]} \qquad i = 1...n \qquad \text{... (A23)}$$

where:

$$A_i = \sum_{j=1}^{n} (EA)_j \left(\bar{z}_i - \bar{z}_j\right)$$

$$B_i = \sum_{j=1}^{n} \left(\left(\frac{1}{(EA)_i} + \left(\bar{z}_i - \bar{z}_j\right) K_{BA_i} \right) \left((EA)_j \bar{z}_j + (EI)_j K_{BA_j} (EA)_j \right) - (EI)_j K_{BA_i} \right)$$

$$C_i = \sum_{j=1}^{n} \left(\frac{(EA)_j}{(EA)_i} + (EA)_j \left(\bar{z}_i - \bar{z}_j\right) K_{BA_i} \right)$$

$$D_i = \sum_{j=1}^{n} (EA)_j \left(\bar{z}_i - \bar{z}_j\right) \left(\bar{z}_j + (EI)_j K_{BA_j} \right)$$

$$E_i = \sum_{j=1}^{n} \left((EI)_j - (EA)_j \left(\bar{z}_i - \bar{z}_j\right) \left((EI)_j K_{BA_j} + \bar{z}_j \right) \right)$$

When n=2, and sub-laminates 1 and 2 are designated A and B, equation (A23) is equivalent to equation (2.3.18)

Once the shear force, bending moment and axial force acting on a sub-laminate is known via equations (A10), (A23) and (A18), the deflection of the delaminated beam can be calculated. The analysis then continues as outlined in chapter 2.

Appendix B - Static Beam Model of a Delaminated Beam Section with Multiple Delaminations: Torsional Rigidity

In chapter 2, the method for determining a value for the effective torsional rigidity of a beam with a single delamination was presented. This appendix extends the analysis for *n-1* delaminations, giving *n* sub-laminates.

Consider the delaminated beam in figure B1. Taking equilibrium at the end of the delaminated section gives:

$$T = \sum_{i=1}^{n} T_i \qquad \text{... (B1)}$$

As in equation (2.3.26) it is assumed that, since the delamination is fixed to the beam at its ends, the twist of each sub-laminate at their ends is equal. Hence:

$$\psi = \psi_i = \psi_j \qquad i = 1...n;\ j = 1...n \qquad \text{... (B2)}$$

Also, the angle of twist is related to the torsional rigidity and length of the delaminated section by:

$$\psi_i = \frac{T_i l_d}{(GJ)_i} \qquad i = 1...n \qquad \text{... (B3)}$$

and for the equivalent undelaminated section:

$$\psi = \frac{T l_d}{GJ} \qquad \text{... (B4)}$$

Equations (B2) and (B3) give:

$$T_j = T_i \frac{(GJ)_j}{(GJ)_i} \qquad i = 1...n;\ j = 1...n \qquad \text{... (B5)}$$

Re-writing equation (B1) gives:

$$T = T_i + \sum_{j=1}^{i-1} T_j + \sum_{i+1}^{n} T_j \qquad i = 1...n \qquad \text{... (B6)}$$

Inserting equation (B5) into (B6) therefore gives:

$$T_i = \frac{T(GJ)_i}{\sum_{j=1}^{n}(GJ)_j} \qquad i = 1...n$$

Which, using equation (B2) gives:

$$\psi = \psi_i = \frac{Tl_d}{\sum_{j=1}^{n}(GJ)_j} \qquad i = 1...n \qquad \text{... (B7)}$$

Therefore, by inspection of equations (B7) and (B4), it can be seen that:

$$(GJ)' = \sum_{i=1}^{n}(GJ)_i \qquad \text{... (B8)}$$

Where $(GJ)'$ is the equivalent torsional rigidity for the delaminated section. Equation (B8) is obviously equivalent to equation (2.3.29) when n=2, and 1=A and 2=B.

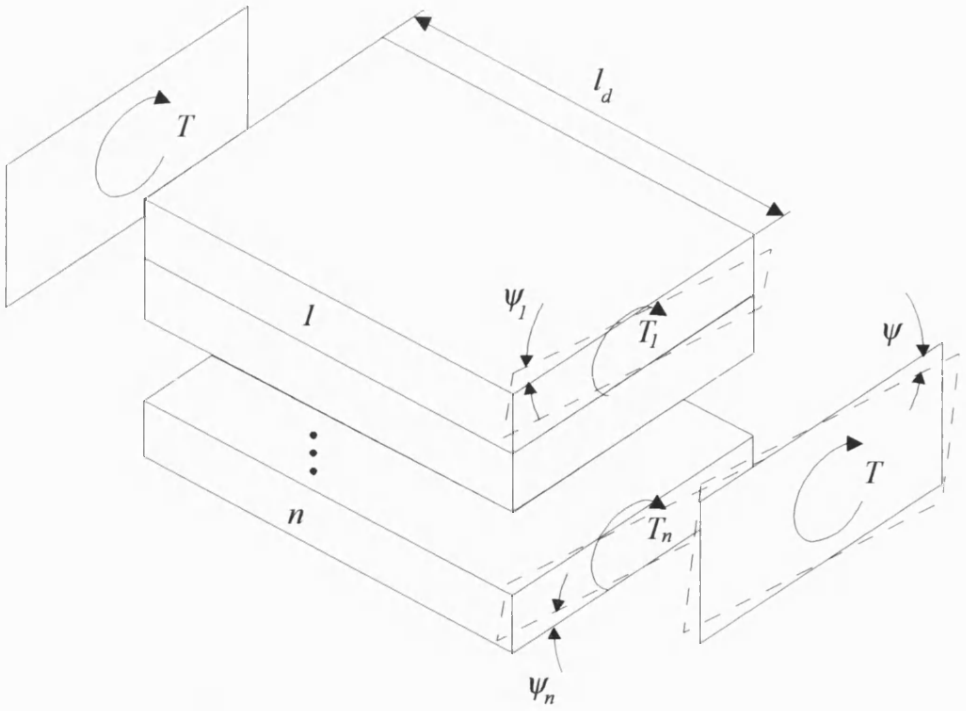

Figure B1 - Delaminated beam section showing the torque acting on each sub-laminate

Appendix C – Experimental Results for the Damaged and Undamaged Beams

This appendix presents the raw data measured from the damaged and undamaged composite laminates described in tables 5.1.2 and 5.1.3, and discussed in Chapters 5 and 6.

In these tables, the experimental results are presented along with the mean value and the standard deviation of the mean value. If an experiment produces a set of n values x, with a mean value of $\bar{x}$, the standard deviation of the mean value σ_m is expressed as:

$$\sigma_m = \sqrt{\frac{\sum_{i=1}^{n}\left(x_i - \bar{x}\right)^2}{n(n-1)}} \qquad \ldots \text{(C1)}$$

Using this equation, it can be said that the actual mean value for x is:

$$x = \bar{x} \pm \sigma_m \qquad \ldots \text{(C2)}$$

This is outlined in many mathematical textbooks.

Mode	Test 1 Frequency [Hz]	Test 2 Frequency [Hz]	Test 3 Frequency [Hz]	Test 4 Frequency [Hz]	Test 5 Frequency [Hz]	Mean Frequency [Hz]	Standard Deviation [Hz]
1B	14.65	12.94	14.92	14.79	14.93	14.45	0.38
2B	90.15	91.80	91.42	91.53	91.52	91.28	0.29
3B	247.62	252.18	251.38	251.40	251.37	250.79	0.81
4B	480.35	489.00	486.99	486.98	486.92	486.03	1.48
1T	71.97	-	-	-	-	71.97	-
2T	221.85	-	-	-	-	221.85	-
3T	422.77	-	-	-	-	422.77	-
4T	684.09	-	-	-	-	684.09	-

Table C1 - Natural frequencies of the undamaged $[0^o,90^o]_{2,s}$ laminate (Case 1 ; B – Bending mode, T – Torsion mode)

Mode	Test 1 Frequency [Hz]	Test 2 Frequency [Hz]	Test 3 Frequency [Hz]	Test 4 Frequency [Hz]	Test 5 Frequency [Hz]	Average Frequency [Hz]	Standard Deviation [Hz]
1B	13.54	12.98	13.33	13.42	13.42	13.34	0.10
2B	87.88	86.50	86.34	86.32	86.32	86.67	0.30
3B	227.84	214.14	207.29	206.98	206.94	212.64	4.04
4B	469.25	461.21	458.25	458.13	458.01	460.97	2.15
1T	64.62	-	-	-	-	64.62	-
2T	220.14	-	-	-	-	220.14	-
3T	360.54	-	-	-	-	360.54	-
4T	650.83	-	-	-	-	650.83	-

Table C2 - Natural frequencies of the Case 2 damaged $[0^o,90^o]_{2,s}$ laminate (B – Bending mode, T – Torsion mode)

Mode	Test 1 Frequency [Hz]	Test 2 Frequency [Hz]	Test 3 Frequency [Hz]	Test 4 Frequency [Hz]	Test 5 Frequency [Hz]	Average Frequency [Hz]	Standard Deviation [Hz]
1B	14.32	14.39	13.91	13.46	14.29	14.07	0.17
2B	90.78	90.25	89.96	89.94	89.85	90.16	0.17
3B	243.40	241.37	240.68	240.76	240.20	241.28	0.56
4B	423.69	410.82	411.20	411.07	408.63	413.08	2.69
1T	70.17	-	-	-	-	70.17	-
2T	217.80	-	-	-	-	217.80	-
3T	397.48	-	-	-	-	397.48	-
4T	580.74	-	-	-	-	580.74	-

Table C3 - Natural frequencies of the Case 3 damaged $[0°,90°]_{2,s}$ laminate (B – Bending mode, T – Torsion mode)

Mode	Test 1 Frequency [Hz]	Test 2 Frequency [Hz]	Test 3 Frequency [Hz]	Test 4 Frequency [Hz]	Test 5 Frequency [Hz]	Average Frequency [Hz]	Standard Deviation [Hz]
1B	14.49	14.26	13.78	14.09	14.38	14.20	0.12
2B	88.82	88.23	87.94	88.37	87.89	88.25	0.17
3B	239.29	242.73	247.38	241.96	241.56	242.58	1.33
4B	486.63	482.54	485.21	476.37	479.85	482.12	1.85
1T	123.67	123.42	121.38	123.59	123.36	123.08	0.43
2T	361.18	354.73	354.23	353.74	353.72	355.52	1.43
3T	639.82	641.68	646.25	639.26	642.63	641.93	1.24

Table C4 - Natural frequencies of the undamaged $[0°,\pm45°,0°]_s$ laminate (Case 4 ; B – Bending mode, T – Torsion mode)

Mode	Test 1 Frequency [Hz]	Test 2 Frequency [Hz]	Test 3 Frequency [Hz]	Test 4 Frequency [Hz]	Test 5 Frequency [Hz]	Average Frequency [Hz]	Standard Deviation [Hz]
1B	14.37	14.36	13.90	13.88	14.19	14.14	0.11
2B	87.44	86.49	86.97	87.08	86.87	86.97	0.15
3B	237.59	237.02	242.24	242.35	235.99	239.04	1.35
4B	469.94	-	480.68	480.57	467.55	474.69	3.46
1T	120.35	120.62	117.44	117.42	121.13	119.39	0.81
2T	352.50	349.33	349.41	348.64	352.82	350.54	0.88
3T	625.10	-	-	-	625.31	625.21	0.11

Table C5 - Natural frequencies of the Case 5 damaged $[0^{\circ},\pm45^{\circ},0^{\circ}]_s$ laminate (B – Bending mode, T – Torsion mode)

Mode	Test 1 Frequency [Hz]	Test 2 Frequency [Hz]	Test 3 Frequency [Hz]	Test 4 Frequency [Hz]	Test 5 Frequency [Hz]	Average Frequency [Hz]	Standard Deviation [Hz]
1B	13.65	13.84	13.40	13.29	14.12	13.66	0.15
2B	86.87	86.40	87.77	87.77	87.09	87.18	0.27
3B	237.35	238.68	243.96	243.66	236.66	240.06	1.56
4B	463.83	475.80	474.52	474.45	444.24	466.57	5.99
1T	117.84	117.60	114.58	114.60	114.31	115.79	0.79
2T	362.84	359.79	362.50	362.78	349.15	359.41	2.63
3T	622.83	631.21	635.58	635.67	619.87	629.03	3.27

Table C6- Natural frequencies of the Case 6 damaged $[0^{\circ},\pm45^{\circ},0^{\circ}]_s$ laminate (B – Bending mode, T – Torsion mode)

Mode	Test 1 Frequency [Hz]	Test 2 Frequency [Hz]	Test 3 Frequency [Hz]	Test 4 Frequency [Hz]	Test 5 Frequency [Hz]	Average Frequency [Hz]	Standard Deviation [Hz]
1B	13.68	14.00	13.51	13.51	14.08	13.76	0.12
2B	84.18	83.12	84.04	84.29	84.07	83.94	0.21
3B	224.63	225.83	229.02	229.83	222.88	226.44	1.31
4B	441.83	430.02	447.53	448.74	442.92	442.21	3.32
1T	109.58	108.89	106.74	106.67	106.65	107.71	0.63
2T	336.13	327.13	334.67	332.34	332.87	332.63	1.53
3T	569.14	-	-	602.28	575.65	582.36	10.14

Table C7 - Natural frequencies of the Case 7 damaged $[0°,\pm45°,0°]_s$ laminate (B – Bending mode, T – Torsion mode)

Mode	Test 1 Frequency [Hz]	Test 2 Frequency [Hz]	Test 3 Frequency [Hz]	Test 4 Frequency [Hz]	Test 5 Frequency [Hz]	Average Frequency [Hz]	Standard Deviation [Hz]
1B	14.10	13.86	13.57	13.28	13.83	13.73	0.14
2B	82.31	81.65	81.60	81.41	81.69	81.73	0.15
3B	220.85	219.53	218.82	224.79	217.95	220.39	1.20
4B	428.69	434.27	431.05	433.08	426.68	430.75	1.39
1T	111.13	110.48	110.34	108.31	108.33	109.72	0.59
2T	329.14	324.31	327.40	331.67	327.49	328.00	1.20
3T	572.50	552.73	565.60	540.05	574.00	560.98	6.44

Table C8 - Natural frequencies of the Case 8 damaged $[0°,\pm45°,0°]_s$ laminate (B – Bending mode, T – Torsion mode)

Mode	Frequency of Undamaged Laminate ω_0 [Hz]	Frequency of Damaged Laminate ω_{0d} [Hz]	$\frac{\omega_{0d}}{\omega_0}$
1B	31.54	31.18	0.99
2B	192.85	192.90	1.00
1T	107.19	108.24	1.01
2T	357.14	360.12	1.01

Table C9 - Natural frequencies of the $[(+45°,-45°,0°,90°)_2]_s$ uni-directional unit ply laminate (Case 9) with and without damage (B – Bending mode, T – Toriosn mode)

Mode	Frequency of Undamaged Laminate ω_0 [Hz]	Frequency of Damaged Laminate ω_{0d} [Hz]	$\frac{\omega_{0d}}{\omega_0}$
1B	62.41	62.43	1.00
2B	384.75	387.49	1.01
1T	204.53	205.44	1.00
2T	516.80	-	-

Table C10 - Natural frequencies of the $[(+45°,-45°,0°,90°)_4]_s$ uni-directional unit ply laminate (Case 10) with and without damage (B – Bending mode, T – Torsion mode)

Mode	Frequency of Undamaged Laminate ω_0 [Hz]	Frequency of Damaged Laminate ω_{0d} [Hz]	$\frac{\omega_{0d}}{\omega_0}$
1B	56.76	56.95	1.00
2B	340.59	343.37	1.01
1T	222.53	224.11	1.01
2T	445.86	-	-

Table C11- Natural frequencies of the $(+45°_4,-45°_4,0°_4,90°_4)_s$ uni-directional unit ply laminate (Case 11) with and without damage (B – Bending mode, T – Torsion mode)

Mode	Frequency of Undamaged Laminate ω_0 [Hz]	Frequency of Damaged Laminate ω_{0d} [Hz]	$\frac{\omega_{0d}}{\omega_0}$
1B	12.32	12.07	0.98
2B	75.76	74.97	0.99
3B	208.24	205.93	0.99
1T	51.06	51.33	1.01
2T	166.30	166.91	1.00
1M	239.19	239.86	1.00
2M	320.65	321.88	1.00
3M	431.00	428.22	0.99

Table C12 - Natural frequencies of the $[(+45°,-45°,0°)_s]_2$ non-crimp fabric unit ply laminate (Case 12) with and without damage (B – Bending mode, T – Torsion mode, M – Mixed mode)

Mode	Frequency of Undamaged Laminate ω_0 [Hz]	Frequency of Damaged Laminate ω_{0d} [Hz]	$\frac{\omega_{0d}}{\omega_0}$
1B	26.43	26.41	1.00
2B	163.19	163.41	1.00
1T	103.32	103.93	1.01
2T	-	340.58	-
1M	-	440.11	-
2M	-	500.76	-

Table C13 - Natural frequencies of the $[(+45°,-45°,0°)_s]_4$ non-crimp fabric unit ply laminate (Case 13) with and without damage (B – Bending mode, T – Torsion mode, M – Mixed mode)